Frequency Domain Modeling and Multidisciplinary Design Optimization of Floating Offshore Wind Turbines

by

Meysam Karimi
B.Sc., Persian Gulf University, 2010
M.Sc., Amirkabir University of Technology, 2012

A Dissertation Submitted in Partial Fulfillment of the
Requirements for the Degree of

DOCTOR OF PHILOSOPHY

in the Department of Mechanical Engineering

Frequency Domain Modeling and Multidisciplinary Design Optimization of Floating Offshore Wind Turbines

by

Meysam Karimi
B.Sc., Persian Gulf University, 2010
M.Sc., Amirkabir University of Technology, 2012

Supervisory Committee

Dr. C. Crawford, Supervisor
(Department of Mechanical Engineering)

Dr. B. Buckham, Supervisor
(Department of Mechanical Engineering)

Dr. R. Dewey, External Member
(Ocean Networks Canada)

ABSTRACT

Offshore floating wind turbine technology is growing rapidly and has the potential to become one of the main sources of affordable renewable energy. However, this technology is still immature owing in part to complications from the integrated design of wind turbines and floating platforms, aero-hydro-servo-elastic responses, grid integrations, and offshore wind resource assessments. This research focuses on developing methodologies to investigate the technical and economic feasibility of a wide range of floating offshore wind turbine support structures. To achieve this goal, interdisciplinary interactions among hydrodynamics, aerodynamics, structure and control subject to constraints on stresses/loads, displacements/rotations, and costs need to be considered. Therefore, a multidisciplinary design optimization approach for minimum levelized cost of energy executed using parameterization schemes for floating support structures as well as a frequency domain dynamic model for the entire coupled system. This approach was based on a tractable framework and models (i.e. not too computationally expensive) to explore the design space, but retaining required fidelity/accuracy.

In this dissertation, a new frequency domain approach for a coupled wind turbine, floating platform, and mooring system was developed using a unique combination of the validated numerical tools FAST and WAMIT. Irregular wave and turbulent wind loads were incorporated using wave and wind power spectral densities, JONSWAP and Kaimal. The system submodels are coupled to yield a simple frequency domain model of the system with a flexible moored support structure. Although the model framework has the capability of incorporating tower and blade structural DOF, these components were considered as rigid bodies for further simplicity here. A collective blade pitch controller was also defined for the frequency domain dynamic model to increase the platform restoring moments. To validate the proposed framework, predicted wind turbine, floating platform and mooring system responses to the turbulent wind and irregular wave loads were compared with the FAST time domain model.

By incorporating the design parameterization scheme and the frequency domain modeling the overall system responses of tension leg platforms, spar buoy platforms, and semisubmersibles to combined turbulent wind and irregular wave loads were determined. To calculate the system costs, a set of cost scaling tools for an offshore wind turbine was used to estimate the levelized cost of energy. Evaluation and comparison of different classes of floating platforms was performed using a Kriging-Bat optimization method to find the minimum levelized cost of energy of a 5 MW NREL offshore wind turbine across standard operational environmental conditions. To show the potential of the method, three baseline platforms including the OC3-Hywind spar buoy, the MIT/NREL TLP, and the OC4-DeepCwind semisubmersible were compared with the results of design optimization. Results for the tension leg and spar buoy case studies showed 5.2% and 3.1% decrease in the levelized cost of energy of the optimal design candidates in comparison to the MIT/NREL TLP and the OC3-Hywind respectively. Optimization results for the semisubmersible case study indicated that the levelized cost of energy decreased by 1.5% for the optimal design in comparison to the OC4-DeepCwind.

Contents

List of Tables

List of Figures

ACKNOWLEDGEMENTS

This PhD dissertation has been carried out in the Mechanical engineering department at the University of Victoria. The PhD research was funded by the Pacific Institute for Climate Solutions (PICS) and the Natural Sciences and Engineering Research Council of Canada (NSERC). I am thankful for their support of this research project.

I would like to particularly acknowledge two people who trusted me and gave me the opportunity to do this research project. Without whom I certainly would not be writing this today:

My supervisors Dr. Curran Crawford and Dr. Brad Buckham have contributed with a magnificent academic support, guidance, numerous and valuable comments, suggestions and criticism of my work. I would like to acknowledge with appreciation their key role in my academic development through their advices on many topics. Through working with them, I feel that I have become more mature as a researcher and learned how to be a well-balanced scientist.

I owe a special debt of gratitude to my past educational supervisors Dr. Saeid Kazemi, Dr. S. Hossein Mousavizadegan, and Dr. Mesbah Sayebani for their knowledge in many fields that has been inspiring and eye opening.

I would like to thank my parents who gradually but firmly established within me a desire for knowledge and mankind. It is really difficult to express the sense of gratitude that I feel towards my family who have been always supportive throughout my educational career and life.

I would like to express my deepest thanks to so many of my friends and colleagues at the Sustainable Systems Design Laboratory (SSDL), West Coast Wave Initiative (WCWI), and Institute for Integrated Energy Systems (IESVic) for helping to foster a collaborative environment of research and learning.

Finally, I would like to express my deepest gratitude to my lovely wife Nooshin who has been a valuable support during my PhD study. Without her supports, I would never have finished this PhD dissertation, mamnoonam azizam.

This dissertation is the result of many years of continuous research at the University of Victoria. During the past years, I have had many unique experiences such as the joy of being a lecturer at university and how to be strong and flexible to overcome many hurdles that could potentially prevent finishing a PhD research project while being abroad. I do praise God for giving me this ability to finish this dissertation.

Meysam Karimi
July 2018

Dedicated to my beloved parents Farideh & Heshmat

and my wife Nooshin for her love and support

Chapter 1

Introduction

1.1 Background and Motivation

An increasing global demand for energy has led to widespread dependence on fossil fuels with numerous unintended consequences, most notably air pollution and climate change. Consequently, numerous renewable energy technologies are being developed in a global effort to replace fossil fuels. Presently, there are a number of generation methods that are considered renewable, including wind, solar, tidal, wave and biomass. The availability of each of these resources varies geographically, however no single renewable technology can provide 100% of the societal electrical power requirements.

Among renewable energy technologies, wind appears to be the preeminent renewable alternative. Wind energy technology is being exploited at significant commercial scales and has established itself as a mature means of renewable energy generation using three blade horizontal-axis configurations and wind farms [1]. However, global wind energy installed capacity is still only a fraction of what it could be. This is partly because of:

1. The economic issues of current renewable and wind energy sources such as return on investment and cost-effectiveness,

2. Difficulties in establishing wind farms due to on-shore wind resource limitations,

3. Public concerns related to noise, visual impact, impact on birdlife, and use of fertile lands.

To combat these factors, a substantial move towards the offshore wind resources has been made in the last two decades, where locational constraints are relaxed and stronger consistent winds are located. [2]. To date, offshore wind technologies have been put into operation primarily in shallow waters using fixed-bottom foundations [3]. However, previous investigations have shown that offshore wind turbines may require floating platforms in deep waters instead of fixed-bottom foundations which are economically limited to maximum water depth of 60 m [2]. The three floating offshore wind turbine (FOWT) support structure classes that dominate the current offshore wind projects are the tension leg platform (TLP) [4], the spar buoy platform [5], and the semisubmersible platform [6] (see Fig. 2.1 and Fig. 4.1). For all the FOWT support structure classes, parameters such as ballast mass, mooring lines, and displacement or a combination of all these parameters stabilizes the floating system in deep waters.

Although the study of floating wind turbines has broadened in recent years, there are still several challenges to overcome including the determination of a simple fast aerodynamics, hydrodynamics, and structural dynamics model to evaluate a wide range of FOWT designs. Thus, there is a need for methodologies to assess platform-turbine system dynamics, design economic, and survivability of a wide range of designs.

In the context of platform-turbine dynamic response analysis, it is common to use non-linear time domain tools to model the coupled hydrodynamic and aerodynamic loading, mooring line loads, structural analysis, and motions of the floating structure. FAST [7], HAWC2 [8], and BLADED [9] are the available fully coupled non-linear aero-hydro-servo-elastic time domain simulation tools in the open-source and commercial domains. Alternative to these simulation tools, a simpler modeling technique

is used in the literature which includes the linearization of system dynamics to facilitate the frequency domain analysis of the floating offshore structures and FOWTs [10–16].

To evaluate the cost contributions of the total offshore wind turbine cost, a set of cost scaling tools is used to estimate the levelized cost of energy (LCOE) of offshore wind turbines developed by Fingersh et al [17]. The OMCE [18] tool developed as an operating and maintenance cost estimator to calculate the cost of offshore wind farms. An offshore wind integrated cost model (OFWIC) [19] estimated the electricity prices for offshore wind energy using a power market. An extensive overview of existing onshore and offshore wind turbine/wind farm cost models provided in Hofmann [20].

To date, there has been no comprehensive study to investigate the technical and economic feasibility of a wide range of FOWTs using interdisciplinary interactions among the wind turbine, floating platform, and mooring system in a consistent framework. Moreover, there is a lack of fast simplified dynamic modeling of the FOWT with a flexible moored support structure in the literature. Hence, this dissertation is focused on developing the early-stage design optimization tools to evaluate across FOWT platform types using frequency domain dynamic modeling approaches.

1.2 FOWT System Components

The complete system of each FOWT design is composed from three main components: the platform, the wind turbine, and the mooring system as shown in Fig. 1.1. To determine the complete suite of loads on the FOWT in a given operating condition, a description of the resulting motions/loads from hydrodynamics and aerodynamics of these three components need to be assembled using a dynamic model. Consequently, the study of moored FOWT support structures requires the development of computational models that can predictively assess the coupled platform-turbine system dynamics, performance, and survivability.

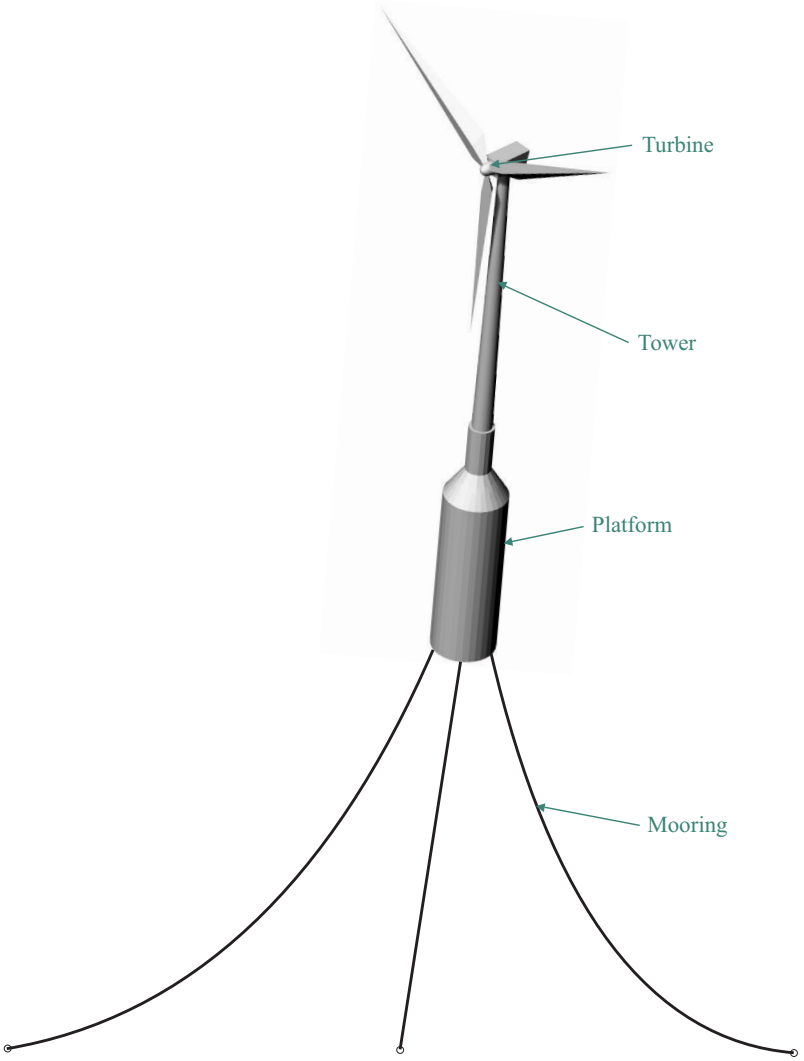

Figure 1.1: FOWT system components including turbine, tower, platform and mooring system

To make a framework for integrating and automating the design process of FOWTs, the computational tools need to be coupled such that the design candidates could be linked to a random search model such as an optimization toolbox. Minimizing the LCOE is the final optimization goal for FOWT technologies.

1.3 Dissertation Outline

The goal of this study is developing a methodology which spans across a wide range of FOWT designs using a fully coupled frequency domain dynamic model and a parameterization scheme for floating platforms, and mooring systems. Using the parametric schemes to describe the design space of the floating platforms, a multi-objective design optimization to study the trade-offs between cost and performance and an multidisciplinary design optimization (MDO) study for the minimum LCOE are executed. For the MDO study, a new frequency domain dynamic modeling of the FOWT is developed using irregular wave and turbulent wind spectral densities, and built by carefully combining the capabilities of validated high-fidelity computational tools. To calculate the FOWT system costs, a set of cost scaling tools is used to estimate the LCOE. The tractable framework and models enable this study to find the optimal FOWTs with the lowest LCOE for the fixed turbine/tower design which is the key research question here. In this way, the optimal design concepts may fall outside established convention and shed new insight on FOWT design.

This dissertation includes three papers which are presented separately in Chapters 2-4. These papers have been accepted/submitted in academic journals. Each paper includes its own abstract, introduction, methodology, results, and conclusions. The Chapters 2-4 follow the development of this research, from an initial multi-objective design optimization framework for simple cost and necelle acceleration comparison (Chapter 2), to a refined frequency domain model (Chapter 3), to a full LCOE-based MDO framework for platform design studies (Chapter 4).

In Chapter 2, a multi-objective design optimization approach for FOWTs with a design space that spans three stability classes of floating wind turbine support structures is presented. A single design parameterization scheme is used to define the geometries of tension-leg, spar buoy, and semisubmersible candidate designs in terms of nine design variables. The dynamic analysis of any particular platform configuration is completed using an uncoupled simplified frequency domain dynamic model applying linearized dynamics for the floating platform, mooring system, and a reference 5 MW wind turbine that are derived using existing functionality in FAST and WAMIT. Evaluation and comparison of different platforms are performed using a Pareto front pursuing multi-objective Genetic Algorithm optimization method to find the locus of platform cost minima and wind turbine performance maxima for a given environmental condition and sea state spectrum. Using above and below-rated steady wind and irregular wave conditions provides a reasonable proxy of typical operating conditions in order to evaluate floater stability. The results/learning in this chapter lead to needs for a coupled frequency domain modeling and an integrated MDO framework for FOWTs.

In Chapter 3, a new frequency domain modeling approach for FOWTs with coupled wind turbine, floating platform, and mooring system sub-models is presented. The sub-models are generated by using the validated numerical tools FAST and WAMIT. While the linearization capability of FAST is utilized, this is only done to obtain a frequency domain sub-model for the rotor/tower aerodynamics and flexible structural response. A separate sub-model based on WAMIT is assembled for the hydrodynamics. The proposed approach in Chapter 3 is distinct in that the model is no longer trying to build a linear model considering each component of the platform geometry separately. Rather it is using a numerical linearization of a full time domain model as the basis for the model creation. This allows for all of the component dynamics to be coupled in the time domain, and then subsequently manifest in the linear model as the linearization process dictates. The approach is therefore unique in

preserving the important frequency-dependent nature of the wave excitation response of the system; this is lost with a more typically adopted full linearization of the coupled system wholely within FAST. The turbulent wind and irregular wave loads are incorporated in the frequency domain model using wind and wave power spectral density functions, the JONSWAP and Kaimal spectra respectively. To validate the proposed 6 DOF frequency domain framework across standard operational environmental conditions, predicted system responses of a 5 MW NREL offshore wind turbine with three classes of baseline platforms including the OC3-Hywind, the MIT/NREL TLP, and the OC4-DeepCwind semisubmersible compared to the outputs of 6 DOF and 22 DOF FAST time domain simulations. The comparison over an aggregate of eleven environmental conditions focused on differences in predicted platform rigid body motions and structural considerations including platform surge, roll, and pitch, and rotor thrust, total blade root and tower base bending moments/fatigue loads, fairlead and anchor tensions/fatigue loads.

In Chapter 4, an MDO approach for floating offshore wind turbine support structures with a design space that spans three stability classes of floating platforms is presented. A design parameterization scheme and a frequency domain modeling approach are incorporated to calculate the overall system responses of TLPs, spar buoy platforms, and semisubmersibles to turbulent wind and irregular wave loads. To calculate the system costs, a set of cost scaling tools for an offshore wind turbine is used to estimate the levelized cost of energy. Evaluation and comparison of different classes of floating platforms is performed using a Kriging-Bat optimization method to find the minimum levelized cost of energy of a 5 MW NREL offshore wind turbine across standard operational environmental conditions. To show the potential of the method, three baseline platforms including the OC3-Hywind spar buoy, the MIT/NREL TLP, and the OC4-DeepCwind semisubmersible are compared with the results of design optimization.

Chapter 5 summarizes the key developments and results from this work, and

suggests a number of avenues for continued development of the FOWT's dynamic modeling and design optimization.

1.4 Research Contributions

The key contributions of the current dissertation are summarized in the following:

1. **Pareto front exploration of FOWT support structures using the frequency domain dynamics and cost models**

   This work executes the global optimization of floating platforms using a multi-objective genetic algorithm optimizer subject to the support structure, and mooring system costs and wind turbine performance. Pareto fronts represent the entire design exploration and optimal design points. In this work, a parameterization scheme for three classes of platform with a revised frequency domain dynamic model is used. The results generated in this work are subject to the specifics of the targeted environmental conditions, cost model, linearized dynamics and choice of performance metric. The proposed method for this work is discussed in Chapter 2 and used to generate a list of the most promising floating support structures that can then be used as conceptual foundations for the detailed design processes. The limitations of the proposed frequency domain dynamic model lead to needs for a new fully coupled frequency domain modeling approach for FOWTs as discussed in Chapter 3. However, the platform design parametrization and support structure cost model of this work are then applied in the multidisciplinary design optimization approach discussed in Chapter 4. Note that this design optimization built on the progress reported in Hall et al [21]. Compared to the method and results in Hall et al [21], a new global optimization algorithm with an updated frequency domain dynamic model are employed in this study. With these changes, the shapes of the Pareto fronts and optimal platform designs are dramatically changed.

2. **Fully coupled frequency domain modeling of FOWT system responses in irregular wave/wind loads**

   This work is focused on a methodology using a frequency domain dynamics modeling approach for FOWTs: one which can quickly provide insight on system performance using the frequency domain coupled aerodynamics, hydrodynamics, and structural dynamics to calculate the overall system response to turbulent wind and irregular wave loads. This frequency domain model is the first FOWT linearized dynamic model which has included combined realistic turbulent wind and irregular wave conditions. In addition, the flexibility of the approach (variable DOFs), efficient use of validated tools to build the model, and ability through random phase inputs to very quickly simulate whole range of DLCs accurately inside an MDO tool make this study unique. The proposed method for this work is discussed in Chapter 3 and validated using FAST time domain results. Using this simple fast and sufficiently accurate frequency domain approach, multidisciplinary design optimization for a wide range of platform designs under a fully coupled floating system is performed in Chapter 4.

3. **Multidisciplinary design optimization of FOWT support structures for minimum LCOE**

   This work is aimed to apply a multidisciplinary design optimization approach on FOWTs in order to explore the optimal designs with minimum LCOE. To achieve this goal, a fully coupled frequency domain dynamic model (see Chapter 3) is integrated to the the framework to evaluate the internal forces, system motions, and other dynamic variables from the frequency domain outputs. Using the frequency domain dynamic model and the parametric scheme (see Chapter 2) to numerically span the design space, a multidisciplinary design optimization of FOWT support structure is executed in Chapter 4.

To minimize the levelized cost of energy for FOWTs as a single objective function, the design optimization architecture uses numerical optimization techniques involving the full design parameterization, the fully coupled frequency domain dynamic model, and a cost model. Note that the Kriging-Bat optimization algorithm used from the study of Saad et al [22]. The main potential of this research is developing a method that can handle parameterization and optimization for a wide range of FOWT support structures. However, the proposed approach is useful beyond platform design, to coupled turbine, platform, and controller design optimization.

Chapter 2

A Multi-Objective Design Optimization Approach For Floating Offshore Wind Turbine Support Structures

This paper is accepted for publication at the Journal of Ocean Engineeing and Marine Energy.

Karimi, Meysam, Matthew Hall, Brad Buckham, and Curran Crawford." A multi-objective design optimization approach for floating offshore wind turbine support structures." Journal of Ocean Engineering and Marine Energy 3, no. 1 (2017): 69-87. Available online at: https://link.springer.com/article/10.1007%2Fs40722-016-0072-4

This chapter presents a multi-objective design optimization approach for floating wind turbines using a parametrization design scheme and a frequency domain dynamic model. The focus in this chapter is on the preliminary conceptual design of three classes of floating platforms subject to the support structure cost and wind turbine performance. Several platform designs are presented in this chapter to show the potential of the proposed approach for techno-economic analysis of a wide range

of FOWTs as the key research question in this dissertation. The design parametrization scheme and the cost model developed in this chapter are then applied to the comprehensive MDO study of FOWTs presented in Chapter 4.

Abstract This chapter presents a multi-objective design optimization approach for floating wind turbines with a design space that spans three stability classes of floating wind turbine support structures. A single design parameterization scheme was used to define the geometries of tension-leg, spar buoy, and semi-submersible candidate designs in terms of nine design variables. The seakeeping analysis of any particular platform configuration was completed using a simplified frequency-domain dynamic model applying linearized dynamics for the floating platform, mooring system, and a reference 5 MW wind turbine that were derived using existing functionality in FAST and WAMIT. Evaluation and comparison of different platforms was performed using a Pareto front pursuing multi-objective Genetic Algorithm (GA) optimization method to find the locus of platform cost minima and wind turbine performance maxima for a given environmental condition and sea state spectrum. Optimization results for the single-body platforms indicated a dominance of tension-leg platforms in this subset of the design space. Results for multi-body platforms showed that semi-submersible platforms with four floats demonstrated better stability and were more cost effective than other semi-submersible designs. In general, the full exploration of the design space demonstrated that four float semi-submersible platforms with angled taut mooring systems are a promising concept that can be used as a foundation for a detailed design and costing study. The results generated here are subject to the specifics of the targeted environmental conditions, cost model, linearized dynamics and choice of performance metric. As these elements evolve, the optimization framework presented here should be reapplied to track how the Pareto fronts for the different classes of platforms respond.

keywords Wind turbine, Offshore, Floating platform, Optimization, Frequency-domain analysis

2.1 Introduction

An increasing global demand for energy has led to widespread dependence on fossil fuels with numerous unintended consequences, most notably air pollution and climate change. Consequently, numerous renewable energy technologies are being developed in a global effort to replace fossil fuels. Wind appears to be the preeminent renewable alternative: wind energy technology is being exploited at significant commercial scales and has established itself as a mature means of renewable energy generation [1]. Along coastlines, high average wind speeds are realized that can provide reliable power. To date, offshore wind technologies have been put into operation primarily in shallow waters using fixed-bottom foundations [3]. However, previous investigations have shown that offshore wind turbines may require floating structures in deep waters instead of fixed-bottom foundations which are economically limited to a maximum water depth of 60 m [2]. Although the study of floating wind turbine platforms has broadened in recent years, there are still several challenges to overcome including the determination of optimal floating platform designs. This work is focused on a methodology for selecting an optimal platform configuration: one which provides the wind turbine with maximum stability at minimal cost.

The three platforms that dominate current offshore wind projects are shown in Fig. 2.1. A mooring-stabilized platform, also called a TLP, is shown in Fig. 2.1(a) that uses taut vertical mooring lines to keep the highly buoyant platform stable. Figure 2.1(b) shows an example of the ballast-stabilized class, also known as a spar buoy, which uses a heavy ballast mass and a deep draft to bring the platform's center of mass well below the center of buoyancy of the structure to produce very large buoyant restoring moments. The buoyancy-stabilized class of support structures,

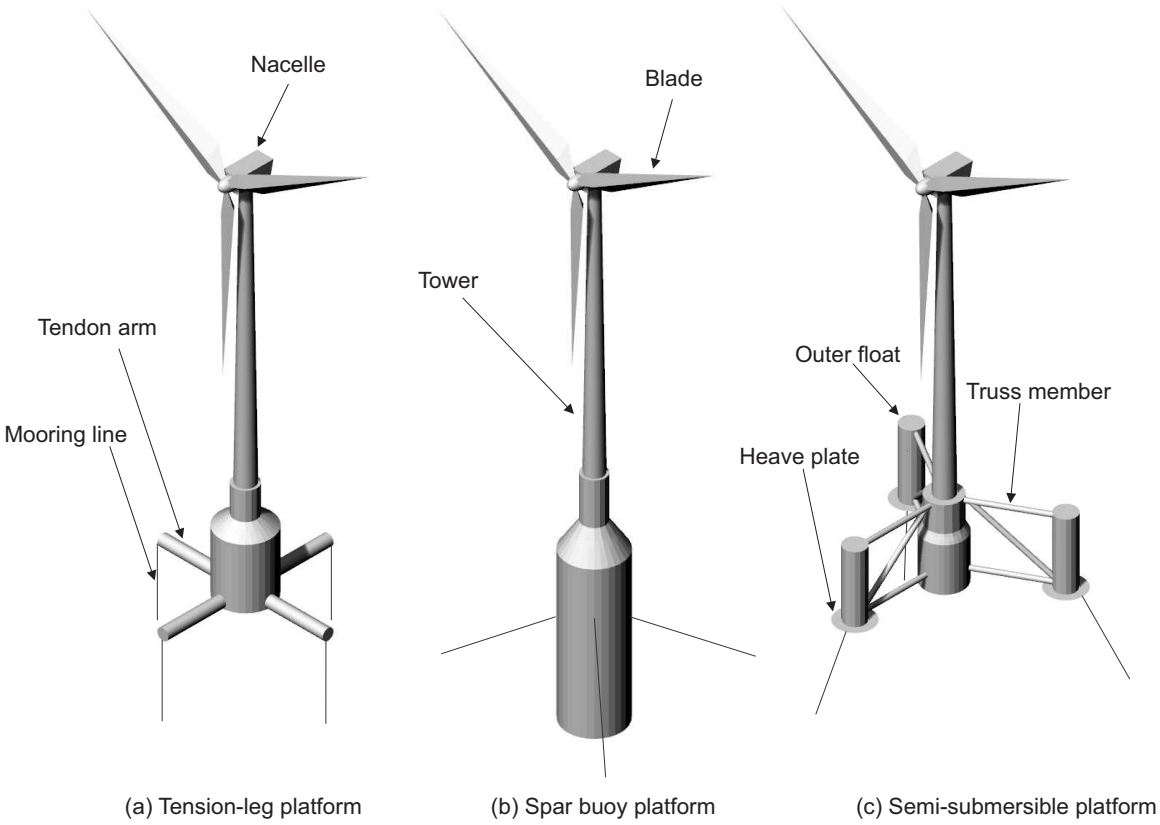

Figure 2.1: The three classes of offshore floating wind turbine support platforms: (a) mooring stabilized (tension-leg), (b) ballast stabilized (spar buoy), and (c) buoyancy stabilized (semi-submersible)

shown in Fig. 2.1(c), uses a large water plane area to raise the metacenter of the platform above the center of mass. This kind of structure is commonly referred to as a semi-submersible platform and is characterized by multi-cylinder configurations that surround the central tower.

Past studies have initiated comparison analyses of the different platform stability classes. A comprehensive dynamic-response analysis for six FOWTs, spanning all the stability classes, was presented by Robertson and Jonkman [4]. Lefebvre and Collu [23] used seven preliminary platform concepts and compared them through a techno-economic analysis to find the best design within the set of seven. Bachynski and Moan [24] analyzed a wide range of design parameters for five single-column TLP platforms using high fidelity computational tools to evaluate the structural loads and

performance of FOWTs under specific environmental conditions. A coupled nonlinear dynamic analysis of four FOWT platforms, including all the stability classes, in three wind turbine fault scenarios and extreme environmental conditions was performed by Bachynski et al [25]. Bachynski's study compared the candidate platform designs on the basis of the structural loads and platform motions arising under these conditions. Benassai et al [26] conducted a numerical parametric study for catenary and vertical tensioned mooring systems of a FOWT to evaluate the influence of water depth on the mooring system configurations under operational and extreme environmental conditions. Karimirad and Michailides [27] completed a dynamic analysis of a specific V-shaped semi-submersible floating wind turbine topology and investigated the hydrostatic stability of different variants of the V-shaped platform.

In the context of floating wind turbine design optimization, there is a surprising lack of studies that explore the full range of platform design classes. One of the first offshore platform design optimization studies was performed by Clauss and Birk [28]. They presented a hydrodynamic shape optimization procedure to improve the seakeeping qualities of a range of ballast stabilized and buoyancy stabilized platforms. Wayman [12] presented a design optimization and economic analysis for four design concepts including a spar, a TLP, and two buoyancy-stabilized variants (a barge and a tri-floater concept) considering steady-state design conditions. Wayman et al [13] also conducted a coupled dynamic analysis for the NREL 5 MW offshore wind turbine in two semi-submersible arrangements in water depth of 10-200 m. A comprehensive design optimization of a floating wind turbine platform was conducted by Tracy [14]. Tracy's study presented a parameterization of single-body platforms and mooring lines. The parameterization enabled an automated search across the design space; for a specific set of parameters a FOWT candidate could be automatically evaluated and then compared to other design candidates. Parker [29] optimized the design of TLPs using a parametric analysis of the mooring-stabilized platform classes. Fylling and Berthelsen [30] created a framework for optimizing spar buoy

platform and mooring line costs using a gradient method for the non-linear objective function and constraints. Brommundt et al [31] used a new tool for the optimization of FOWT catenary mooring systems based on a frequency-domain analysis of the platform dynamic responses. They focused on minimizing cost of the mooring system as well as finding the optimal arrangement for the mooring lines in a particular environmental condition. Myhr et al [32] presented optimization routines to adjust the geometry and mooring line layout for Tension-Leg-Buoy (TLB) platforms subject to support structure cost. Hall et al [21] completed a design optimization of the support structure for floating wind turbines. They employed a cumulative multi-niching GA optimizer and a frequency-domain dynamic model for three stabilized classes of floating platforms. Hall et al [33] provided a hydrodynamics-based floating wind turbine platform optimization in the frequency-domain by combining characteristics from a diverse set of basis platform geometries. For an extensive review of the challenges and recent approaches in the design optimization of wind turbine support structures, the reader is referred to the survey presented by Muskulus and Schafhirt [34].

In this study, a wide range of platform designs is addressed by using a parameterization scheme that spans all three platform stabilization classes, and includes both tension leg and catenary mooring lines. Using this parametric scheme to numerically traverse this broad design space, a platform design optimization study is executed. The current design optimization builds on the progress reported in Hall et al [21]. Compared to the method and results in Hall et al [21], a new global optimization algorithm with an updated frequency-domain dynamic model are employed in this study. With these changes, the shapes of the Pareto fronts and optimal platform designs are dramatically changed.

The approach taken for this optimization problem is not to automate the generation of detailed platform designs. Rather, the goal is to generate a list of the most promising floating support structures that can then be used as conceptual foundations for the detailed design processes. To identify promising concepts, the optimization

algorithm in this work is focused on the task of generating Pareto sets. Each Pareto set is the series of minimum design costs, across the range of possible performances (measured in terms of turbine nacelle acceleration). Through reporting of the Pareto fronts, this work enables the reader to consider trade-offs between cost and performance over a finite subset of promising designs. In this way, the optimal platform design concept may fall outside established convention and shed new insight on FOWT design.

The remainder of this chapter is presented in five main sections as follows. The coupled frequency-domain dynamics model to evaluate the response and behaviour of any given design candidate is discussed in section 2.2. Section 2.3 defines the support structure parameterization scheme including floating platform geometries, and mooring system types. Section 2.4 summarizes the multi-objective GA, objective functions, and design constraints used to explore a complete design space. The validity of the frequency-domain dynamic model is discussed in section 2.5. Sections 2.6 and 2.7 present the results and subsequent conclusions of this work, respectively.

2.2 Design analysis methodology

The complete system dynamics of each floating wind turbine candidate design is composed from three main components: the platform, the wind turbine, and the mooring system (see Fig. 2.1). To determine the complete suite of loads on the floating wind turbine in a given operating condition and build a description of the resulting motion in the frequency-domain, linearized representations of the hydrodynamics and aerodynamics of these three components must be assembled. In the following subsections, we describe how these contributions to the dynamic model are determined.

2.2.1 Inviscid platform hydrodynamics

The inviscid hydrodynamic properties of the platform are calculated using WAMIT to solve for the inviscid potential flow around the floating body for the series of all expected wave frequencies. Note that only first-order wave forces are calculated in this study. WAMIT generates frequency dependent coefficients including added mass, damping, and wave excitation for a six degree of freedom (DOF) platform in terms of the global coordinate system on the free surface. Before WAMIT is called, a C++ code discretizes the surface of each platform to generate the input mesh file for WAMIT. The same code also handles the calculation of mass and inertia properties for each platform. This C++ code is interfaced to the Matlab-based frequency-domain dynamic model (see Eq. 2.4) using a Matlab executable file. It is necessary to mention that the truss members and tendon arms (see Fig. 2.1(a) and Fig. 2.1(c)) are excluded from inviscid platform hydrodynamic analysis for two reasons: one is to avoid creating an overly complex panel mesh file for WAMIT, and the other reason is the relatively small wave-radiation and diffraction contribution of these slender bodies [35]. However, these slender components are included in the viscous drag and added mass calculations discussed in the next subsection.

2.2.2 Viscid platform hydrodynamics

To consider the effect of additional platform damping due to drag, a linear representation of Morison's equation, referred to Borgman's linearization [36] in the literature, is used for the platform's submerged cylinders, truss members, and tendon arms (see Fig. 2.1). In order to apply this drag term, the length of each element is divided into a number of sections and drag forces are calculated using the principles of strip theory. For linear frequency-domain calculations, the viscous drag for a single strip becomes:

$$dF_d = (\frac{1}{2}\rho C_d D\sqrt{\frac{8}{\pi}}\sigma_u U)\ dL \tag{2.1}$$

where dF_d is the drag force on a section of length dL and diameter D, ρ is the water density, C_d is the constant drag coefficient taken as 1 [37], U is the transverse component of relative water velocity at the strip, and σ_u is the standard deviation of U (considering all of the frequency components). In this study, to maintain the linear representation of the frequency-domain problem, wave velocity is neglected and only platform motion is used in the calculation of the velocity of each strip. In irregular wave conditions, the phases of the constituent regular waves are not known-rather they are considered entirely random. To complete a true relative velocity calculation the phase of each component regular wave would have to be arbitrarily assigned leading to an arbitrarily scaled damping effect in the form of a new wave force and moment at the platform center of gravity. Any fidelity that may be gained through that step is negated by the approximation inherent in the linearization and the subsequent superposition of the linear terms. Hence, U in Eq. 2.1 is defined for each section, and at each frequency considered, based only on the displacement of the platform center of gravity with respect to the global coordinate system. The normal velocity of a vertical submerged cylinder is expressed as a linear function of the platform surge and sway motions using the known location of the vertical cylinder in the platform design. The normal displacement amplitude for any tendon arms and truss members is similarly defined in terms of the surge, sway, and heave motions of the platform. An iterative procedure is used to fill-in the entries of this damping matrix (see Fig. 2.2): on each iteration an estimate of σ_u is applied in Eq. 2.1, U in Eq. 2.1 is defined as a linear function of platform motion variables, and the coefficients of these motion variables in the resulting expression are transferred to the damping matrix which is used to calculate the next estimate of the response at the frequency being considered. By adopting strip theory approach for drag forces applied to the platform elements, a viscous damping coefficient matrix can be calculated for

all DOFs.

The hydrodynamic drag characteristics of the heave plates (see Fig. 2.1(c)) are calculated by applying the Fourier-Averaged method to the Morison quadratic drag force [38]. The linearized viscous drag coefficient for the heave plates follows as:

$$B = \frac{2}{3}\rho D^2(2\pi a)C_d \tag{2.2}$$

where D is the diameter of the heave plate, C_d is considered as a constant heave plate drag coefficient of 4.8, and a is the average of the amplitude of all of the heave plate oscillations [38]. This viscous coefficient can be directly inserted into the platform damping matrix.

As mentioned previously, in constructing a WAMIT geometry file for each platform design, connective members including truss elements and tendon arms are not included. In order to capture the hydrodynamic added mass of these connective members, the added mass values from Morison's equation are used as shown in Eq. 2.3 for accelerations normal to the cylinder axis [39]:

$$dM_a = (\frac{\pi}{4}\rho C_a D^2)\ dL \tag{2.3}$$

where dM_a is the added mass value from a section of length dL and diameter D, ρ is the water density, and C_a is the constant added mass coefficient taken as 1 [37]. Similar to the calculation of viscous drag forces, the length of each cylinder is discretized axially into a number of sections and added mass values are calculated using strip theory. The resulting added mass coefficients in these expressions are superposed on the added mass matrix calculated by WAMIT to create the total added mass matrix for the platform. That superposition process is facilitated by expressing the normal accelerations of the cylinder section as linear functions of the surge, sway, and heave motions of the platform center of gravity.

2.2.3 Wind turbine properties

The wind turbine dynamic characteristics are kept constant in this study: i.e. the same wind turbine is mounted on every floating platform design. FAST, an aeroelastic computer-aided engineering (CAE) tool, is used to generate linearized dynamic quantities for the three-bladed NREL 5 MW horizontal axis wind turbine [40]. FAST creates the linearized mass matrix, damping matrix, and stiffness matrix for each wind speed at a zero pitch angle that is referenced to the tower-base coordinate system. These coefficients are directly applied within the frequency-domain dynamic model (see Eq. 2.4) to evaluate the influence of rotor aerodynamics and wind turbine mass on the FOWT motions. The default controllers for the 5 MW reference turbine are used in this work.

2.2.4 Mooring line loads

Similar to the platform hydrodynamic loads, mooring line loads can be linearized and added to the frequency-domain dynamic model using the quasi-static mooring subroutine of FAST [41]. In order to better integrate the different parts of the dynamic model, this subroutine was translated into a C++ code which executes the generation of the mooring stiffness matrix, and the fairlead/anchor tension offsets for each wind speed and water depth. In generating the mooring line model, the linearization procedure is performed based on the steady state displaced position of the floating platform corresponding to the wind turbine thrust load at each wind speed as noted by Tracy [14] and Hall [15]. This model is interfaced to the Matlab-based dynamic model using a Matlab executable file. At this time, wave drift loads are not considered in the calculation of the displaced mooring configuration.

2.2.5 Frequency-domain dynamic model

To evaluate the dynamics of a candidate FOWT, all the aforementioned loads and coefficients for the wind turbine, mooring system, and floating platform are gathered into 6x6 system mass, stiffness and damping matrices. The resulting linearized equation of motion for the case of a unit amplitude regular wave is shown in Eq. 2.4:

$$\begin{aligned}[M_a(\omega) + M_{WT} + M_p]\ddot{\zeta}(t) + [B_{WT} + B_P(\omega) + B_{Visc}(\omega, \zeta)]\dot{\zeta}(t) \\ +[C_{WT} + C_P + C_M]\zeta(t) = \hat{X}(\omega)e^{i\omega t}\end{aligned} \tag{2.4}$$

where $\zeta(t) = \hat{Z}(\omega)\ e^{i\omega t}$ is the six DOF platform complex response and $\hat{Z}(\omega)$ is the complex amplitude vector for the platform displacement, $M_a(\omega)$ is the platform added mass matrix calculated using WAMIT and Morison's equation (Eq. 2.3), M_{WT} is the mass matrix of the wind turbine and M_P is the mass matrix of the floating platform, B_{WT} is the damping matrix of the wind turbine, $B_P(\omega)$ is the platform frequency dependent damping matrix generated using WAMIT, $B_{Visc}(\omega, \zeta)$ is the six-by-six viscous damping coefficient discussed in viscid platform hydrodynamics, C_{WT}, C_P, and C_M are the linearized wind turbine, platform, and mooring line stiffness matrices, respectively. $\hat{X}(\omega)$ is the first-order wave excitation vector calculated by WAMIT, and ω is the wave and platform motion frequency.

Making use of Eq. 2.4, the complex form of the equation of motion to evaluate the complex response of the FOWT to the wave excitation forces at a single frequency can be written as:

$$-\omega^2 M_{total}(\omega)\hat{Z}(\omega) + i\omega B_{total}(\omega, \zeta)\hat{Z}(\omega) + C_{total}\hat{Z}(\omega) = \hat{X}(\omega) \tag{2.5}$$

where $M_{total}(\omega)$, $B_{total}(\omega, \zeta)$, and C_{total} are the total mass matrix, damping matrix, and stiffness matrix of the FOWT respectively. By calculating the complex response of the FOWT, RAOs for all modes of motion can be calculated by solving Eq. 2.5 for unit amplitude waves for each frequency in terms of DOF amplitudes and phases.

The RAOs for all six DOF are given as:

$$\begin{bmatrix} RAO_1(\omega) \\ \vdots \\ RAO_6(\omega) \end{bmatrix} = \left[-\omega^2 M_{total}(\omega) + i\omega B_{total}(\omega, \zeta) + C_{total} \right]^{-1} \hat{X}(\omega) \tag{2.6}$$

where the numerical subscripts indicate the floating structure DOFs: 1 to 6 define surge, sway, heave, roll, pitch and yaw displacements, respectively. The contribution of all three major parts of an FOWT to the linear frequency-domain dynamic model is shown in Fig. 2.2. The complete response of the FOWT in an irregular wave regime is found by multiplying the individual frequency components of the wave spectral density function, $S(\omega)$, by the RAOs evaluated at that frequency (see Fig. 2.7).

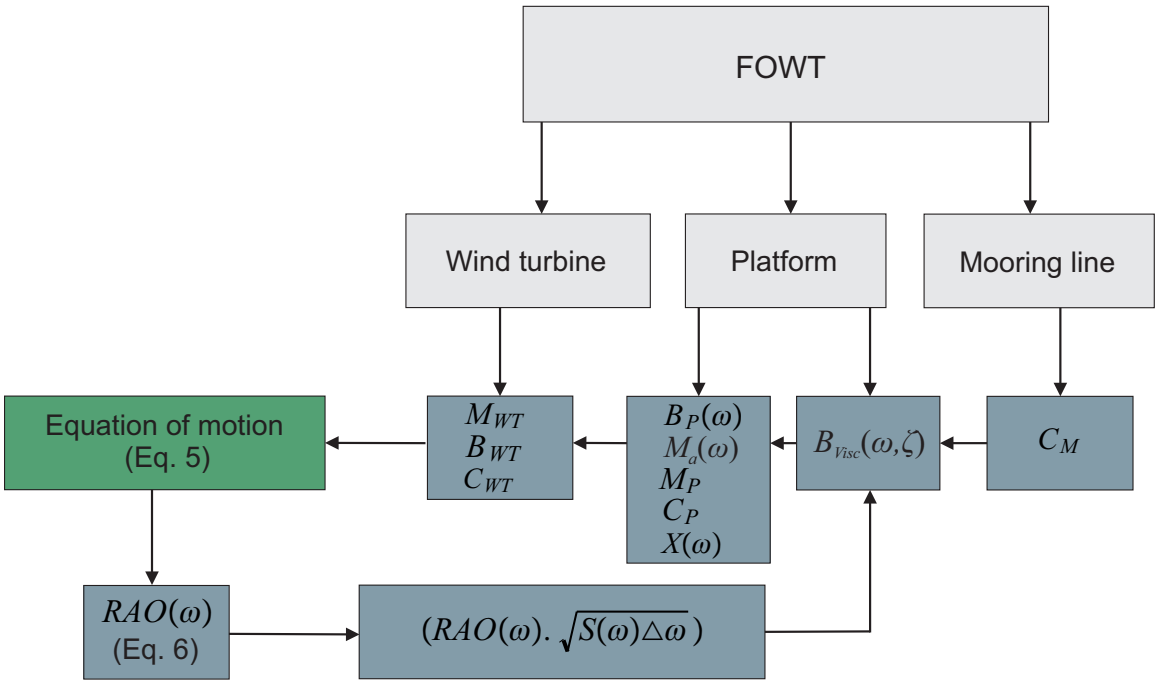

Figure 2.2: Solution procedure for dynamic analysis of an FOWT in the frequency-domain. In this procedure, an iterative approach is taken into account. Once a stable estimate of the viscous damping matrix is achieved, the RAO values at the frequency in question are calculated. Repeating this calculation for all of the incident wave frequencies establishes the RAO functions that are combined with the incident wave spectrum, $S(\omega)$, to form the complete estimate of the platform response

2.3 Support structure parameterization

The platform parameterization scheme used in this work attempts to describe the widest range of offshore wind turbine platforms and mooring systems with as few design variables as possible. In this section, the platform topology, size of connective elements, fairlead and anchor locations, mass and ballast, and the cost of the overall structure are defined in terms of nine design variables [15].

2.3.1 Platform topology

All the platform designs are formed by a central cylinder with variable radius and draft, and an array of outer cylinders whose radius, draft and distance from the center

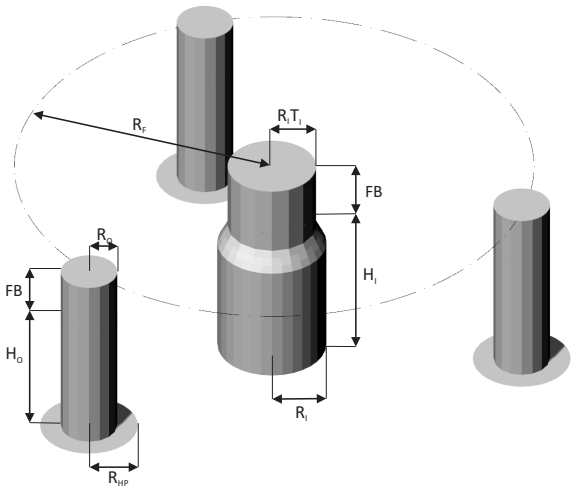

Figure 2.3: A perspective view of a multi-body platform including four floats (one inner cylinder and three outer cylinders) with design parameters

are also variable in the platform design parameterization. The outer cylinders can include circular heave plates of variable size at their bases. In order to adjust the wave interaction with the floating platform, a variable taper ratio is implemented for the central cylinder draft elevations. A free board (FB) of 5 m is used for all the platform designs as a constant design parameter. Figure 3 illustrates the geometry for a multi-body platform with three outer floats. Referring to Table 1, the eight geometric design variables include the inner cylinder draft, H_I, the inner cylinder radius, R_I, the top tapper ratio of inner cylinder, T_I, number of outer cylinders, N_F, the radius of outer cylinder array, R_F, the outer cylinder draft, H_O, the outer cylinder radius, R_O, and the outer cylinder heave plate radius, R_{HP}. Constraints are applied to these variables to ensure that the inner cylinder diameter is not less than the wind turbine tower base diameter which is 6 m [40], and to avoid large taper angles near the water line.

Table 2.1: Geometric design variables of platform

Variable	**Description**	**Min.**	**Max.**
H_I	Inner cylinder draft	2 m	150 m
R_I	Inner cylinder radius	3 m	25 m
T_I	Top taper ratio	0. 2	2
N_F	Number of outer cylinders	3	5
R_F	Radius of outer cylinderarray	5 m	40 m
H_O	Outer cylinder draft	3 m	50 m
R_O	Outer cylinder radii	1.5 m	10 m
R_{HP}	Outer cylinders heave plate radii	0	20 m

Cross-bracing

In order to connect the outer cylinders to the central element, truss members are needed. These cross-bracing elements are modeled by three truss members - two horizontal and one diagonal - between each pair of connected cylinders (see Fig. 2.4). The truss members are treated as hollow cylinders with a fixed wall thickness to radius ratio of $k = 5\%$ [42]. A single diameter for all the truss members is chosen based on the pinned-pinned critical buckling load, P_{Crit}, of the diagonal member given by Eq. 2.7.

$$P_{Crit} = \frac{\pi^2 EI}{L^2} \tag{2.7}$$

where L is the length of the diagonal member, $E = 200\, GPa$ is the module of elasticity of steel, and I is the tubular section's moment of inertia. The design load, P_{des}, that is evaluated against the buckling limit is:

$$P_{des} = \frac{\max(\rho \forall_O g,\ T_{Line\,\max})}{\sin(\theta)} \tag{2.8}$$

The numerator of Eq. 2.8 shows the maximum load on the truss member which is taken to be the larger of the displaced weight of one of the outer cylinders, $\rho \forall_O g$ (which includes water density ρ, outer cylinder displacement $\forall_O$, and gravitational acceleration g) or the maximum steady state mooring tension, $T_{Line\ \max}$, if mooring

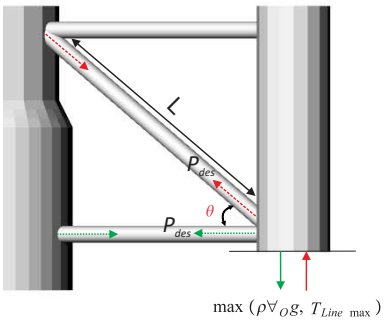

Figure 2.4: Physical interpretation of implemented loads on the diagonal truss member

lines are connected to the outer cylinder. The angle θ is the inclination angle of the diagonal member. The steady-state mooring line tension is evaluated at the rated wind speed which results in the maximum thrust load on the mooring system. The length of the diagonal member, L, is calculated between two points in the platform design: one at 90% of the inner or outer cylinder draft, whichever is less, and one at the elevation of half of the FB height (see Fig. 2.4).

The justification for the approach embodied in Eq. 2.8 is explained through two cases; in the case where the outer cylinders of a multi-body platform provides a significant contribution to the stability of the floating platform, the buoyancy forces from the outer cylinders create a compressive load on the diagonal member. As a result, the diameter of the truss members are calculated to ensure that this compression load does not induce buckling. On the other case, if the outer cylinders are smaller than the inner cylinder, the majority of the load on the truss members is applied by the mooring lines attached to the outer cylinders, imposing a compressive load on the bottom horizontal truss members. In the latter case, the required diameter for the truss members is calculated again using the diagonal member load and length, even though this member is in tension, as this gives a conservative result.

The diameter of the members can then be calculated considering the critical buckling load (Eq. 2.7), where P_{Crit} is equal to the design load, P_{des}, multiplied by a safety

factor of 10, which includes compensation for the growth of the maximum mooring line tension in the presence of waves. This leads to:

$$D = \left(\frac{8}{\pi^3} \frac{P_{Crit} L^2}{Ek} \right)^{1/4} \tag{2.9}$$

where k is a constant wall thickness to radius ratio.

2.3.2 Mooring system

To maintain as broad a design space as possible, a continuous range of mooring layouts, from taut lines to slack catenary are included in the parameterization scheme. The mooring line configuration is specified based on the platform design variables, shown in Table 2.1, water depth, and an additional design variable specific to the mooring system, X_M. In this study, the mooring system design variable transitions between a taut vertical line configuration ($-1 \leq X_M \leq 0$), an angled taut (non-vertical) line configuration ($0 < X_M \leq 1$), and a slack catenary (non-vertical) line configuration ($1 < X_M \leq 2$), as illustrated in Table 2.2 and shown in Fig. 2.5.

The number of mooring lines and the fairlead locations are determined by the platform geometry and X_M. To avoid wasting computational time in the design of mooring systems, some constraints are applied to the number of mooring line and their geometric arrangement. For single-body designs with taut vertical lines (TLPs), four lines are used and they are connected at the end of each tendon arm as shown in Fig. 2.1(a) [43]. For single-body platforms with slack and taut non-vertical lines (spar buoys) three lines are used that are connected at half the cylinder draft as shown in Fig. 2.1(b) [44]. For multi-body designs as in Fig. 2.1(c), a mooring line is connected at the bottom of each outer cylinder [42].

The anchor location is determined by the linear variation of X_M from lying directly under the fairlead, when $-1 \leq X_M \leq 0$, to the horizontal spread of double the water depth ($X_M = 2$) as can be seen in Fig. 2.5. The unstretched mooring line length for

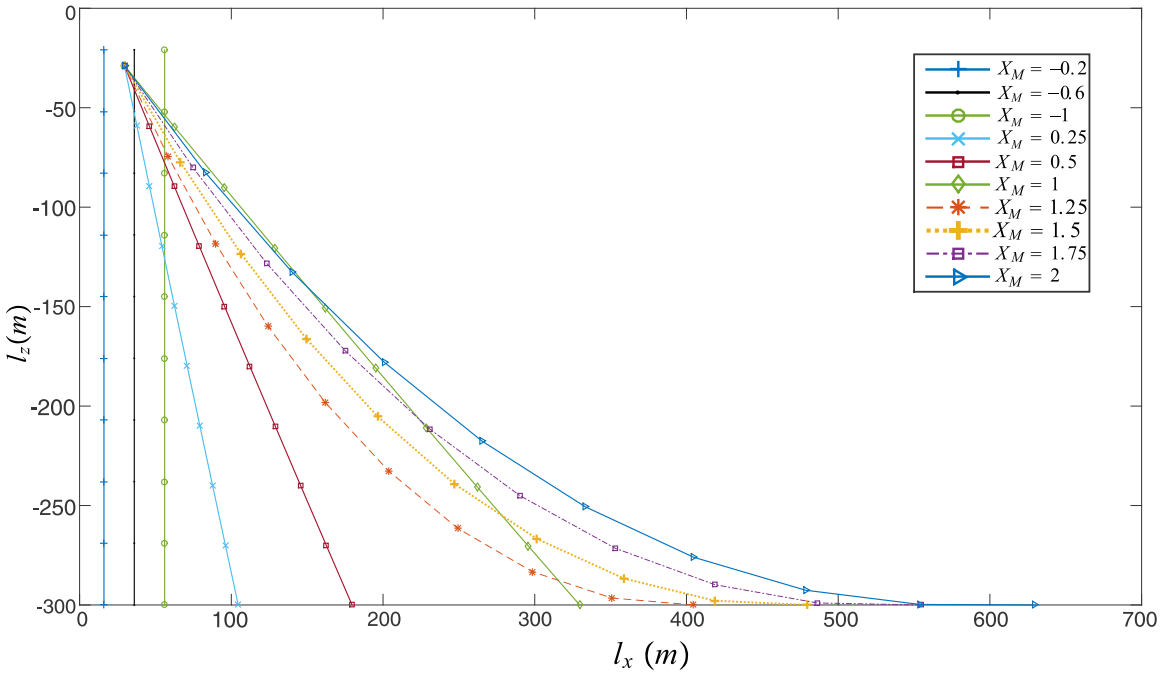

Figure 2.5: Mooring line profiles with 10 nodes for $-1 \leq X_M \leq 2$ in 300 m water depth and variable fairlead locations. l_x and l_z are horizontal and vertical distances from the anchor to the fairlead location

the slack catenary mooring configurations ($1 < X_M \leq 2$), which is noted by Jonkman and Musial [45], is calculated using the following equation:

$$L_u = \sqrt{l_x^2 + l_z^2} + \frac{l_z}{12} \tag{2.10}$$

where l_x and l_z are the horizontal and vertical distances from the anchor to the nominal fairlead location.

Tendon arms

In the design of single-body platforms with taut vertical lines, tendon arms need to be considered in the platform design to hold the fairleads at a distance radially from the platform. The tendon arms are formed by horizontal steel tubes that have a constant wall thickness to radius ratio of 5%. The diameter of these tendon arms are calculated based on the bending moment developed in the steel tubes. The maximum bending

Table 2.2: Design parameters of mooring systems for three specific platform types [4]

Design parameters	**Tension-leg platform**	**Spar buoy platform**	**Multi-body platform**
Mooring technology	Taut vertical line	Angled taut line Slack catenary line	Angled taut line Slack catenary line
X_M Variations	$-1 \leq X_M \leq 0$	$0 < X_M \leq 1$ $1 < X_M \leq 2$	$0 < X_M \leq 1$ $1 < X_M \leq 2$
Line mass density ($\frac{kg}{m}$)	116.027	77.7	113.35
Modulus of elasticity (Pa)	1.18E+09	6E+08	1.66E+09
Line diameter (m)	0.127	0.09	0.076
Line extensional stiffness (N)	1.5E+09	384.243E+06	$(7.536E+08 \times 3/\text{number of lines})$

moment is taken at the root of the tendon arms extensions, and is calculated from the vertical component of the maximum steady-state mooring line tension applied at the fairlead multiplied by a safety factor of 3 [14]. The length of these arms is equal to X_M (negative values for taut vertical lines) multiplied by 50 m. Note that the sizing of the members in this study is based on assuring that they can withstand extreme loads and there is no consideration for fatigue load. Fatigue analysis is proposed as one of the future studies in section 2.7.

2.3.3 Platform mass and ballast

The mass characteristics of each platform are fully specified by the platform geometry, mooring system scheme and the ballast mass. The mass of a cylinder component is modelled using a wall thickness of 50 mm, and heave plate steel thickness is taken to be 30 mm. The total platform mass estimate is formed by superposing the masses of the cylinders, heave plates, truss members and tendon arms using the geometries described earlier and a steel density of 8050 $\frac{kg}{m^3}$.

The ballast mass is set according to the surplus buoyancy of the system which is calculated after subtracting wind turbine weight, platform weight, and vertical component of mooring line tensions from the platform buoyancy force. For taut mooring lines, when $-1 \leq X_M \leq 1$, the configuration is chosen to cancel the surplus buoyancy in the system by increasing the line tension. Therefore, no ballast mass is applied to floating platforms with fully taut mooring systems. For slack mooring

lines, ballast is added from the bottom of deepest cylinder(s) upward, to a common top level across all cylinders, as shown in Fig. 2.6. The ballast material is assumed to be concrete with a density of 2400 $\frac{kg}{m^3}$.

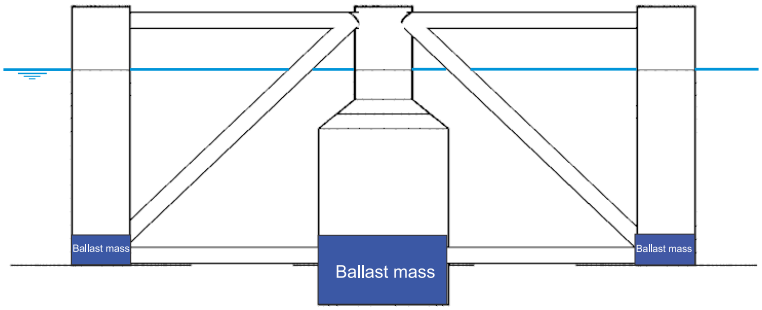

Figure 2.6: Ballast mass distribution for multi-body platforms. In this case, the ballast mass height for the inner cylinder is more than outer cylinders because the inner cylinder draft is more than the draft of outer cylinders, however they are all at a common top level

2.4 Optimization problem methodology

The formulation for a general multi-objective design optimization is defined as:

Find

$$\hat{x} = [x_1, x_2, .., x_k] \tag{2.11}$$

That minimizes

$$\hat{J}(x) = [J_1(x), J_2(x), ..., J_n(x)] \tag{2.12}$$

Subject to

$$\hat{x}_{lower} \leq \hat{x} \leq \hat{x}_{upper} \tag{2.13}$$

$$h_i(x) = 0; \quad i = 1 \text{ to } m \tag{2.14}$$

$$g_j(x) \leq 0; \quad j = 1 \text{ to } p \tag{2.15}$$

where $\hat{x}$ is a k-dimensional vector of design variables with lower and upper bounds, $\hat{J}(x)$ is an n-dimensional vector of objective functions, m is the number of equality constraints, and p is the number of inequality constraints. Note that because $\hat{J}(x)$ is a vector, if all the components of $\hat{J}(x)$ are competing, there is no unique solution for the optimization problem. Therefore, the solution of multi-objective optimization is always situated in a Pareto optimal set [46]. A feasible point x^* in the design space is called Pareto optimal if there is no other point x in the design space that improves one objective function without worsening in another objective [47].

At this study, the multi-objective GA Matlab toolbox is used to achieve optimal design configurations for support platforms. The GA provides a non-gradient nature inspired search method by using clusters of design points around locally-optimal configurations to find a group of optimal solutions for the optimization problem [47]. One of the most distinctive features of this multi-objective GA optimizer, in comparison with other optimizers used for design optimization of FOWTs [14, 21], is finding an evenly distributed set of design points on the Pareto front.

To use the Matlab multi-objective GA optimizer, we provided two objective functions (see section 2.4.1) with design variables constrained by lower and upper bounds (see Tables 2.1 and 2.2), an inequality constraint for limiting cost, and four inequality constraints to improve the performance of the wind turbine (see section 2.4.2). In order to define the design space size, a population of 200 design candidates is used for a maximum of 120 generations before the algorithm stops the design optimization. In addition, a tolerance value of 1E-04 is applied to stop the algorithm if the average relative change in the best fitness function was less than or equal to this value. The optimizer returns a design population including the population of design variables in each generation, and also a design score, that contains the objective function values for each population when the optimizer terminated. More details about GA option

structures and generation of Pareto optimal set can be found in MATLAB [48] global optimization toolbox user's guide.

2.4.1 Objective functions

Although minimizing cost of energy (COE) is the final optimization goal for FOWT technologies, a simpler optimization problem can be used to avoid additional considerations for modeling the wind turbine energy production over its lifetime [33, 49]. Hence, to simplify this design optimization problem, platform and mooring system costs as well as the wind turbine fore-aft nacelle acceleration are used as the objective functions. These objective function metrics serve as proxies for overall costs and technical wind turbine performance in limiting platform motion.

Cost model

The cost function is a combination of floating platform cost, mooring system cost, and anchor cost:

$$C(x) = C_{Platform}(x) + C_{Mooring}(x) + C_{Anchor}(x) \tag{2.16}$$

The floating platform cost is a function of the design variables. This accounts for material costs as well as manufacturing and installation costs. Although the cost per-mass is different for platform cylinders and connections, for simplicity a constant cost of \$2.5 per-kg is used here [12]. The ballast is not costed in this study because of the relatively inexpensive nature of concrete. In order to show how the results of this optimization problem depend on the platform cost, a sensitivity analysis is performed in section 2.6.5. Note that in addition to the extreme loads, considering fatigue loads would further drive platform sizing and consequently platform cost.

The cost of the mooring system is modelled using the total length of the lines and the maximum steady-state mooring line tension which is implemented on the mooring

system. Therefore, the cost model for mooring lines is defined based on a factor of $\$0.42/m-kN$ which is multiplied by the line length and the maximum steady-state line tension [12, 50].

The anchor cost is the third component of the cost model and it is defined by combining the anchor installation and technology costs. The three technologies which are considered for the anchors are drag-embedment anchors, vertical-load drag-embedment anchors (VLAs), and suction piles. Similar to the mooring line cost model, the cost of each technology is modelled based on the maximum steady-state load on the anchors. For each technology, a fixed per-anchor installation cost is also included in the cost model. The anchor type selection is done based on the angle of mooring line at the connection with anchor [12]. All the information of anchor technology and installation cost is summarized in Table 2.3. To show how the optimization results depend on the anchor technology and installation cost, a sensitivity analysis is performed in section 2.6.5.

Table 2.3: Cost model for three anchor technologies

AnchorTechnology	**Line Angle**	**$/anchor/kN (Line tension)**	**$/anchor (Installation)**
Drag embedment	$0^{\circ}-10^{\circ}$	100	50000
VLA	$10^{\circ}-45^{\circ}$	120	80000
Suction pile	$45^{\circ}-90^{\circ}$	150	110000

Wind turbine performance metric

To increase the performance of a floating wind turbine, nacelle acceleration from platform pitch and surge motion needs to be minimized. This motion creates extra loads on the wind turbine blades, causes fatigue in the drivetrain, and decreases the lifetime of the system [49]. In order to formulate this objective function, the linearity of the simplified dynamic system was exploited to define the RAO of nacelle acceleration at each sea state condition. The performance metric for this study is defined as the standard deviation of nacelle acceleration [12]:

$$\sigma_{a_{nac}}(\omega) = \sqrt{\int_0^\infty |RAO_{a_{nac}}(\omega)|^2 S(\omega)\, d\omega} \tag{2.17}$$

where $S(\omega)$ is the spectral density of the waves at prescribed sea states, and $RAO_{a_{nac}}(\omega)$ is the fore-aft nacelle acceleration response amplitude operator. The complex forms of the nacelle displacement RAO and nacelle acceleration RAO are given by the following equations.

$$RAO_{\zeta_{nac}}(\omega) = RAO_1(\omega) + RAO_5(\omega) z_{nac} \tag{2.18}$$

$$RAO_{a_{nac}}(\omega) = -\omega^2 (RAO_1(\omega) + RAO_5(\omega) z_{nac}) \tag{2.19}$$

where z_{nac} is the hub height of the wind turbine. It should be mentioned that the $RAO_{a_{nac}}(\omega)$ contains the aerodynamic effects implicitly from the linearized dynamic quantities of the wind turbine (Eqs. 2.4 to 2.6). An example to illustrate how the overlap of the $RAO_{a_{nac}}$ and sea state spectral density, $S(\omega)$, produces a response spectrum is shown in Fig. 2.7.

2.4.2 Design constraints

The final stage in the mathematical formulation of the design process is implementing design restrictions called constraints. In addition to the lower and upper bounds on the design variables discussed in section 2.3, different constraints are applied to each objective function.

Cost constraint

To avoid expensive design configurations, a cost constraint is applied to the optimization problem. This inequality constraint restricted the cost of the platform to less than $9 M.

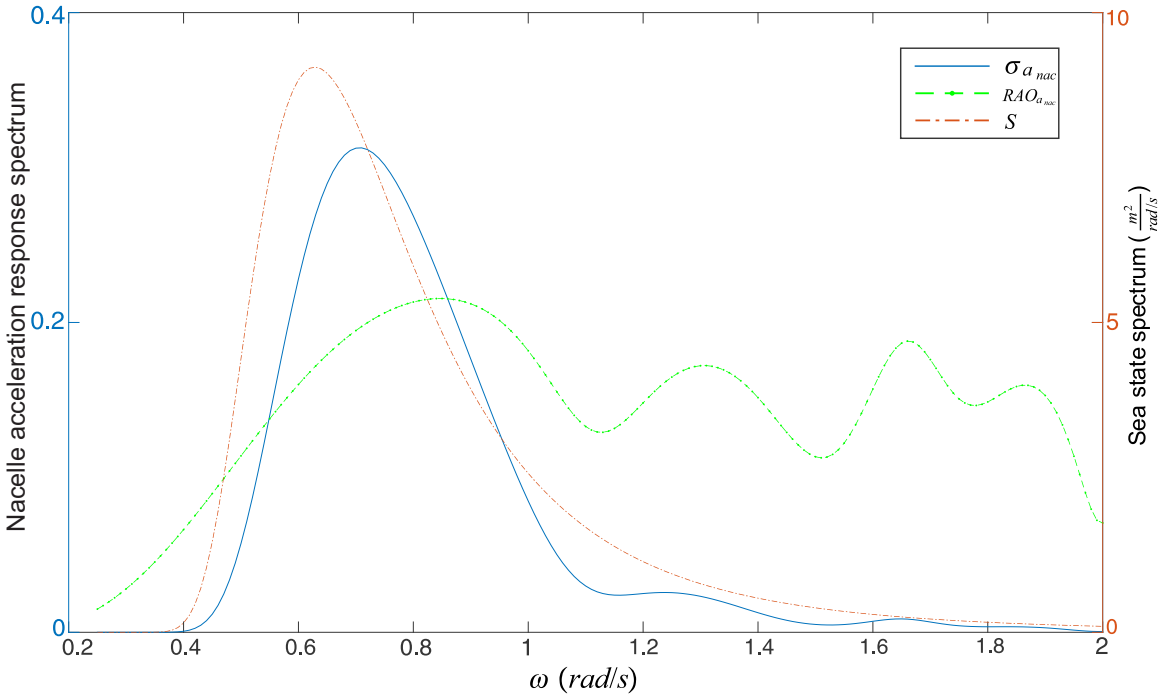

Figure 2.7: An example of spectral analysis for a floating wind turbine. This figure shows the overlap of nacelle acceleration RAO and sea state spectrum to create the wind turbine response spectrum

Performance constraints

To keep the platform and wind turbine stable, the maximum allowable nacelle acceleration is limited to 1 $\frac{m}{s^2}$. Moreover, one of the critical quantities in the design of FOWTs is the static stability of the platform during operation. In order to avoid over-turning of the platform, and also to achieve the required wind turbine performance, the steady-state pitch angle of the floating structure should be less than 10 degrees [21]. The expression to represent this constraint is given below:

$$\bar{\zeta_5} = \frac{F_{thrust}.z_{nac} + M_{mooring_5} - M_{ballast}}{\rho g \forall z_{CB} - M_t g z_{CG} + \rho g I_{xx} - C_{mooring_{5,5}} + C_{5,1} z_{fair}} < 10^{\circ} \tag{2.20}$$

where F_{thrust} is the steady thrust load of the wind turbine, $M_{mooring_5}$ is the mooring line pitching moment at the maximum wind turbine thrust, $M_{ballast}$ is the pitching moment due to stabilizing ballast mass, $\forall$ is the platform displacement, z_{CB} is the

center of buoyancy location, M_t is the total mass of the system, z_{CG} is the center of gravity location, I_{xx} is the platform water plane moment of inertia in pitch motion, $C_{mooring_{5,5}}$ is the mooring lines stiffness in pitch motion, $C_{5,1}$ is the mooring line stiffness in pitch-surge motions, and z_{fair} is the fairlead depth in pitch motion. To evaluate this constraint for the NREL 5 MW wind turbine reference model, a maximum thrust load of 800 kN with hub height of 90 m are selected as design constants.

Similar to the static pitch angle consideration, the dynamic pitch angle of the platform should not exceed the operating limit designated for a floating wind turbine [14]. The final form of the constraint is based on the combination of the steady-state pitch angle (Eq. 2.20) plus the standard deviation of the platform pitch motion as shown in Eq. 2.21:

$$\bar{\zeta_5} + \sigma_{\zeta_5} < 10^\circ \tag{2.21}$$

For platforms with taut mooring lines, loss of tension followed by snap loading cause them to fail. To avoid this issue, a slackness constraint, first suggested by Tracy [14]:

$$T_{line} - 3\sigma_{T_{line}} > 0 \tag{2.22}$$

where T_{line} is the line tension calculated by the mooring model at equilibrium, and $\sigma_{T_{line}}$ is the standard deviation of the mooring line tension calculated from the RAO of line tension. This three-sigma approach is an approximation in line with the level of fidelity in the overall framework, designed primarily to capture the proportionalities between device motions and mooring system loads. More refined estimation of mooring tensions incorporating carefully chosen statistical methods and the inclusion of dynamic contributions to mooring tension is available in the study of Hall et al [51].

2.5 Time-domain verification of dynamic model

To verify the frequency-domain dynamic model framework, FAST was used as a higher fidelity time domain model to evaluate two platform designs–a TLP and a spar buoy platform. Design parameters for these two platforms are summarized in Table 2.4. The mooring line properties for each design can be implemented directly in the FAST input file based on the platform dimension and the mooring system parameterization discussed in section 2.3.2. The hydrodynamic coefficients generated by WAMIT can also be used directly for the FAST simulations. Note that in this section, a comparison of the frequency-domain model and a FAST time-domain model for a semi-submersible platform configuration would be less informative because truss members are neglected in the generation of the WAMIT file (as discussed in section 2.2.2) and thus the inviscid effects associated with these components would not manifest in the FAST simulation.

Table 2.4: Design parameters for a TLP and a spar buoy platform

Design parameters	**Tension-leg platform**	**Spar buoy platform**
Draft (m)	48	48
Diameter (m)	18	16
$m_{platform}$ (tonnes)	8.6E+06	9E+06
Center of mass (m)	40.61	36.32
I_4 (kg-m^2)	5.71E+08	1.34E+10
I_5 (kg-m^2)	5.71E+08	1.34E+10
I_6 (kg-m^2)	3.61E+08	3.27E+08

For environmental conditions, a steady wind of 12 m/s and a Jonswap wave spectrum with significant wave height of 3.4 m and peak period of 8.7 s was used. The water depth was taken to be 300 m. A total run time of 25 minutes with integration time step of 0.0125 s is used for each FAST simulation. To avoid start-up transients, the first 5 minutes of data is excluded from the analysis. In Table 2.5, comparing the RMS of nacelle accelerations, $\sigma_{a_{nac}}$, from the frequency-domain dynamic model

and FAST time domain simulation, there is a good agreement for the TLP design. However, the difference between the $\sigma_{a_{nac}}$ values calculated from the two models is more significant for the spar buoy platform. The difference in the spar buoy case is likely caused by neglecting the tower flexibility in the frequency-domain model as well as by variations in the surge and pitch motions between two models (see Table 2.5). In any case, in the final results presented in the next section, the comparison of platform types means that the frequency-domain predictions are conservative in their performance (i.e. likely underpredicted acceleration) and are therefore a fair comparison between platform types.

Table 2.5: Comparison of frequency- and time-domain results

Objective parameters	**Tension-leg platform**			**Spar buoy platform**		
	FAST	**Dynamic model**	**Variation (%)**	**FAST**	**Dynamic model**	**Variation (%)**
σ_{surge} (m)	0.25	0.23	8.33	0.32	0.28	13.33
σ_{pitch} (deg)	0.12	0.16	28.57	0.17	0.18	5.71
$\sigma_{a_{nac}}$ (m/s^2)	0.28	0.27	3.63	0.34	0.32	6.06

2.6 Results

To this point, a parametrization scheme has been presented that allows the geometry of the candidate design to be automatically generated; a linear dynamic model of the design has been proposed and this model can be used to assess the performance of the candidate; the cost required to achieve that level of performance can be assessed using the cost models for the platform, mooring and anchor components. Using the optimization algorithm, an automated search of the entire design space could be executed. However, to fully elucidate the cost-performance trade-offs within each of the three classes considered, and respecting that the dynamic model's estimates of performance may have varying accuracy across the three classes, it is prudent to complete the optimization in stages that are restricted to one platform class. Consequently, the optimization results are divided according to TLPs, spar buoy platforms, and semi-

submersibles. The results from each stage are discussed separately in the following subsections followed by a comparison of the individual class-specific Pareto fronts.

2.6.1 Environmental conditions

In this study, a water depth of 300 m is applied universally. Three sets of steady wind speeds, 8 m/s, 12 m/s, and 18 m/s are considered for calculation of aerodynamic loading on the NREL 5 MW wind turbine. The reason for considering steady winds is that we are primarily concerned with locating platform designs with reduced sensitivity to wave loads rather than aerodynamic loads. Moreover, an irregular sea state is included based on a Jonswap wave spectrum with significant wave heights of 2.5 m, 3.4 m, and 4.9 m which correspond to the three wind speed conditions. The peak periods for these wave spectra are 7.1 s, 8.7 s, and 11.2 s respectively [52]. The spectral discretization of the waves is at a resolution of 0.027 rad/s over the range $0.25 \leq \omega \leq 2$ rad/s. For the sake of evaluating the FOWT performance, the final fitness value is the average of the performance objective function calculated for the three environmental conditions. While this is not a complete set of environmental conditions by any means, using above and below-rated wind and wave conditions provides a reasonable proxy of typical operating conditions in order to evaluate floater stability.

2.6.2 Single-body platforms

Two conventional types of floating platforms for FOWTs are the TLP and spar buoy platforms. To define these single-body structures, a cylindrical element is used in the design optimization of these platforms. For TLPs, the four variables defining the design optimization are cylinder draft, H_I, cylinder radius, R_I, taper ratio, T_I, and type of mooring line, $-1 \leq X_M \leq 0$. In addition, two pairs of tendon arms (see Fig. 2.1(a)) are needed for the TLP design. This is done by defining each tendon arm length, L_T, and radius, R_T. The design parameterization scheme for the catenary

moored spar buoy platform type is similar to the TLP except with $0 < X_M \leq 2$, and without tendon arms at the bottom of platform.

Figure 2.8 illustrates the multi-objective design space for the single-body platforms in terms of platform cost and nacelle acceleration. The Pareto front of each design class is along the lower-left boundary of the design points. The visualization of a group of optimal platform candidates is also shown in Fig. 2.8. The geometry of each labelled platform is summarized in Table 2.6.

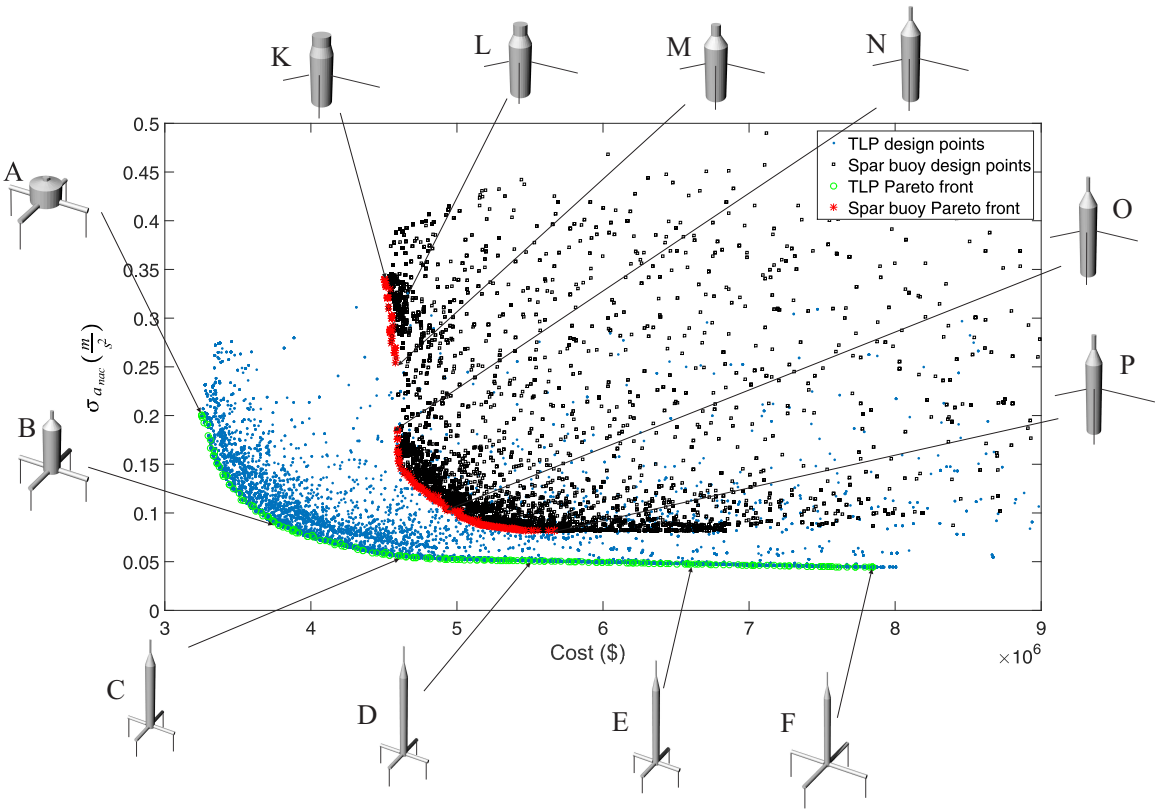

Figure 2.8: Design exploration of single-body platforms including TLPs and spar buoys. The Pareto fronts, which show the optimal design points, presented at the lower left of each design space

As can be seen from Fig. 2.8, TLPs are found to be the most cost effective and stable structures in the class of the single-body platform candidates. The design space shows the lowest platform cost for TLPs, platform A, with minimum acceptable stability and a cost of \$3.25 M. The results also give the most expensive floating

structure, platform F, with the maximum performance among all the evaluated TLPs. From the details of each TLP design (Table 2.6), it is apparent that there is a consistent trend along the design parameters as the cost increases. This trend shows draft increasing and the radii decreasing as cost increases. For the platform stabilization, mooring line tension increases are required with longer tendon arms and hence bigger diameters. Presumably, the more slender floats are improving the performance by reducing the platform's sensitivity to wave excitation. For the spar buoy configurations, platform K is the most cost effective design point, at \$4.5 M, with the minimum platform stability, and platform P is the best design from the standpoint of wind turbine performance (minimum nacelle acceleration). The trend apparent in the spar buoy optimal design candidates is the dominance of two design parameters, a slack catenary mooring system and increasing cylinder draft, as the platform stability improves.

Table 2.6: Platform characteristics for single-body designs including platform geometries, design parameters, and the calculated value for objective functions

Design parameters		Tension-leg platforms						Spar buoy platforms					
		A	B	C	D	E	F	K	L	M	N	O	P
Draft (m)	H_I	18.37	48.80	83.14	83.75	83.75	83.73	43.40	47	49.01	51.94	77.87	91.35
Radius (m)	R_I	6.16	3.95	3.13	3.02	3.02	3.02	8.91	8.93	8.91	8.89	6.61	6.12
Taper ratio	T_I	0.25	0.20	0.21	0.21	0.21	0.21	0.83	0.62	0.52	0.28	0.20	0.20
Mooring line type	X_M	-0.29	-0.32	-0.33	-0.46	-0.62	-0.78	1.96	1.98	1.97	1.92	1.97	1.80
Tendon arm length (m)	L_T	14.5	16	16.5	23	31	39	N/A	N/A	N/A	N/A	N/A	N/A
Tendon arm radius (m)	R_T	1.30	1.35	1.42	1.72	1.96	2.05	N/A	N/A	N/A	N/A	N/A	N/A
Platform cost (million \$)	$Cost$	1.58	2.18	2.99	3.86	5.04	6.35	3.72	3.78	3.83	3.79	4.23	4.81
Mooring system cost (million \$)	$Cost$	0.74	0.66	0.63	0.62	0.57	0.56	0.55	0.54	0.53	0.56	0.50	0.59
Anchor cost (million \$)	$Cost$	0.93	0.94	1.03	1.01	0.95	0.93	0.23	0.22	0.21	0.23	0.20	0.26
Overall cost (million \$)	$Cost$	3.25	3.78	4.65	5.49	6.56	7.84	4.50	4.54	4.57	4.58	4.93	5.66
Nacelle acceleration (m/s^2)	$\sigma_{a_{nac}}$	0.20	0.08	0.5	0.05	0.04	0.04	0.33	0.28	0.25	0.18	0.10	0.08

The results for the performance of single-body platforms are provided here for a group of optimal design candidates. Figure 2.9 displays the spectral nacelle acceleration graphs based on surge and pitch modes of motion that are excited for the TLP and spar buoy platforms. The smooth single peaks in the frequency response reflect the influence of sea state spectrum on the RAOs of the platforms. The lower peaks of

the graphs indicate the more stable structures. Figure 2.9 also shows that by increasing the stability of the platforms, the curve peaks shift towards lower frequencies.

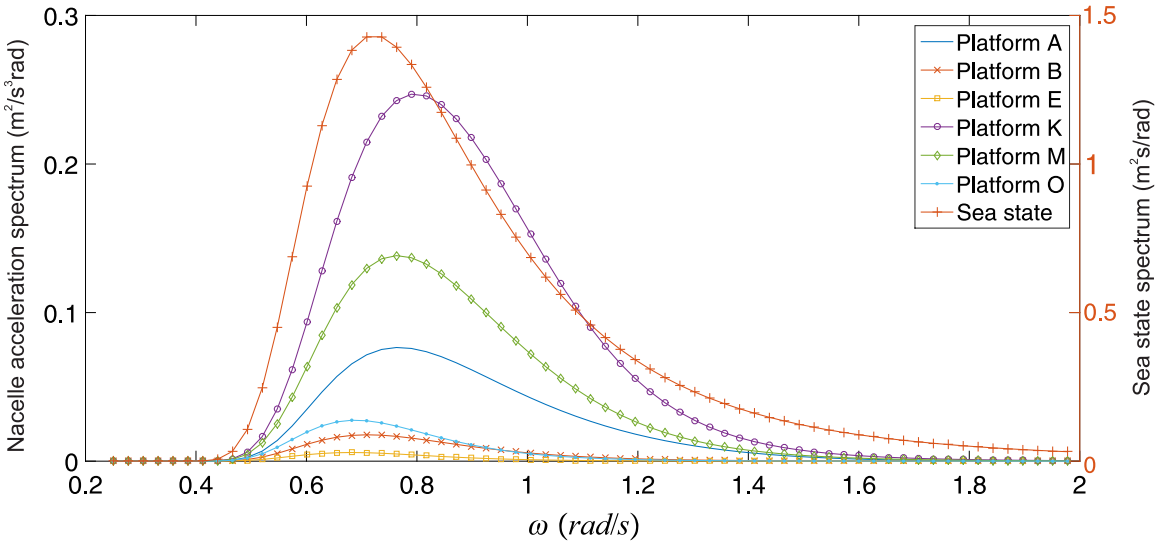

Figure 2.9: Nacelle acceleration spectrum for a group of single-body design candidates in a sea state. The area under each graph shows the variance of nacelle acceleration for each platform design

2.6.3 Multi-body platforms

This section focuses on the optimization results for semi-submersible platforms. The multi-body structures are formed by a main inner cylinder with an array of vertical cylinders around the inner float as discussed in section 2.3. A visualization of the domain exploration and Pareto optimal results are provided in Fig. 2.10.

For semi-submersible design configurations with four floats, the Pareto optimal points are distributed between costs of \$2.5 M and \$4.5 M. From Fig. 2.10, it can be seen that platforms $A^{'}$ and $F^{'}$ represent the lowest and highest structural costs respectively with inversely varying performance. The details of the optimal design points for four float semi-submersible platforms (see Table 2.7) show that heave plates are used in all design cases and the mooring line type is a taut system with non-vertical

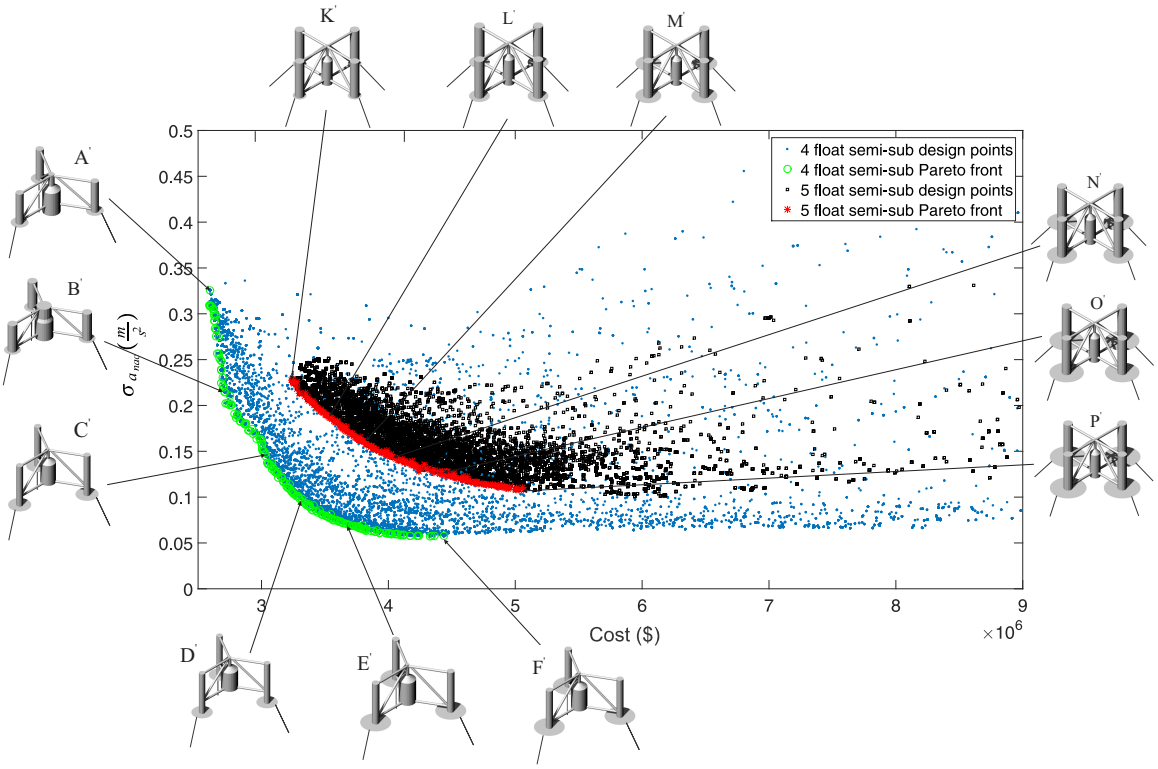

Figure 2.10: Design exploration for multi-body platforms including semi-submersibles with four and five floats. The Pareto front at the lower left of each design space displays the optimal design points

lines for all of the Pareto points. The cylinders' draft also increases and taper ratio drops quickly before becoming steady as stability of the structure improves.

Designs with five total floats in Fig. 2.10 are indicated by representative platforms K' to P'. The mooring system transitions from a slack catenary configuration to a taut system with non-vertical lines as the cost increases. It seems that for this form of semi-submersible platform, heave plates are more effective than cylinder draft at reducing the nacelle acceleration of the wind turbine. Table 2.7 shows the inner and outer cylinders' draft getting deeper and their radius becoming smaller as cost increases, so the platform water plane area decreases (i.e. reducing sensitivity to incident waves).

Results for the semi-submersible platforms with five cylinders arrayed around a central cylinder are shown in Fig. 2.11. The Pareto front for this class of design

Table 2.7: Platform characteristics for four and five float semi-submersible designs including platform geometries, design parameters, and the calculated value for objective functions

Design parameters		Four float semi-sub platforms						Five float semi-sub platforms					
		$A^{'}$	$B^{'}$	$C^{'}$	$D^{'}$	$E^{'}$	$F^{'}$	$K^{'}$	$L^{'}$	$M^{'}$	$N^{'}$	$O^{'}$	$P^{'}$
Inner cylinder draft (m)	H_I	8.41	8.33	14.04	17.18	17.73	18.95	9.50	11.08	11.25	12.03	13.16	13.46
Inner cylinder radius (m)	R_I	7.05	6.64	6.22	5.91	5.84	5.99	7.90	6.82	6.91	6.65	6.19	4.43
Taper ratio	T_I	0.37	0.87	0.26	0.28	0.20	0.29	0.28	0.27	0.27	0.26	0.26	0.29
Radius of array (m)	R_F	27.99	27.80	28.67	27.70	28.40	28.07	20.91	21	20.89	20.87	20.30	20.18
Outer cylinders draft (m)	H_O	5.53	5.68	7.5	9.71	15.63	19.03	13.35	14.73	14.73	15.27	17.16	18.44
Outer cylinders radii (m)	R_O	2.82	2.57	2.34	2.01	2.03	2.08	2.52	2.6	2.65	2.74	2.80	3.34
Truss members radii (m)	R_T	0.58	0.58	0.62	0.64	0.66	0.71	0.48	0.53	0.53	0.55	0.58	0.67
Heave plates radii (m)	R_{HP}	3.01	3	6.42	7.81	8.78	9.34	3.89	5.87	7.78	8.99	10.66	11.63
Mooring line type	X_M	0.53	0.53	0.48	0.49	0.45	0.39	1.20	1.18	1.18	1.18	1.16	1.16
Platform cost (million \$)	$Cost$	1.85	1.94	2.17	2.34	2.72	3.15	2.55	2.81	3.05	3.33	3.78	4.44
Mooring system cost (million \$)	$Cost$	0.36	0.37	0.41	0.44	0.47	0.59	0.43	0.43	0.43	0.43	0.43	0.43
Anchor cost (million \$)	$Cost$	0.38	0.38	0.43	0.47	0.50	0.69	0.25	0.24	0.24	0.24	0.25	0.25
Overall cost (million \$)	$Cost$	2.59	2.69	3.01	3.25	3.69	4.43	3.23	3.48	3.72	4	4.46	5.12
Nacelle acceleration (m/s^2)	$\sigma_{a_{nac}}$	0.32	0.22	0.15	0.10	0.06	0.05	0.22	0.19	0.16	0.14	0.12	0.10

shows a gap in optimal points which represents the high sensitivity of the performance function as the cost of the structure increases. Platforms $Q^{'}$ and $V^{'}$ are the design candidates for the minimum cost and maximum performance respectively. The upper points of the Pareto set show the structures are moored with slack catenary systems, while the lower more optimal design points use taut mooring system with non-vertical lines attached to the fairlead. Similar to the semi-submersible platforms with five floats, heave plates of the platform candidates with six floats are more effective than other design parameters to improve the stability of the floating structure. The complete geometrical properties of this platform class for some representative design points are presented in Table 2.8.

Figure 2.12 displays nacelle acceleration spectra for a group of semi-submersible platforms in the frequency-domain across a range of float configurations (e.g. 4, 5 and 6 float designs). To compare the performance of different designs, the area under each graph, which represents the variance of nacelle acceleration in pitch and surge motion, has to be calculated. As such, performance can be seen to degrade with increasing peak height, with increasing width of the peak, or when the curve develops a second

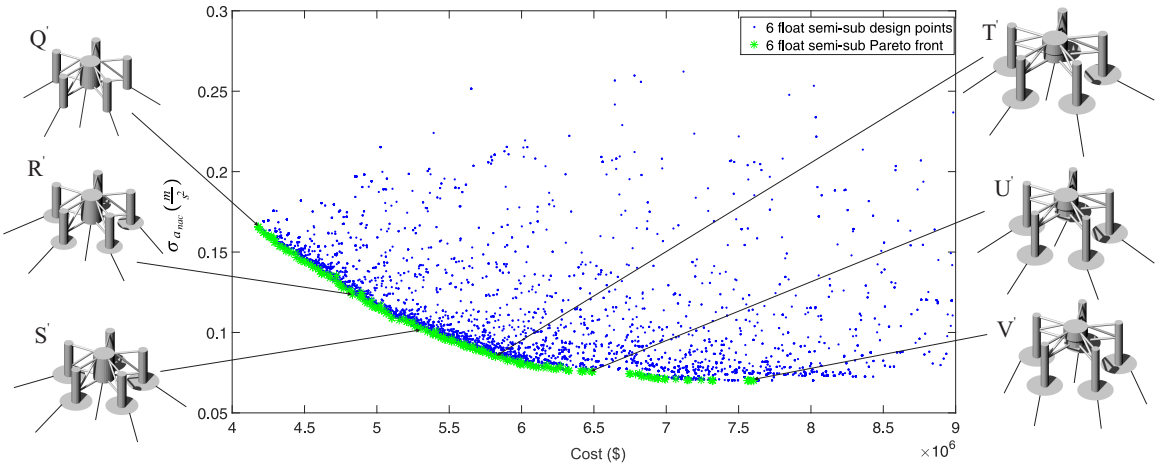

Figure 2.11: Design exploration for multi-body platforms including semi-submersibles with six floats. The Pareto front at the lower left of each design space displays the optimal design points

peak. The results for the five and six float semi-submersibles (designs $K^{'}$, $M^{'}$, $O^{'}$, $Q^{'}$, $S^{'}$ and $V^{'}$ in Fig. 2.12) show that there are two shapes of nacelle acceleration spectra being realized for optimal design candidates. Concurrent with this change in spectral response, the type of mooring system changes between five and six float semi-submersible designs. Figure 2.12 shows that platforms with taut mooring lines ($0 < X_M \leq 1$) have smooth single peaks in the frequency response, whereas platforms with slack catenary mooring system ($1 < X_M \leq 2$) have multi peaks and complex behaviours.

2.6.4 Full design space exploration

The Pareto fronts across all design classes are shown together in Fig. 2.13. Looking at the optimal design points, one can see that the TLPs and four float semi-submersible platforms are the most optimal designs across all the platforms. To find a design point at a lower cost and the same performance with TLPs, there is a region at $\sigma_{a_{nac}} \in [0.05, 0.2]$ for semi-submersible designs with one central cylinder and an array of three outer cylinders. The results also show that the TLPs and semi-submersible platforms are more stable and cost effective than spar buoy design configurations. Among the

Table 2.8: Platform characteristics for six float semi-submersible designs including platform geometries, design parameters, and the calculated value for objective functions

Design parameters		Six float semi-submersible platforms					
		$Q^{'}$	$R^{'}$	$S^{'}$	$T^{'}$	$U^{'}$	$V^{'}$
Inner cylinder draft (m)	H_I	13.23	11.97	12.55	12.60	13.59	13.89
Inner cylinder radius (m)	R_I	4.96	4.76	4.73	4.06	3.89	3.80
Taper ratio	T_I	1.04	1.07	1.17	1.48	1.72	1.80
Radius of array (m)	R_F	20.51	21.13	21.43	22.27	24.03	24.30
Outer cylinders draft (m)	H_O	16.23	16.44	18.80	20.34	22.60	22.73
Outer cylinders radii (m)	R_O	2.74	2.94	2.89	2.91	2.83	2.83
Tendon arms radii (m)	R_T	0.59	0.61	0.64	0.68	0.73	0.74
Heave plates radii (m)	R_{HP}	3.47	7.20	8.92	9.98	10.34	10.24
Mooring line type	X_M	1.31	1.32	1.31	1.30	1.21	0.44
Platform cost (million \$)	$Cost$	3.54	4.10	4.65	5.22	5.78	5.84
Mooring system cost (million \$)	$Cost$	0.43	0.42	0.41	0.41	0.45	0.80
Anchor cost (million \$)	$Cost$	0.21	0.21	0.22	0.21	0.25	0.92
Overall cost (million \$)	$Cost$	4.18	4.73	5.28	5.84	6.48	7.56
Nacelle acceleration (m/s^2)	$\sigma_{a_{nac}}$	0.16	0.13	0.10	0.08	0.07	0.6

multi-body structures, it seems that semi-submersibles with four floats are the best option below a cost of \$4.5M. It is necessary to mention that in this study, the most promising candidates are not simply designs lying on fronts farthest to the bottom left in Fig. 2.13–designs that are optimal within their class should also be pursued in the detailed design stage.

2.6.5 Sensitivity analysis

In order to investigate the impact of cost model assumptions on comparisons of platforms across the full design space, two additional optimization studies were performed to expose the sensitivity of the Pareto fronts to the parameters of cost model. Note that the dynamic model parameters were unchanged in the additional studies and a complete optimization was performed to explore a new design space for the three classes of platform. Platform cost, which accounts for material costs as well as manufacturing and installation costs was adjusted in one of the additional studies, and

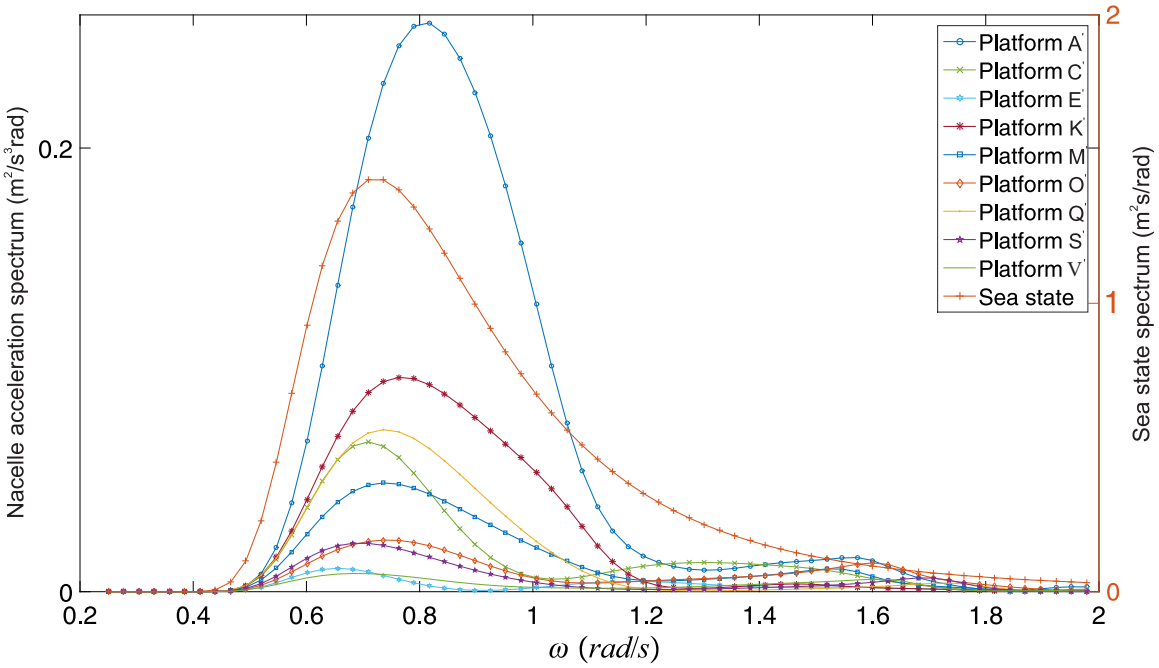

Figure 2.12: Nacelle acceleration spectrum for a group of multi-body design candidates in a sea state. The area under each graph shows the variance of nacelle acceleration for each platform design

anchor cost was adjusted in the other. Figure 2.14 shows the results of a full design space exploration for a 10% increase in the platform material cost of \$2.5 per-kg (see section 2.4.1). Although the Pareto fronts move toward higher costs overall, the trace of the optimal designs follows the general trend observed in Fig. 2.13 and there is no change in the predominant classes-TLPs and four float semi-submersible platforms remain preferred candidates.

In the second run, a 50% increase was applied to each of the parameters reported in Table 2.3 and the results are presented in Fig. 2.15. The shifted set of Pareto fronts shows that the effect of this change on the TLPs is more tangible than other platforms, as would be expected. Comparing Fig. 2.13 to Fig. 2.15, the four float semi-submersible platforms remain a preferred design class except for very marginal stability improvements at high cost. With increased anchor costs, the five float semi-submersible platforms move to dominate the TLPs at lower cost levels.

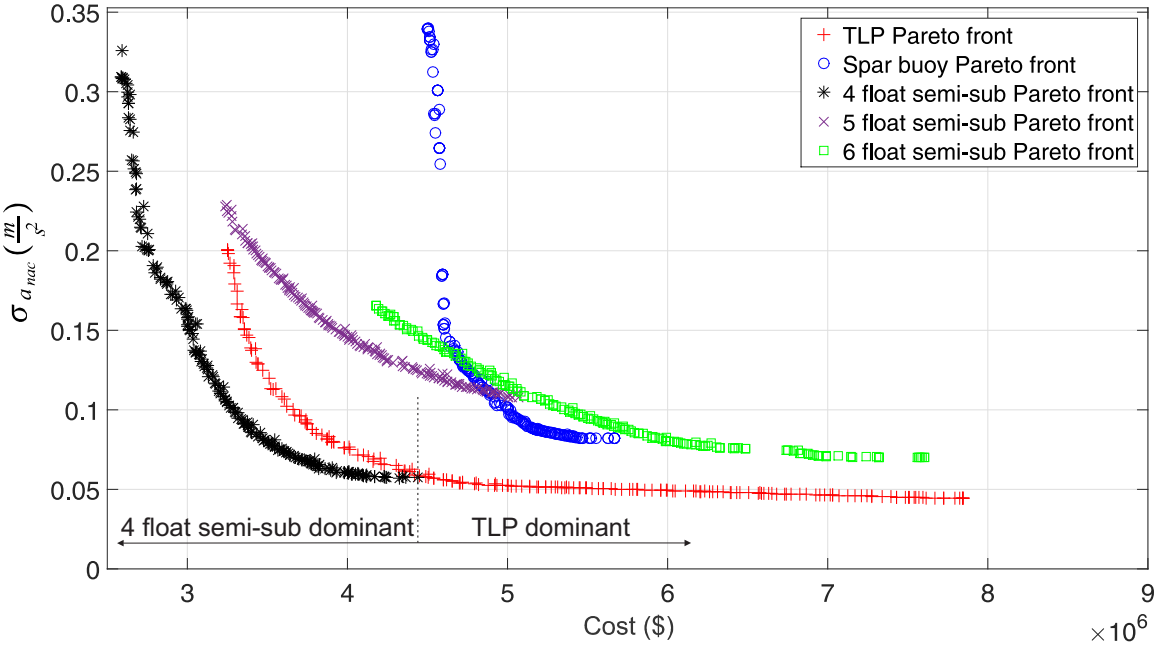

Figure 2.13: Full design Pareto optimal sets for five group of platform designs including TLPs, spar buoys, and three classes of semi-submersibles. This figure also shows the cross-over point between TLPs and semi-submersible optimal platform designs

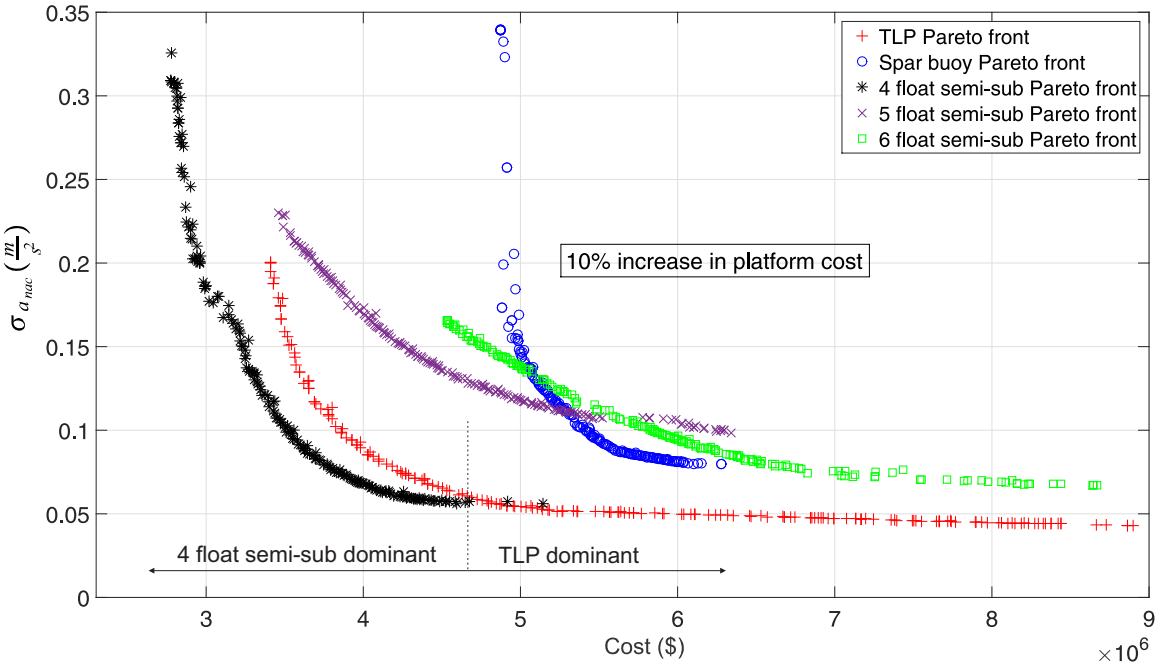

Figure 2.14: Sensitivity analysis for five group of platform designs including TLPs, spar buoys, and three classes of semi-submersibles with 10% increase in platform cost. This figure shows the cross-over point between TLPs and semi-submersible optimal platform designs

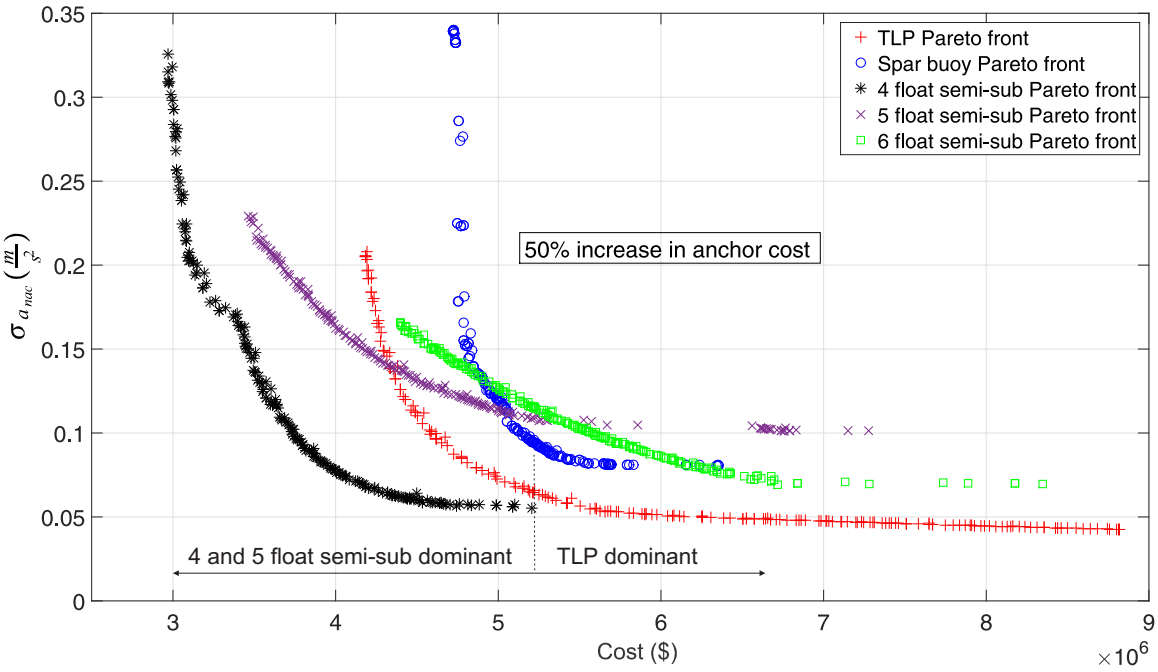

Figure 2.15: Sensitivity analysis for five group of platform designs including TLPs, spar buoys, and three classes of semi-submersibles with 50% increase in anchor cost. This figure shows the cross-over point between TLPs and semi-submersible optimal platform designs

2.7 Conclusions and future work

In the past years, many studies have been carried out to develop and optimize the support structures of floating wind turbines. However, only a few have applied a global design optimization approach, and those only examined single-body platforms subject with a single objective function. These formulations therefore potentially missed large regions of the design space as a wide range of design configurations were not considered, and objective function trade-offs could not be properly compared. This limitation in previous works is mainly because of the level of complexity in modeling and simulating multi-body platforms, as well as the hydrodynamic and aerodynamic analyses of FOWT components. The work presented herein was a step forward in a design optimization study that simultaneously considers a wide range of platform designs for an offshore wind turbine subject to the cost and performance objective functions and constraints.

In this research, in order to carry out a global optimization, a multi-objective GA was selected to represent the entire design exploration and optimal points. A combination of a cost model and dynamic model were used to define the economic and engineering performance of the platforms. A linearized hydrodynamic model computed loads on the platform, together with a quasi-static mooring system model, and a linear representation of the NREL 5 MW wind turbine under specific environmental conditions. The goal of this optimization was explore the cost implications of platform stability, expressed through the nacelle acceleration objective function, across the three FOWT platform stability classes.

The results for optimized TLPs, spar buoys, and semi-submersible platforms lead to Pareto fronts with widely distributed optimal design points. As seen in Fig. 2.13, TLPs and semi-submersibles with three outer cylinders are the best options below a cost of $4.5 M. Above this cost, TLPs are the optimal platforms but achieve only modest performance improvements with exponentially increasing costs. Sensitivity analysis of the optimization revealed high sensitivity of the TLP designs to changes

in the cost model. The results offer insight into designs away from spar buoy designs which were one of the first proposed platforms for floating wind turbines [53] and that have found commerical deployment. It is very important to note though that this work is a preliminary exploration across the full design space, focusing only on acceleration minimization versus cost, rather than a direct minimization of cost of energy. Different environmental conditions using the same optimization approach would also likely lead to new optimal design configurations, as would model fidelity refinements.

There are a number of avenues for improving the methods used in this work, including parameterization extensions, cost model improvements, a comprehensive sensitivity study for the model parameters, and improvements to the dynamic model, structural analysis, and environmental conditions. The cost models could be extended to include wind turbine and balance of plant cost as well as financial models to estimate levelized cost of energy. In order to improve the fully coupled dynamic model of the floating structure, the mooring system should include dynamic mooring line loads, second-order wave loads, and turbulent wind impacts. In particular, the wind turbine model needs to be interactive with the platform motion and include turbulence inflow, in turn impacting rotor structural life and costs. It would also be possible to expand the design space, by defining more flexible design variables to create other support structures such as the Sway's floating wind turbine concept [3] and Fukushima FORWARD (see http://www. fukushima-forward. jp). Future efforts are therefore directed at extending the current framework to include turbine design variables and a wide set of design conditions, yielding structural performance and cost esimates to ultimately compute cost of energy as the objective function. The frequency-domain approach will be retained for computational efficiency, but benchmarked against time domain simulations to ensure validity across the design space.

Chapter 3

A Fully Coupled Frequency Domain Model for Floating Offshore Wind Turbines

This paper has passed the first stage of review in the Journal of Ocean Engineeing and Marine Energy.

Karimi, Meysam, Brad Buckham, and Curran Crawford, "A fully coupled frequency domain model for floating offshore wind turbines".

This chapter presents a new fully coupled frequency domain modeling approach for floating offshore wind turbines using the linearized aerodynamic and hyrodynamic characteristics of the floating system. The unique characteristic of the proposed dynamic model is incorporating the turbulent wind and irregular wave loads in the frequency domain model using wind and wave power spectral density functions. The focus in this chapter is on verification of the proposed approach through comparing the results generated for each of the three baseline platforms using time domain models. The proposed dynamic model in this chapter is then applied to the comprehensive MDO study presented of FOWTs presented in Chapter 4.

Abstract This chapter presents a new frequency domain modelling approach for floating offshore wind turbines with coupled wind turbine, floating platform, and mooring system sub-models. The sub-models are generated by using the validated numerical tools FAST and WAMIT to obtain the frequency domain aerodynamic and hydrodynamic characteristics respectively for any given design candidate. The turbulent wind and irregular wave loads are incorporated in the frequency domain model using wind and wave power spectral density functions, the JONSWAP and Kaimal spectra respectively. To verify the proposed 6 DOF frequency domain framework across standard operational environmental conditions, predicted system responses of a 5 MW NREL offshore wind turbine with three classes of baseline platforms including the OC3-Hywind, the MIT/NREL TLP, and the OC4-DeepCwind semisubmersible were compared to the outputs of 6 DOF and 22 DOF FAST time domain simulations. The comparison over an aggregate of eleven environmental conditions (a total of 220 minutes of time series data) focused on differences in predicted platform rigid body motions and structural considerations including platform surge, roll, and pitch, and rotor thrust, total blade root and tower base bending moments/fatigue loads, fairlead and anchor tensions/fatigue loads. In terms of platform motions, the worst match of frequency and time domain model predictions was seen for the OC4-DeepCwind semisubmersible with errors of 13.2% in peak displacement values. The frequency domain model predictions of rotor thrust, blade root and tower base bending moments demonstrated the largest error in the case of the OC3-Hywind spar buoy with the peak loads differing by up to 12.8%. Errors in the predictions of maximum fairlead and anchor tensions were less than 11.5% with maximum error occurring for the MIT/NREL TLP. In terms of fatigue load comparison, the blade root and tower base fatigue load predictions showed less than 9.8% errors for all the baseline platforms. Comparison of the fairlead and anchor fatigue loads showed errors were less than 13.8% with the largest error seen for the OC3-Hywind spar buoy platform. Overall, the frequency domain model provides reliable means for assessing platforms dynamics

at the conceptual stage of the design process.

keywords Wind turbine, Offshore, Floating platform, Frequency domain model

3.1 Introduction

In the past decade, simultaneous efforts to electrify and decarbonize the world's energy systems have intensified efforts to develop renewable energy technologies. Among renewable options, wind energy is being exploited as a leading alternative to fossil fuels [1]. One of the technologies that can contribute to wind energy harvesting in deep water (water depth $>$ 60 m) is the floating offshore wind turbine (FOWT). Although shallow sites close to the shore have already been exploited as the most accessible locations for installing offshore wind turbine technology, the trend is toward building FOWTs in deep waters [54–56]. Consequently, the study of moored FOWT support structures requires the development of computational models that can predictively assess the coupled platform-turbine system dynamics, performance, and survivability. This work is focused on a methodology using a frequency domain dynamics modeling approach for FOWTs: one which can quickly provide insight on system performance using the frequency domain coupled aerodynamics, hydrodynamics, and structural dynamics to calculate the overall system response to turbulent wind and irregular wave loads.

It is common to use time domain tools in the design and analysis of FOWTs. Hence, most recent studies have focused on extending these time domain simulation tools to model the hydrodynamic loading, mooring lines, and motion of floating wind turbine support structures [7–9, 57, 58]. Time domain tools play a vital role in analysis of specific FOWT designs; simulation data is used to fine tune design features, control strategies, assess power conditioning requirements, and check fatigue loads in faulty operations and extreme events. In addition, the non-linear aerodynamic and hydrodynamic interactions between floating platform and wind turbine, non-linear

viscous drag forces, and mooring line dynamics need to be solved using a time domain equation of motion.

However, ahead of such detailed design refinement studies, a simple faster model is still needed to assess and compare the myriad combinations of floating platform, mooring, tower and blade dynamics. Coupling the simpler, yet sufficiently accurate, model with an optimization algorithm could yield a design tool that can generate a list of the most promising FOWT conceptual designs that serve as a foundation for subsequent detailed time domain investigations.

3.1.1 Time domain models for FOWTs

Several studies in the past have generated fully coupled time domain aero-hydro-servo simulation codes to predict the behavior of FOWTs. One of the first fully coupled time domain simulation codes, referred to as FAST in the literature, was developed by Jonkman and Buhl Jr [7]. Jonkman's study presented a model to predict the response of a floating wind turbine system in a stochastic wind and wave environment using a tension leg spar buoy platform and Morison's approximation to the fluid loading. Skaare et al [59] developed a computer tool for simulating the dynamic response of FOWTs exposed to wind, wave, and current forces. They used HAWC2 [8], which is a state-of-the-art aero-elastic code, for analysis of the wind turbine, and the SIMO/RIFLEX computer program for calculating the dynamic response of the marine structure. Jonkman [41] augmented FAST with the HydroDyn module, which calculates the hydrodynamic loads on the floating turbine support structure. Jonkman's FAST and HydroDyn combination is widely used for simulation of FOWTs in the literature [4, 16, 43, 51, 57, 60, 61].

In the study of Roddier et al [62], FAST was integrated with TimeFloat, a time domain floating body dynamics code, to conduct a techno-economic feasibility study for the WindFloat technology. Ormberg et al [63] used the AeroDyn module of the FAST, which is a well proven time domain simulation tool, as well as the SIMO/RIFLEX

for simulation of coupled floating structures in offshore wind turbine applications. Bossanyi [9] developed the GL Garrad Hassan software BLADED to calculate the aerodynamic and hydrodynamic loads of FOWTs in the time domain. Henderson et al [64] used BLADED to assess the prospects of suitable floating support structures for FOWTs in the North and Baltic seas. Myhr et al [65] conducted a numerical study of FOWTs using 3Dfloat and ANSYS [66] to compare FOWTs built on a spar buoy and a tension leg platform.

Larsen et al [67] presented a model to simulate loads and dynamics motions for a floating wave energy conversion which platform was also equipped with wind turbines. In Larsen's study, the aero-elastic code HAWC2 [8] was coupled to the time domain diffraction/radiation model for floating systems, WAMSIM [68]. Karimirad and Moan [69] addressed coupled wave and wind induced motions of a FOWT with a spar type platform in both extreme and operational environmental conditions using DeepC [70] and HAWC2. A 3D platform dynamics and wave loading code was implemented into Flex5 [71] by Ramachandran [72], resulting in a fully coupled aero-hydro-servo model for FOWTs. Bae and Kim [73] modified FAST to include additional features of the time domain mooring dynamic analysis program CHARM3D [70] to improve the fidelity of the moored floating platform dynamics model.

3.1.2 Simplified FOWT modeling techniques

In the context of developing a simpler FOWT modeling technique, there are two strategies in the literature: one is to remain in the time domain but eliminate some system degrees of freedom (DOF), and the second is to use a linearization of the system dynamics in order to facilitate frequency domain analysis.

Reduced order time domain models

Considering reduced order time domain models, Fulton et al [74] considered 6 DOF simulation of FOWTs using three codes: BLADED, FAST, and OrcaFlex. Casale

et al [75] conducted a preliminary design exercise for FOWTs considering eight DOF incorporating the wind turbine blade, tower, and the floating support structure. In Casale et al's study, the code MOSES [76] was used to assess the behavior of the floating system under wave and wind loads. Sandner et al [77] developed a simplified low order wind turbine model (SLOW) for the initial coupled structural analysis of the FOWT support structures. Zhang et al [78] studied the dynamic behavior of a FOWT considering the support structure (floating platform and tower) to be rigid, but did fully couple the dynamics of the wind turbine, support structure, and mooring lines. Zhang et al's study was performed in both the frequency and time domains using the SESAM software [79].

Frequency domain models

Alternative to the time domain simulation, the full system response has been assembled as a superposition of harmonic constituents. The frequency domain approach is widely used for floating offshore structures [10, 11, 60, 80, 81]. The prerequisite to the frequency domain approach is a linearization of the system dynamics. Usually, this linearization is accomplished using the time domain simulation codes themselves. FAST is the most widely used tool for FOWTs linearization in the literature; it has been used by Wayman [12], Wayman et al [13], Tracy [14], Hall [15], Karimi et al [16], Philippe et al [82], Saad et al [83].

One of the first frequency domain offshore wind turbine codes was TURBU developed by van Engelen and Braam [84]. However, TURBU has only been used to model fixed bottom offshore wind turbines with eleven structural and mechanical DOF for the wind turbine blades, and tower. Brommundt et al [31] used the WADAM and the spectrum of turbulent aerodynamic loads to study the mooring dynamics and responses of a FOWT. Kvittem and Moan [85] focused on developing a frequency domain methodology to calculate the tower base bending moment and fatigue damage of a semisubmersible floating wind turbine using WADAM and the complex trans-

fer functions of the platform displacements. Lupton [55] developed a new numerical method to model FOWTs using a frequency domain approach to find the overall response of the system to harmonic wind and wave loading. The accuracy of Lupton's method was verified by comparing the calculated platform displacements and wind turbine blade and tower loads of the OC3-Hywind [5] FOWT model to similar results produced using the time domain commercial code BLADED. Peak-peak errors of less than 5% were achieved in Lupton's study for harmonic wave and wind inputs. To date, no frequency domain model of FOWTs has included realistic turbulent wind and irregular wave conditions.

3.1.3 Proposed model

In the current study, a new frequency domain approach for a coupled wind turbine, floating platform, and mooring system is developed using the validated numerical tools FAST and WAMIT as sub-modules. While the linearization capability of FAST is utilized, this is only done to obtain a frequency domain sub-model for the rotor/tower aerodynamics and flexible structural response. A separate sub-model based on WAMIT is assembled for the hydrodynamics. The approach is therefore unique in preserving the important frequency-dependent nature of the wave excitation response of the system; this is lost with a more typically adopted full linearization of the coupled system wholely within FAST. Irregular wave and turbulent wind loads are incorporated using wave and wind power spectral densities (PSDs), JONSWAP and Kaimal, that are determined from the environmental conditions mentioned in Jonkman and Matha [52]. The FOWT system sub-models are coupled to yield a simple frequency domain model of the FOWT system with a flexible moored support structure. Although the model framework has the capability of incorporating tower and blade structural DOF, these components are considered as rigid bodies for further simplicity here. To verify the proposed framework, predicted wind turbine, floating platform and mooring system responses to the turbulent wind and irregular wave

loads are compared to model outputs from the full FAST time domain model. To identify a valid range of technology and environmental conditions for this approach, three classes of platforms including the OC3-Hywind [5], the MIT/NREL TLP [43], and the OC4-DeepCwind semisubmersible [6] are examined in this work. Using this simple fast and sufficiently accurate frequency domain approach, design optimization for a wide range of platform designs under a fully coupled floating system should be possible.

3.1.4 Chapter outline

The remainder of this chapter is presented as follows. The coupled frequency domain approach that includes the system's component sub-models, wind/wave PSDs, and governing frequency domain equations is discussed in Section 3.2. Section 3.3 presents the strategy for recovering time domain descriptions of system motions, internal forces and other dynamic variables from the frequency domain outputs. In particular, a fatigue load analysis is presented to demonstrate the new frequency domain model's utility for FOWT conceptual design and analysis. Section 3.4 compares the results of the 22 DOF and the 6 DOF time domain simulations, and then the results of the proposed 6 DOF frequency domain model are compared with the 22 DOF time domain model for each of the baseline FOWTs. Section 3.5 presents conclusions drawn from the current work and directions for the future work.

3.2 Frequency domain model framework

The frequency domain model presented here is implemented as a stand-alone code in MATLAB. For given wind and wave PSDs, the model calculates a series of constituent harmonics based on a schedule of frequency dependent system mass, damping, and stiffness matrices. In the following subsections, we describe how these linearized time domain model constituents are identified using existing FAST and WAMIT

functionality, the conversion into frequency domain, and how the final frequency domain model translates wind and wave PSDs into frequency domain outputs that are subsequently used to form time domain descriptions of key system metrics.

3.2.1 Wind turbine and platform description

In the modeling framework, Fig. 3.1, system displacement for a FOWT are described in a global coordinate system as $q_{6\times1} = [X\ Y\ Z\ \phi\ \theta\ \psi]^T$. These include surge X, sway Y, heave Z, roll ϕ, pitch θ, and yaw ψ. For simplicity, the wind turbine blades, nacelle and tower are assumed rigid with no structural DOF for the frequency domain model. Moreover, the rotor rotational speed is assumed constant at a rate $\dot{\gamma}$, and a collective blade pitch (rotor pitch) controller is defined to increase the platform restoring moments [86, 87]. The collective blade pitch controller changes rotor tilt angle, lowers the thrust load and lowers the tipping moment induced on the platform. This leads to an increase in the overall restoring moment- restoring moment here referring to the net moment causing the platform to return to a level state. A local coordinate system is aligned with the center of gravity of the platform and tower, and is placed on the wind turbine tower base [88]. This origin is the reference point for all the system kinematic variables and moment calculations in this work. Wind and wave directions are chosen to be aligned with the positive X axis direction of the global reference frame (X, Y, Z) as shown in Fig. 3.1. The Newton's second law with regard to the global frame for a FOWT can be written as:

$$\left[R\ M_t(\gamma)\ R^T\right]\ddot{q} = f(q,t,\alpha,\gamma) \tag{3.1}$$

where R is the transformation matrix to the global frame (c.f. Eq. 2.55, [89]), $M_t(\gamma)$ is the FOWT total mass matrix at reference point in terms of a local frame, and $f(q,t,\alpha,\gamma)$ is the state (q), time (t), rotor pitch angle (α), and blade azimuth angle (γ) dependent forcing vector.

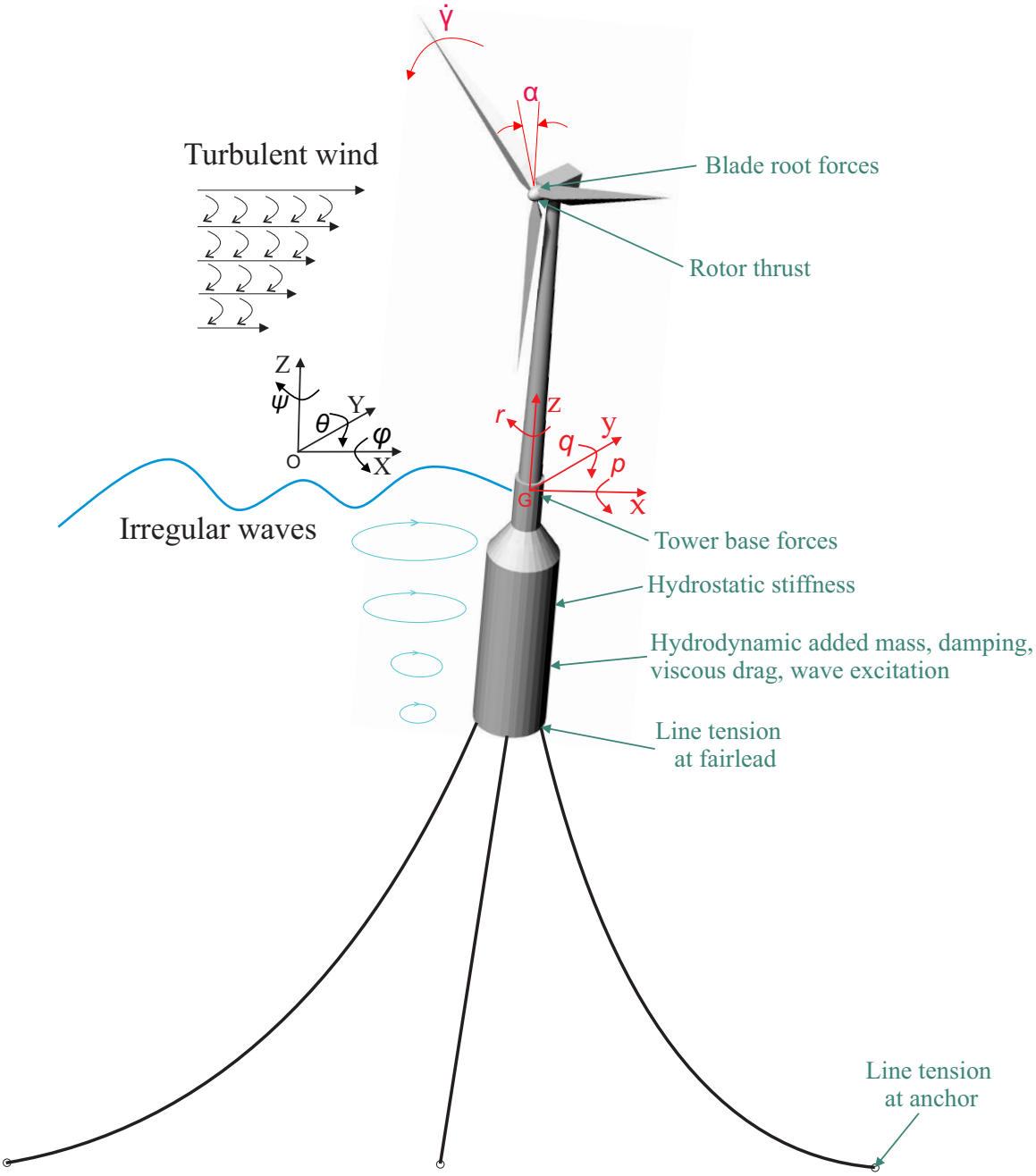

Figure 3.1: FOWT DOF, global reference frame (X, Y, Z, ϕ, θ, ψ), environmental factors and key output variables (i.e. internal loads) associated with the proposed FOWT frequency domain model. The conventional rigid body DOF are incorporated: surge x, sway y, heave z, rate of roll p, pitch q, yaw r. G is the center of gravity of the platform and tower, α is the collective blade pitch angle (rotor angle), and $\dot{\gamma}$ indicates rotor rotational speed.

3.2.2 Wave and wind inputs

In this chapter, irregular wave loads are considered through the adoption of JONSWAP wave spectra [90]. The wave amplitude of each frequency is characterized by the power associated with it, which is defined by the PSD function. The JONSWAP sea state spectrum, suggested by Jonkman et al [91], is defined as:

$$\begin{aligned} S_J(\omega) = \frac{1}{2\pi}\frac{5}{16} {H_s}^2 \; T_P\Big(\tfrac{\omega \; T_P}{2\pi}\Big)^{-5} exp\left[\tfrac{-5}{4}\left(\tfrac{\omega T_P}{2\pi}\right)^{-4}\right] \\ \times(1-0.287 \; ln(\Gamma)) \; \Gamma^{exp\left[-0.5 \; \left(\frac{\frac{\omega \; T_P}{2\pi}-1}{\sigma(\omega)}\right)^2\right]} \end{aligned} \tag{3.2}$$

where ω is the wave frequency, H_s is the significant wave height, T_P is the peak spectral period, Γ is the peak shape parameter of the JONSWAP sea state, and σ is the scaling factor. The IEC 61400-3 design standard recommends the following schedule for the peak shape parameter and scaling factor based on the significant wave height and peak spectral period [92].

$$\sigma(\omega) = \begin{cases} 0.07 & for \quad \omega \leq \frac{2\pi}{T_P} \\ 0.09 & for \quad \omega > \frac{2\pi}{T_P} \end{cases} \tag{3.3}$$

$$\Gamma = \begin{cases} 5 & for \quad \frac{T_P}{\sqrt{H_s}} \leq 3.6 \\ exp\left(5.75 - 1.15 \; \frac{T_P}{\sqrt{H_s}}\right) & for \quad 3.6 < \frac{T_P}{\sqrt{H_s}} \leq 5 \\ 1 & for \quad \frac{T_P}{\sqrt{H_s}} > 5 \end{cases} \tag{3.4}$$

The wind turbulence, also defined in the frequency domain by a user supplied PSD function, describes the spectral distribution of the variance of the wind speed [93]. In this study, the Kaimal spectrum [94, 95] is used following:

$$S_k(f) = \frac{4 \; \sigma_k^2 \frac{L_k}{\overline{U}_{hub}}}{\left(1 + \; \frac{6 \; f_i \; L_k}{2\pi \; \overline{U}_{hub}}\right)} \tag{3.5}$$

In Eq. 3.5, f_i is the cyclic frequency, and L_k is the integral length scale (c.f. Eq. 21, [95]), $\overline{U}_{hub}$ is the mean wind speed at the hub height, and σ_k is the standard

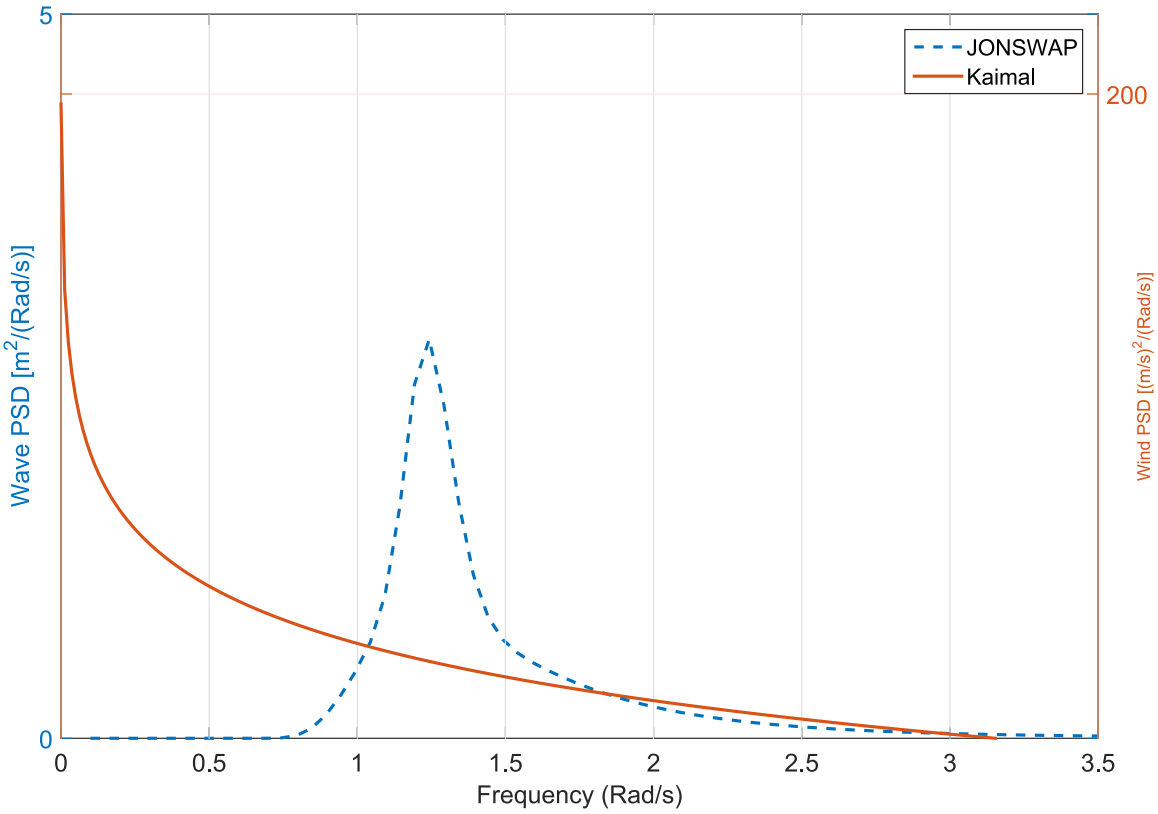

Figure 3.2: Wind (Kaimal), and wave (JONSWAP) power spectral densities over a frequency band at the rated wind speed (12 m/s) and corresponding wave height (3.4 m) and peak period (5.1 s).

deviation of wind speed which is calculated using turbulence intensity and $\overline{U}_{hub}$. The turbulence intensity is generally lower offshore than onshore [93]. Figure 3.2 shows the wind and wave spectra for an operating environmental condition described further in section 3.4.1.

3.2.3 Linearizing FOWT dynamics using FAST

The complete system dynamics of each FOWT design are assembled from three main components: the platform, the wind turbine and the mooring system (see Fig. 3.1). To numerically linearize the non-linear equation of motion (Eq. 3.1), a two step linearization process is followed: first, a steady state operating point for all DOF is achieved; then, a numerical linearization is performed by perturbing each of the

system variables about their operating point (op), calculating the induced changes in the individual aerodynamic, hydrodynamic and mooring forces and thereby form the periodic state matrices using finite differences [7]. FAST is used in this study to complete this process considering still water and steady wind.

Calculating the steady state operating point

To calculate the steady state operating point, all the 6 DOF of floating platform as well as the rotor pitch angle in a steady wind and still water (no wave) are considered. The hydrodynamic approximations including the added mass, damping, and hydrostatic matrices are generated using WAMIT for all the selected platforms. Note that only diagonal values of the added mass and damping matrices at the infinite wave frequency are used in this step (see section 3.2.4). The main reasons for this assumption are: to allow the time domain model to evolve until the system achieves its stable operating point, and to subtract the constant added mass and damping from M_{avg} and C_{avg} in assembling the frequency domain model (see section 3.2.4).

In the steady state operating point, the general equation of motion for a FOWT can be written as:

$$\Big(M_p + M_w(\gamma)\Big)\,\ddot{q}_{op} = f_{op}(q_{op}, t, \alpha, \gamma) \tag{3.6}$$

where M_p is the platform mass, $M_w(\gamma)$ is the wind turbine/tower mass, and $f_{op}(q_{op}, t, \alpha, \gamma)$ is the steady state forcing function vector at the operating point.

Finite difference approximations to the system state matrices

The total loads acting on the platform are hydrostatic load F_h, viscous drag load F_{vd}, radiation load F_{rad}, mooring line loads F_m, and loads transmitted on the wind turbine F_{aero}. Therefore, the forcing function vector is defined as:

$$f(q, \alpha, \gamma) = F_h + F_{vd} + F_{rad} + F_m + F_{aero} \tag{3.7}$$

FAST numerically linearizes the equation of motion by perturbing (represented by Δ) the system state and control variables about the operating point (op) values:

$$q = q_{op} + \Delta q \quad ; \quad \dot{q} = \dot{q}_{op} + \Delta \dot{q} \quad ; \quad \ddot{q} = \ddot{q}_{op} + \Delta \ddot{q} \tag{3.8}$$

$$\begin{aligned} \Delta f(q, \alpha, \gamma) = & \frac{\partial F_h}{\partial q}|_{op} \Delta q + \frac{\partial F_{vd}}{\partial \dot{q}}|_{op} \Delta \dot{q} + \frac{\partial F_{rad}}{\partial \dot{q}}|_{op} \Delta \dot{q} + \frac{\partial F_{rad}}{\partial \ddot{q}}|_{op} \Delta \ddot{q} \\ & + \frac{\partial F_m}{\partial q}|_{op} \Delta q + \frac{\partial F_{aero}}{\partial u_d}|_{op} \Delta u_d + \frac{\partial F_{aero}}{\partial \dot{q}}|_{op} \Delta \dot{q} + \frac{\partial F_{aero}}{\partial q}|_{op} \Delta q \end{aligned} \tag{3.9}$$

$$\left(\left[M_p + M_w(\gamma) \right] + \Delta \left[M_p + M_w(\gamma) \right] \right) \Delta \ddot{q} = f_{op} + \Delta f(q, \alpha, \gamma) \tag{3.10}$$

In Eq. 3.10, Δu_d is the vector of wind input disturbances. The state dependence of the mass matrices is bundled into an inertial force which is defined as:

$$\begin{aligned} \Delta F_I = & - \left(\Delta \left[M_p + M_w(\gamma) \right] \Delta \ddot{q} \right) = \\ & - \left(\Delta f(q, \alpha, \gamma) - \left[M_p + M_w(\gamma) \right] \Delta \ddot{q} \right) \end{aligned} \tag{3.11}$$

The perturbation of the inertial force is:

$$\Delta F_I = \frac{\partial F_I}{\partial q}|_{op} \Delta q + \frac{\partial F_I}{\partial u}|_{op} \Delta u \tag{3.12}$$

where Δu is the vector of rotor pitch control inputs.

By substituting the perturbations into the equation of motion and expanding as a Taylor series approximation, the linearized second order representation of the motion equations can be written as:

$$
\begin{aligned}
&\underbrace{\left(\underbrace{(M_w(\gamma)|_{op}+M_p|_{op})}_{(1)}+\underbrace{\frac{\partial F_{rad}}{\partial \ddot{q}}|_{op}}_{(2)}\right)}_{M_{avg}}\Delta\ddot{q}\\
&+\underbrace{\left(\underbrace{\frac{\partial F_{aero}}{\partial \dot{q}}|_{op}}_{(3)}+\underbrace{\frac{\partial F_{rad}}{\partial \dot{q}}|_{op}}_{(4)}+\underbrace{\frac{\partial F_{vd}}{\partial \dot{q}}|_{op}}_{(5)}\right)}_{C_{avg}}\Delta\dot{q}\\
&+\underbrace{\left(\underbrace{(\frac{\partial F_{aero}}{\partial q}+\frac{\partial F_I}{\partial q})|_{op}}_{(6)}+\underbrace{\frac{\partial F_h}{\partial q}|_{op}}_{(7)}+\underbrace{\frac{\partial F_m}{\partial q}|_{op}}_{(8)}\right)}_{K_{avg}}\Delta q\\
&=\underbrace{-\frac{\partial F_{aero}}{\partial u_d}|_{op}}_{(9)}\Delta u_d-\underbrace{\frac{\partial F_I}{\partial u}|_{op}}_{(10)}\Delta u
\end{aligned}
\tag{3.13}
$$

In Eq. 3.13, term (1) is the mass matrix of the system at the operating point, term (2) is the constant added mass matrix (diagonal values of the added mass matrix at the infinite frequency), term (3) is the aerodynamic damping, term (4) is the wave damping (similar to the added mass, only diagonal values of the damping matrix at the infinite frequency are used in this step), term (5) is the viscous drag damping, term (6) is the added aerodynamic stiffness which includes gyroscopic stiffness, term (7) is the hydrostatic stiffness, term (8) is the mooring stiffness, term (9) is the wind input disturbance matrix, and term (10) is the rotor pitch control input matrix. In the above equation, M_{avg}, C_{avg}, and K_{avg} are the total azimuth-averaged (see the next section) of the total mass, damping, and stiffness matrices at the steady state operating point.

3.2.4 Assembling the frequency domain model

The frequency domain output files need a multi-blade coordinate (MBC) transformation [96] which behaves as a filter between the rotating subsystem (rotor) and the

nonrotating entities (tower, nacelle, and platform). A MBC transforms the azimuth-specific mass, damping, stiffness, output variable, displacement output matrix, velocity output matrix, pitch control input transmission matrix, and wind input disturbance transmission matrix to a nonrotating frame to be used in the frequency domain model. Note that 36 equally-spaced azimuth steps is defined in the periodic linearized model.

To evaluate the dynamics of a candidate FOWT in the frequency domain, the total loads on the system including platform, mooring, and wind turbine loads are gathered into 6x6 system mass, stiffness, damping and wind/wave excitation load matrices. The resulting frequency domain equation of motion for an irregular wave and unsteady wind is shown in Eq. 3.14:

$$\begin{aligned} &-\omega^2\left(\underbrace{(M_{avg}-\frac{\partial F_{rad}}{\partial \ddot{q}}|_{op})}_{(1)}+\underbrace{M_a(\omega)}_{(2)}\right)\Delta Q(\omega)e^{i\omega t} \\ +i\omega&\left(\underbrace{(C_{avg}-\frac{\partial F_{rad}}{\partial \dot{q}}|_{op})}_{(3)}+\underbrace{C_p(\omega)}_{(4)}\right)\Delta Q(\omega)e^{i\omega t}+\underbrace{\left(K_{avg}\right)}_{(5)}\Delta Q(\omega)e^{i\omega t} \\ =&\left(\underbrace{F_w\left(\sqrt{2\ S_J(\omega)\Delta\omega}\right)}_{(6)}+\underbrace{F_d\left(\sqrt{2\ S_k(\omega)\Delta\omega}\right)}_{(7)}+\underbrace{F\Delta U(\omega)}_{(8)}\right)e^{i\omega t} \end{aligned} \tag{3.14}$$

where $\Delta Q(\omega)e^{i\omega t} = \Delta q$ and $\Delta U(\omega)e^{i\omega t} = \Delta u$, term (1) is the system mass after subtracting the diagonal high frequency WAMIT added mass values (term (2) in Eq. 3.13) from M_{avg}, term (2) is the platform added mass matrix calculated using WAMIT, term (3) is the system damping matrix after subtracting the diagonal high frequency WAMIT damping values (term (4) in Eq. 3.13) from C_{avg}, term (4) is the platform dependent damping matrix calculated using WAMIT, term (5) is the system stiffness matrix, term (6) is the forcing amplitude of the wave excitation vector F_ω calculated using WAMIT and JONSWAP spectrum $S_J(\omega)$, term (7) is the forcing

amplitude of the wind disturbance vector calculated using wind input disturbance matrix F_d (term (9) in Eq. 3.13) and Kaimal spectrum $S_k(\omega)$ at the hub height, term (8) is the forcing amplitude of the rotor pitch control vector calculated using the rotor pitch control input matrix F (term (10) in Eq. 3.13) and the rotor pitch control vector $U(\omega)$, and ω is the frequency of the steady system response. Note that for calculation of $U(\omega)$, a single control input spectrum is calculated based on a Fourier transform of a time series of the collective blade pitch control produced during a single time series simulation for each platform type.

Note that terms (6)-(8) are independent for each frequency component, ω. To reconstitute a time domain response through superposition of the responses at the individual frequencies, we realize that a common control action must be applied across the instances of Eq. 3.14. In addition, the relative phases of the external forces in terms (6)-(8) are assumed to be zero, since detail of phases cannot be extracted from PSDs as shown in Fig. 3.2. An example of wave excitation, wind disturbance, and the collective blade pitch forcing amplitudes (terms (6)-(8) in Eq. 3.14) are shown in Fig. 3.3 for an operating environmental condition described further in section 3.4.1. The force contribution plots show the design importance of the collective blade pitch controller along with the structures as an integrated system to decrease the tipping moment induced on the platform as discussed in section 3.2.1. Note that the collective blade pitch controller is only used for the rated and above rated wind speeds- region 3 of the wind turbine power curve [87].

Making use of Eq. 3.14, the complex form of the equation of motion to evaluate the complex response of the FOWT to the wind and wave excitation forces at a single frequency bin can be summarized as:

$$\left(-\omega^2 M_t(\omega) + i\omega C_t(\omega) + K_t\right) \Delta Q(\omega) = F_t(\omega) \tag{3.15}$$

where $M_t(\omega)$ is the total 6x6 mass matrix (terms (1) and (2) in Eq. 3.14), $C_t(\omega)$ is the total 6x6 damping matrix (terms (3) and (4) in Eq. 3.14), $K_t(\omega)$ is the total 6x6

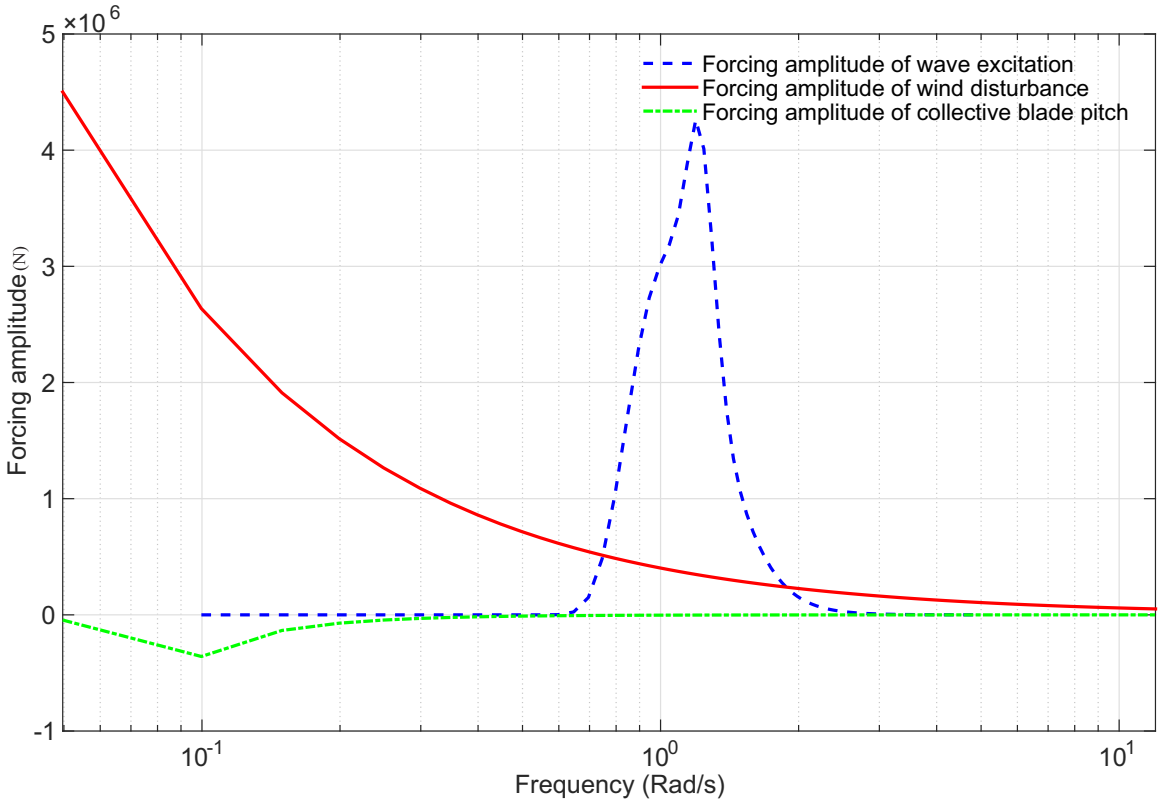

Figure 3.3: An example of wave excitation, wind disturbance, and collective blade pitch forcing amplitudes over a frequency band at the rated wind speed (12 m/s) and corresponding wave height (3.4 m) and peak period (5.1 s) for the OC3-Hywind spar buoy platform.

stiffness matrix (term (5) in Eq. 3.14), and F_t is the total 6x1 excitation load matrix (terms (6)-(8) in Eq. 3.14).

Frequency domain output variables

Along with the frequency domain equation of motion (Eq. 3.15), the FAST capability to process a set of series of output variables is used in this study. The second-order frequency domain representation of the output system in the complex form and the amplitude of output variables are given as:

$$\begin{bmatrix} \Delta Y_1(\omega) \\ \Delta Roll(\omega) \\ \vdots \\ \Delta Y_j(\omega) \end{bmatrix} = \begin{bmatrix} i\omega VelC_{1\times k}\ \Delta Q_{k\times 1}(\omega) \\ i\omega VelC_{Roll}\ \Delta Q_{Roll}(\omega) \\ \vdots \\ i\omega VelC_{j\times k}\ \Delta Q_{k\times j}(\omega) \end{bmatrix} + \begin{bmatrix} DspC_{1\times k}\ \Delta Q_{k\times 1}(\omega) \\ DspC_{Roll}\ \Delta Q_{Roll}(\omega) \\ \vdots \\ DspC_{j\times k}\ \Delta Q_{k\times j}(\omega) \end{bmatrix} + \begin{bmatrix} D_{d1}\Delta U_d(\omega) \\ D_{dRoll}\Delta U_d(\omega) \\ \vdots \\ D_{dj}\Delta U_d(\omega) \end{bmatrix} + \begin{bmatrix} D_1\Delta U(\omega) \\ D_{Roll}\Delta U(\omega) \\ \vdots \\ D_j\Delta U(\omega) \end{bmatrix} \tag{3.16}$$

$$\begin{bmatrix} Y_1(\omega) \\ Roll(\omega) \\ \vdots \\ Y_j(\omega) \end{bmatrix} = \left| \begin{bmatrix} \Delta Y_1(\omega) \\ \Delta Y_{Roll}(\omega) \\ \vdots \\ \Delta Y_j(\omega) \end{bmatrix} \right| + \begin{bmatrix} Y_{op_1}(\omega) \\ Y_{op_{Roll}}(\omega) \\ \vdots \\ Y_{op_j}(\omega) \end{bmatrix} \tag{3.17}$$

where j subscript shows the number of output variables and k subscript presents the system's DOF, $VelC$ is the azimuth-averaged velocity output matrix which represents velocity to output direct connections, $DspC$ is the displacement output matrix which shows the displacements to output direct connections, D_d and D are the wind input disturbance and control input transmission matrices which represent the input-to-output direct connections, Y_{op} is the output variable vector at the steady state operating point, and $Roll(\omega)$ is the amplitude of the platform roll motion. All the aforementioned matrices are calculated using FAST and the MBC at the steady state operating point (more details are available in the FAST and MBC user's guides [96]). As Eqs. 3.16 and 3.17 present, the amplitude of the output variables, Y, is computed using the state variable Q in a given simulation (see Eq. 3.15). The architecture of this frequency domain aero-hydro-elastic model as well as the governing equations are presented in Fig. 3.4.

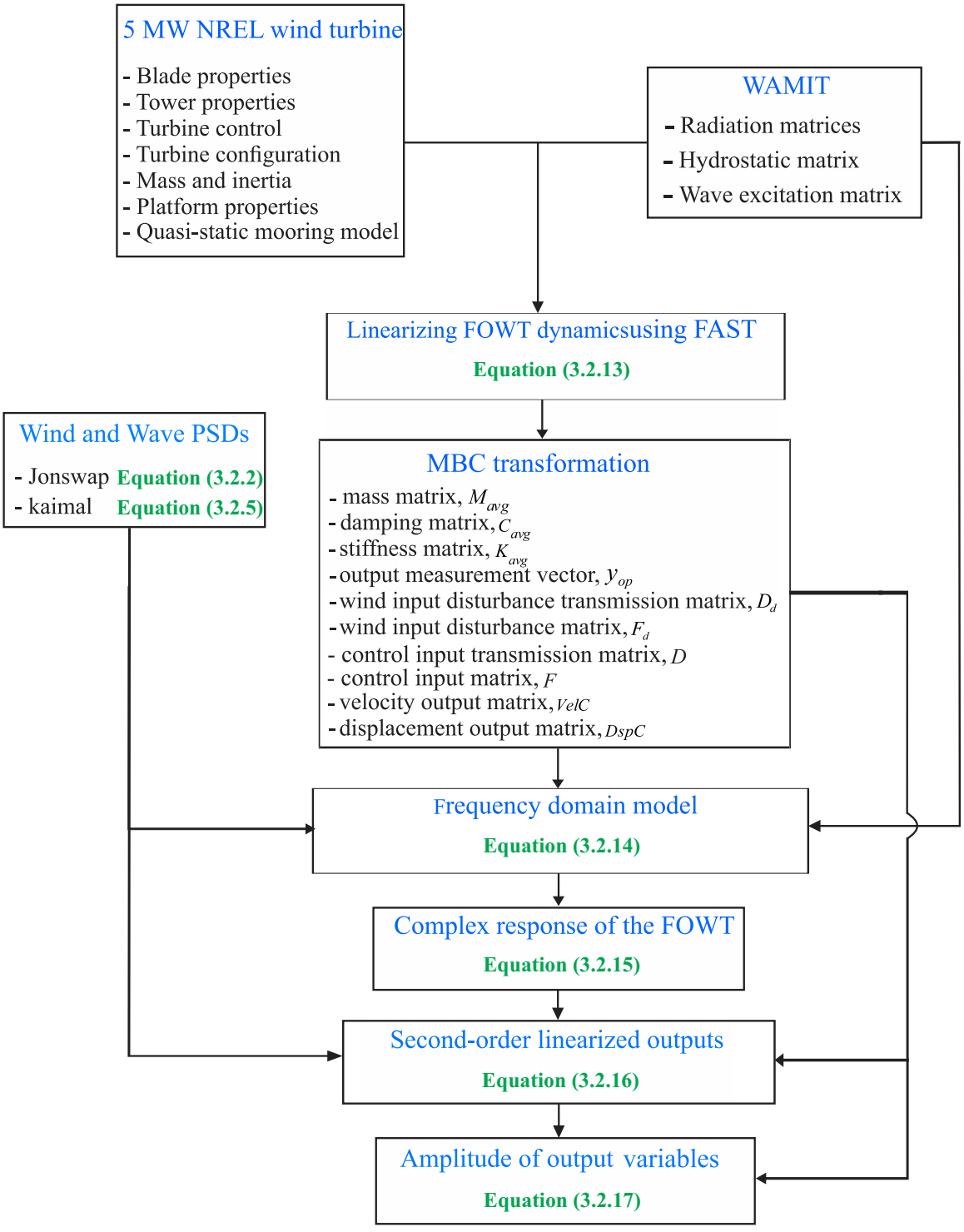

Figure 3.4: The fully coupled frequency domain model architecture including wind turbine and platform properties, linearization framework, assembling the frequency domain model, and frequency domain output variables

3.3 Fatigue load analysis

In order to perform an extreme load analysis and fatigue-life prediction in this study, the output variables are converted from the frequency domain model to the time domain data file using the following equation:

$$\zeta(t) = \sum (Y_i \cos(\omega_i t + \phi_i)) \tag{3.18}$$

where $\zeta(t)$ is the time series of output variables, and Y is the frequency domain amplitude of the output variables (see Eqs. 3.16 and 3.17), t is time in seconds, and ω_i and ϕ_i are the associated frequency and random phase angles respectively. Note that Eq. 3.18 uses multiple ϕ to reflect random phasing and capture a good set of potential interactions of frequency components. The lifetime fatigue analysis is performed based on the complete design lifetime of the FOWT components by including wind speed distribution, cycle counting of the variable-amplitude load ranges, ultimate loads, and fixed mean loads as discussed in Hayman and Buhl Jr [97]. The ultimate (extreme) loads obtained from largest loads across the time series of output variables $\zeta(t)$. In order to calculate the equivalent lifetime constant-amplitude fatigue-load, also referred to as the accumulative damage equivalent load (DEL) in the literature, a collection of time-series data is require [98]. In this case, the accumulation of the total damage from all cycles is then computed as an equivalent DEL for a given single frequency of loading:

$$DEL_j^{Life} = \sum_i \frac{n_{ji}^{Life}}{N_{ji}} \tag{3.19}$$

$$DEL^{Life} = \sum_j DEL_j^{Life} \tag{3.20}$$

where DEL_j^{Life} is the damage over the design lifetime from the j^{th} time series, n_{ji} is the life cylces, and N_{ji} is the cycles to failure which is shown in Eq. 3.21:

$$N_{ji} = \left(\frac{L_{ult} - L_{FM}}{\frac{1}{2} L_{ji}^{RF}} \right)^m \tag{3.21}$$

where L_{ult} is the ultimate design load, L_{FM} is the fixed mean load, L_{ji}^{RF} is the range about the mean load in the simulation, and m is the Wholer exponent which is specific for each output variable [98]. Note that fatigue loads are calculated using Mlife [97] in this study. Hence, the reader is referred to the Mlife user's guide and Mlife theory manual for more details about the fatigue analysis using Mlife.

3.4 Results

To this stage, a framework for numerical linearization of the non-linear equations of FOWT motion has been proposed; the frequency domain motion equations were used to establish a frequency domain model that consolidated turbulent wind and irregular wave loads. By aggregating the frequency domain model outputs over the complete range of wind/wave inputs, time series responses for motions and internal loads can be synthesized and used to assess the performance of candidate FOWT designs.

To check the validity of the frequency domain model, results for three FOWT design candidates are compared to FAST time domain simulations. For each FOWT, the three-bladed NREL offshore 5 MW horizontal axis wind turbine is used as a reference model. Properties of this offshore wind turbine are given in Table 3.1. More details about the blade and tower structure, control system, mass and inertia properties can be found in Jonkman et al [40].

Three floating support structures, which have been widely studied previously, are chosen as the baseline models: a mooring-stabilized platform, also called the MIT/NREL TLP, a ballast-stabilized platform, also known as the OC3-Hywind spar buoy platform in the literature, and a buoyancy-stabilized platform, known as the

Table 3.1: Summary of the NREL offshore 5MW wind turbine properties [40]

Property	**Value**
Rated power	5 MW
Rotor diameter	126 m
Hub height	90 m
Cut-in wind speed	3 m/s
Rated wind speed	11.4 m/s
Cut-out wind speed	25 m/s
Rotor mass	110 000 kg
Nacelle mass	240 000 kg
Tower mass	347 460 kg
Center of mass height	64 m

Table 3.2: Summary of the MIT/NREL TLP, the OC3-Hywind spar buoy, and the OC4-DeepCwind semisubmersible properties

Property	**MIT/NREL TLP**	**OC3-Hywind spar buoy**	**OC4-DeepCwind semi-sub**
Draft	47.89 m	120 m	20 m
Total mass	8,600,000 Kg	7,466,000 Kg	13,473,000 Kg
Displacement	12,180 m^3	8,029 m^3	13,917 m^3
Diameter of the main column	18 m	6.5 m	6.5 m
Diameter of offset columns	N/A	N/A	12 m
Water depth	200 m	300 m	200 m
Number of mooring lines	8	3	3
Fairlead depth	47.89 m	70 m	20 m
Fairlead radius from centerline	27 m	5.2 m	40.87 m
Anchor radius from centerline	27 m	853.87 m	418 m
Mooring line unstretched length	151.7 m	902.2 m	440.35 m
Mooring line diameter	0.127 m	0.09 m	0.076 m
Mooring line linear density	116 kg/m	77.7 kg/m	113.35 kg/m
Mooring line EA	1,500,000 kN	384,243 kN	753,600 kN

OC4-DeepCwind semisubmersible. The TLP uses taut vertical mooring lines to keep the highly buoyant platform stable, however the spar buoy platform uses a heavy ballast mass and a deep draft to bring the platform's center of mass well below the center of buoyancy of the floating structure. The semisubmersible platform uses a large water plane area to raise the metacenter of the platform above the center of mass. Table 3.2 summarizes the properties of each platform and mooring system configuration. The details of these three concepts as well as the mooring line properties for each platform are explained in Robertson and Jonkman [4].

To quantify the impact of system DOF reduction on a number of structural metrics (maximum rotor thrust, total blade root and tower base bending moments, and fairlead tensions) a 22 DOF FAST time domain model (6 DOF platform, blade, tower, and generator with variable rotor rotational speed and active pitch controller) and a 6 DOF FAST time domain model (6 DOF platform with active pitch controller, and constant rotor rotational speed) are compared first for all three baseline platforms. In the next step, results drawn from the 6 DOF frequency domain model and the 6 DOF and 22 DOF FAST time domain models are compared for eight variables: the surge (PtfmSurge), roll (PtfmRoll), and pitch (PtfmPitch) motions and the rotor thrust, the total blade root bending moment (RootMxyt), the total tower base bending moment (TwBsMxyt), the fairlead tension (FairTen) and anchor tension (AnchTen). Note that total bending moment refers to the result of in-plane and out-of-plane bending moments on blade roots and tower base. In addition, Mlife is used to compare the statistical descriptions (e.g. the maximum and standard deviation) of each quantity, and the lifetime fatigue loads predicted using the 6 DOF and 22 DOF FAST time domain outputs and the time domain results created using the new frequency domain approach. The environmental conditions used in the comparison studies as well as the results from each model are discussed in the following sections.

3.4.1 Environmental and simulation conditions

In this study, the OC3-Hywind spar buoy platform, the MIT/NREL TLP, and the OC4-DeepCwind semisubmersible platform are simulated in water depths of 300 m, 200 m, and 200 m, respectively (see the design properties of these platforms in Table 3.2). A range of steady wind speeds from 4 m/s to 24 m/s with 2 m/s increments at the hub height are considered in the linearization of the system dynamics. An unsteady wind spectrum, Kaimal, and an irregular sea state spectrum, JONSWAP, are included in both the time and frequency domain models (see section 3.2.4). The JONSWAP spectrum are set using significant wave heights H_s that correspond to

the steady wind speed. The peak periods T_p for the range of wind speeds and wave heights are presented in Table 3.3 [52]. The peak shape parameter Γ of 3.3 is applied for all of the JONSWAP wave spectrum. For the Kaimal wind spectra, the integral length scale L_k was set as 28.35, and the standard deviation of wind speed σ_k of 1.2 m/s was considered [93]. The spectral discretization of the wave and wind was at a resolution of 0.0497 rad/s over the range of $0.001 \leq \omega \leq 12.65$ rad/s. For the sake of evaluating the frequency domain model, the output variables are calculated from an aggregate of all the environmental conditions.

For the FAST time domain simulations, a total run time of 25 minutes with integration time step of 0.0125 s is used. The turbulent wind data for the time domain model is generated using Turbsim [95] and irregular wave profile and loads is generated by the HydroDyn FAST module. In this study, the 6 DOF models work with 1D turbulent wind data and unidirectional waves, while the 22 DOF model uses 3D wind data. To avoid start-up transients, the first 5 minutes of data is excluded from the analysis. For plotting the output results of the 6 DOF FAST time domain and the 6 DOF frequency domain models, the reported amplitude results are the average of short-time Fourier transforms of the input signals which are divided into 512 segments (windows) using the MATLAB spectrogram function.

For the calculation of fatigue loads, the operating turbine design load case (DLC) 1.2 is considered in this study as recommended by the IEC 61400-3 design standard. Note that the other four fatigue DLCs including DLC 2.4 (control or protection system fault), DLC 3.1 (start-up), DLC 4.1 (shut-down), and DLC 6.4 (parked, idling) are also recommended by IEC 61400-3 for the fatigue life analysis of FOWTs. The wind speed range and the corresponding wave heights and peak periods for partially developed waves are shown in Table 3.3.

Table 3.3: Environmental conditions over the operational wind speed range for partially developed waves are shown for DLC 1.2 [60]

Objective Parameters	**Environmental Conditions**										
Mean Wind Speed (m/s)	4	6	8	10	12	14	16	18	20	22	24
Wave Height (m)	1.1	1.9	2.5	2.9	3.4	4	4.9	5.1	5.5	6.2	6.9
Peak Period (s)	2.9	3.2	3.9	4.3	5.1	5.9	6.4	7.2	8.7	9.1	9.7

3.4.2 System DOF reduction

To investigate the impacts of time domain modelling with 6 DOF versus a full time domain model, a new configuration of the FAST 22 DOF is used to compare the key parameters of the wind turbine and baseline platforms. Note that this comparison is an essential sequence from a 22 DOF time domain model to a 6 DOF time domain model, and then to a frequency domain 6 DOF model.

Figure 3.5 shows the comparison of the maximum rotor thrust, total blade root and tower base bending moments using an aggregate of time series results of the FAST 6 DOF and FAST 22 DOF time domain models for the baseline platforms. The comparison of these two models for the OC3-Hywind platform shows small variations of less than 1.4% for the maximum thrust load and tower base bending moment, and relatively larger variation of 9% for the maximum value of the blade root bending moment. The calculated maximum blade root bending moment for the MIT/NREL TLP shows 6% difference between the 22 DOF and 6 DOF time domain models. There is less than 5.2% variations in their maximum thrust load and tower base bending moment. Figure 3.5 shows the results for the maximum thrust load and tower base bending moment (variation of less than 2.1%) for the OC4-DeepCwind semisubmersible. Also for the OC4-DeepCwind semisubmersible, a variation of 11.6% in the maximum blade root bending moment was observed.

Figure 3.6 shows the comparison of the maximum fairlead tensions observed across an aggregate of time series over the full operational range for the time domain models and all three of the FOWT platforms. Based on Fig. 3.6, the difference between the

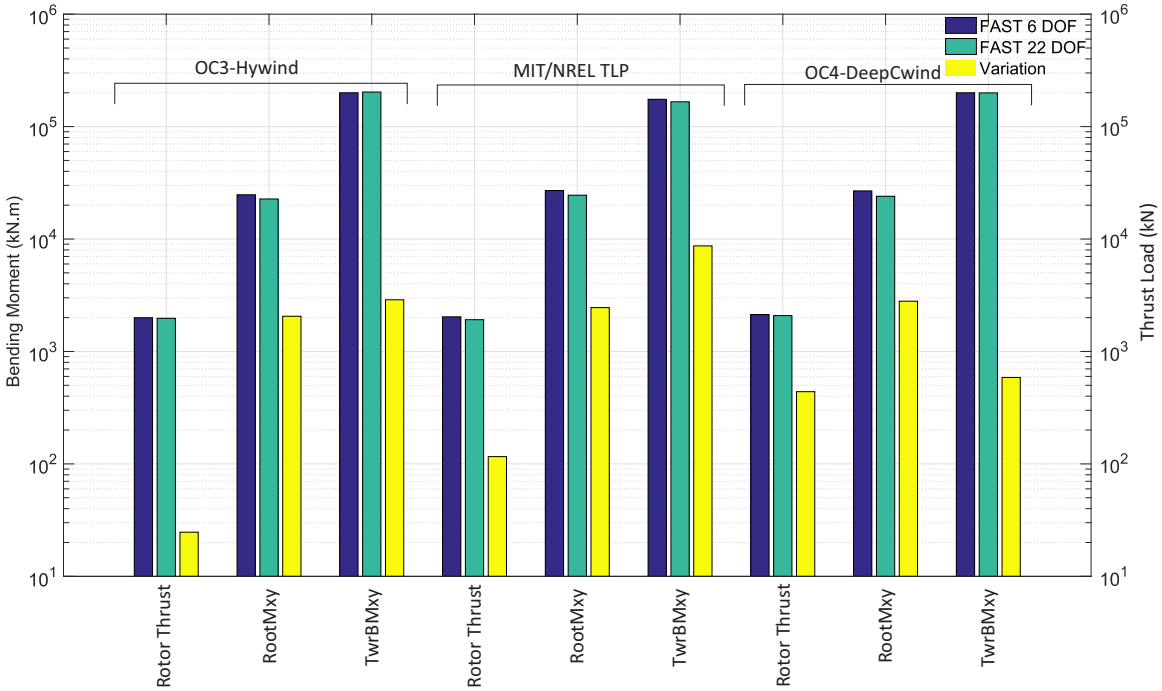

Figure 3.5: Comparison of the FAST 6 DOF and 22 DOF simulations for the maximum rotor thrust, total blade root bending moment, and total tower base bending moment using an aggregate of all the environmental conditions

maximum fairlead tensions for the OC3-Hywind platform and the MIT/NREL TLP are less than 9.9% and 4.6%, respectively. For the OC4-DeepCwind, the variation of maximum tensions in fairlead 1 and 2 are 5.2% and 2.3%, respectively. However the maximum tension of fairlead 3 for the 6 DOF time domain model is 43.2% greater than the 22 DOF time domain model. In any case, in the results presented in the next section, the comparison of the 6 DOF frequency domain and time domain models means that the 6 DOF time domain model is consistent with more flexible designs and conservative in its prediction (i.e., likely overpredicted results). Detailed comparison of the 6 DOF frequency domain model and time domain models for selected cases are presented in the following sections, highlighting the key results found in each verification.

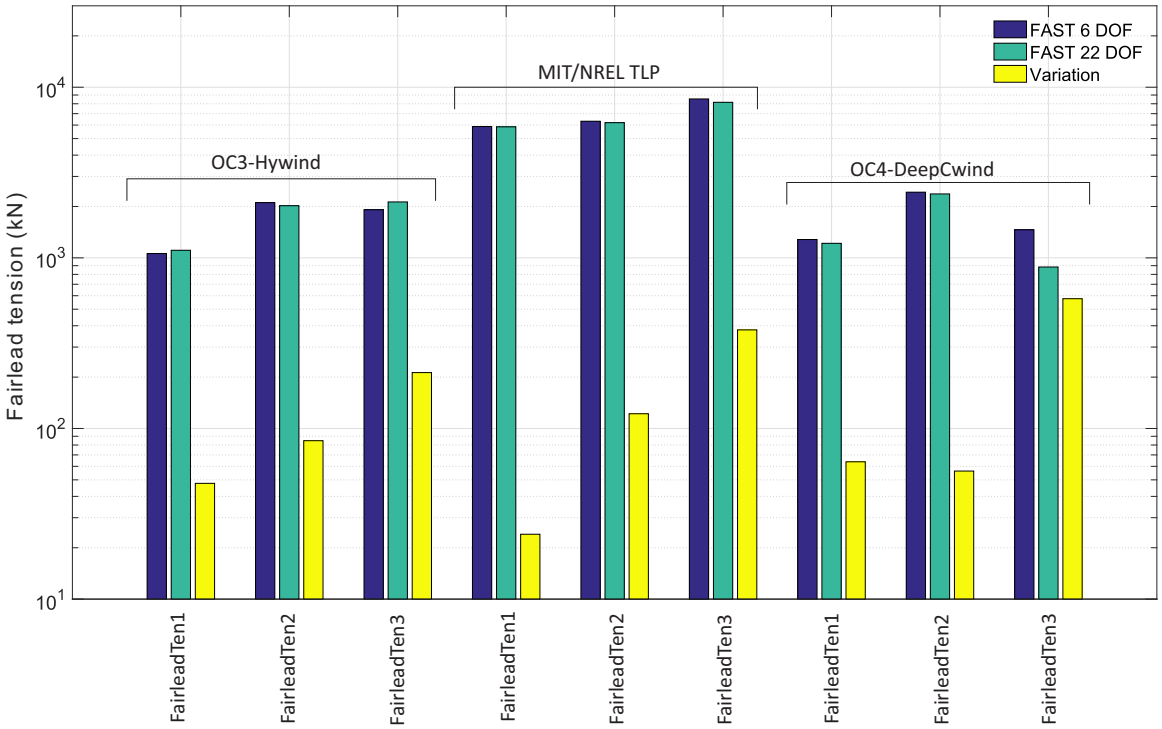

Figure 3.6: Comparison of the FAST 6 DOF and 22 DOF simulations for the maximum fairlead tension 1, 2, and 3 using an aggregate of all the environmental conditions

3.4.3 OC3-Hywind spar buoy case study

Overall views of the 6 DOF time domain and frequency domain results for the OC3-Hywind spar buoy platform at the wind turbine operating condition (wind speed of 12 m/s) are given in Fig. 3.7 and Fig. 3.8. Figure 3.7 shows the amplitude of platform responses in surge, roll, and pitch motions as well as the rotor thrust, total blade root bending moment, and tower base bending moment over the frequency range of $0.001 \leq \omega \leq 2.5\ rad/s$. One of the main reasons for the differences in the amplitude of output variables in Fig. 3.7 and Fig. 3.8 is the average of short-time Fourier transforms of the time domain signals which are divided into 512 segments (windows). To compare the statistical results of the frequency domain and time domain models, the maximum value, the standard deviation, and the variation of these metrics for all the output variables in time domain are summarized in Table 3.4 and Table 3.5 considering an aggregate of all the environmental conditions.

As can be seen from Table 3.4, the surge and roll motions show relatively small variations of 8.5% and 6.2% in their maximum values, respectively. However, the comparison of their standard deviations shows larger relative variations of 15.3% and 14.2%. Figure 3.7 indicates that for the roll motion, the difference between the linear and non-linear responses increases around the frequency of 0.14 rad/sec which shows a uniform underprediction of the linear roll motion at lower frequency. The results also give the variations of 11.7% and 11.5% for the maximum platform pitch angle and the standard deviation, respectively. The reason for the relatively large variation of the pitch motion is the underprediction of the aerodynamic thrust load in the frequency domain model which varies the platform rotational motions. The variations of 12.8% and 11.7% are observed for the maximum and the standard deviation of the aerodynamic thrust load which can consequently lead to changes in the platform pitch motion.

The total blade root bending moment and the tower base bending moment variations are also presented in Table 3.4. Based on this table, the difference between the maximum blade root bending moment for both the frequency domain and the time domain models is 9.2% with 13% variation in their standard deviations. The maximum value of the tower base bending moment and the variation of standard deviation for the frequency domain model are 11.5% and 10.1% less than the time domain model.

Table 3.4: Comparison of the frequency domain model and the time domain FAST results for the OC3-Hywind spar buoy platform. Maximum and standard deviation of the platform motions, total blade root and tower base bending moments for both models compared in time domain using an aggregate of all the environmental conditions

Objective Parameters	**Maximum**			**Standard Deviation**		
	6 DOF Frequency domain model	**6 DOF Time domain FAST**	**Variation (%)**	**6 DOF Frequency domain model**	**6 DOF Time domain FAST**	**Variation (%)**
PtfmSurge (m)	55.5	60.7	8.5	12.1	14.3	15.3
PtfmRoll (deg)	1.5	1.6	6.2	0.3	0.35	14.2
PtfmPitch (deg)	9.8	11.1	11.7	2.3	2.6	11.5
Rotor Thrust (kN)	1,550	1,777.7	12.8	384.9	436.2	11.7
RootMxyt (kN.m)	19,618	22,075	10.9	4,896	5,444.3	10
TwMsFxyt (kN.m)	164,280	190,070	13.5	38,380	44,265	13.2

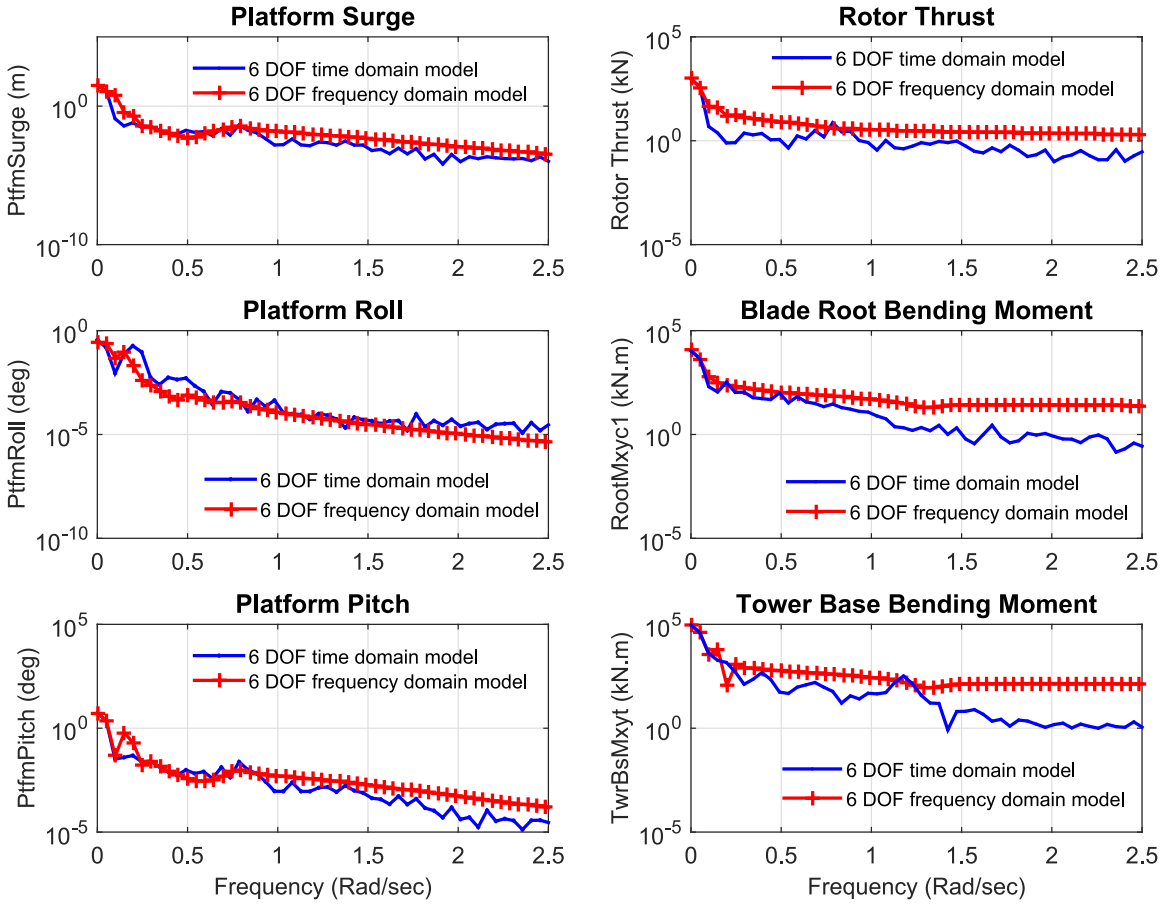

Figure 3.7: Results including amplitude of platform surge, roll, and pitch motions of the OC3-Hywind spar buoy platform at the wind turbine operating condition (wind speed of 12 m/s) are presented at the left side of the figure. The amplitude of rotor thrust, total blade root bending moment, and total tower base bending moment are shown at the right side of the above figure for the given environmental condition

Figure 3.8 shows the fairlead and anchor tensions for the mooring line 1, 2, and 3 over the frequency range of $0.001 \leq \omega \leq 2.5\ rad/s$. The statistical results are summarized in Table 3.5 for both the frequency domain and time domain models using an aggregate of all the environmental conditions in time domain. Based on Table 3.5, mooring system shows consistent variation of results from 2.6% to 14.9% for the maximum fairlead and anchor tensions. However, the large variation of 4.9% to 23.8% is observed for the standard deviations. Among the three mooring lines, the minimum variation of the maximum fairlead and anchor tensions between the frequency domain

and time domain models is observed for line 1 with less than 10.2%. The maximum variation of this metric is also recorded for line 2 with less than 14.9%. The reason for the relatively large variation of the maximum fairlead and anchor tensions is the overprediction of these loads in the frequency domain model in comparison to the time domain model. Table 3.5 also shows relatively small variations (less than 10.1%) in the standard deviation of fairlead and anchor tensions for line 2. However, the comparison between the standard deviation of fairlead and anchor tensions for line 1 and 3 shows large variations from 10.8% to 12.2% and 6% to 23.8%, respectively.

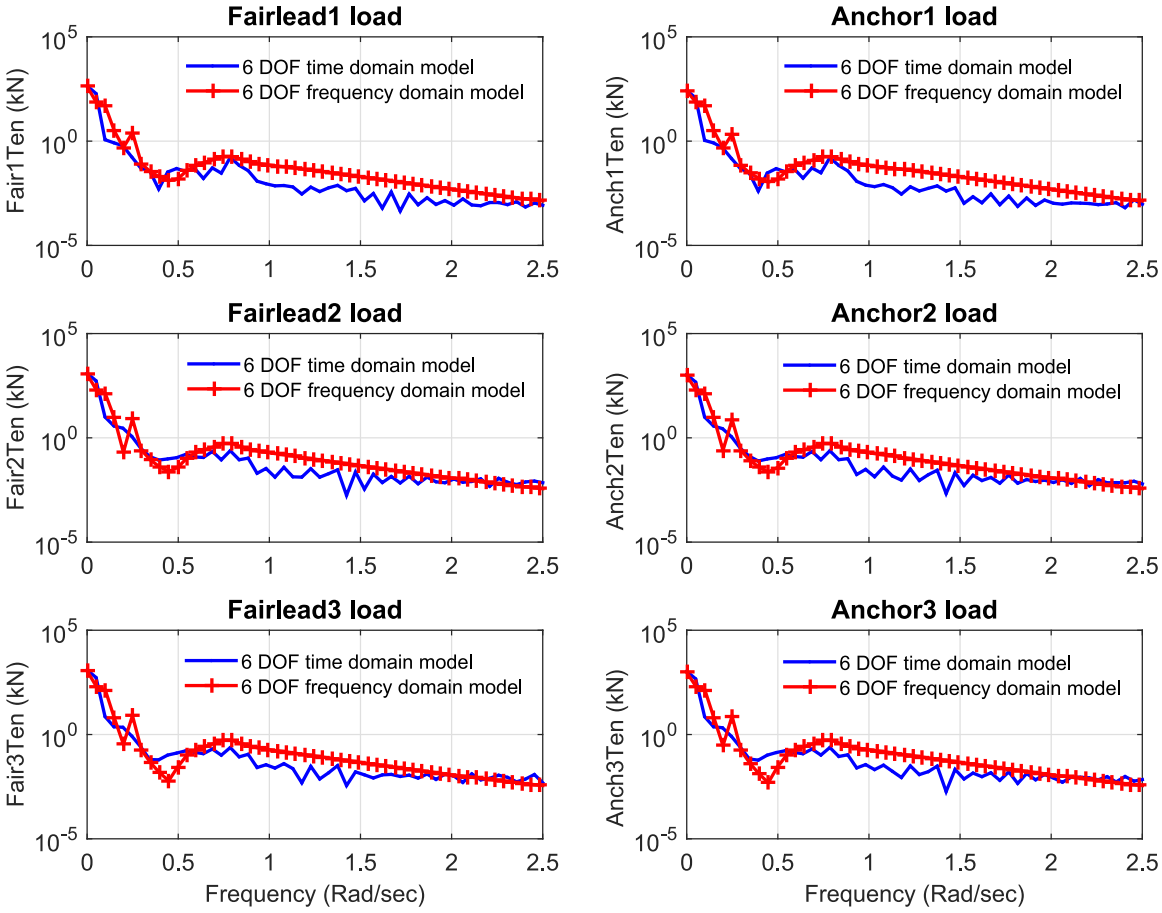

Figure 3.8: Results including the amplitude of fairlead and anchor tensions for mooring line 1, 2, and 3 of the OC3-Hywind spar buoy platform at the wind speed of 12 m/s

Table 3.5: Comparison of the frequency domain model and the time domain FAST results for the OC3-Hywind spar buoy platform. Maximum and standard deviation of the amplitude of the fairlead and anchor loads for both models compared in time domain using an aggregate of all the environmental conditions

Objective Parameters	Maximum			Standard Deviation		
	6 DOF Frequency domain model	6 DOF Time domain FAST	Variation (%)	6 DOF Frequency domain model	6 DOF Time domain FAST	Variation (%)
Fair1Ten (kN)	951	1,060	10.2	182.6	204.9	10.8
Anch1Ten (kN)	791	812.8	2.6	142.1	161.9	12.2
Fair2Ten (kN)	2,500	2,205.8	13.3	499.9	476.1	4.9
Anch2Ten (kN)	2,140	1,861.2	14.9	466.7	423	10.1
Fair3Ten (kN)	1,890	2,160.3	12.5	363.8	477.6	23.8
Anch3Ten (kN)	1,730	1,914.4	9.6	391.9	417.1	6

The lifetime fatigue analysis of the frequency domain and time domain models is summarized in Table 3.6. To correctly predict the lifetime fatigue loads on the wind turbine blade and tower as well as the platform fairleads and anchors, the time domain output variables for the operational wind speed range (see Table 3.3) are accumulated to calculate the damage cycle counts over the design lifetime. In this study, the wind turbine lifetime is 20 years, the ultimate load is 1.5 of the extreme load [99], the Wholer exponent (m) is 3 for the steel and 10 for the fiberglass components. As discussed in section 3.3, the rainflow cycles and accumulative damage equivalent loads are also calculated using Mlife. Based on the results presented in Table 3.6 for the OC3-Hywind spar buoy platform, the difference of fatigue loads for the blade root and tower base are 10% and 8.5%, respectively. The comparison of the fatigue load for the fairlead and anchor loads also shows variations of 2.7% to 18.9%. The ultimate loads also vary from 2.6% to 15% for the wind turbine and mooring system output variables.

Table 3.6: The ultimate load, mean load, and accumulative damage equivalent load (fatigue load) of the wind turbine blade and tower as well as the platform fairleads and anchors for the OC3-Hywind spar buoy platform

Objective Parameter	6 DOF Frequency domain model			6 DOF Time domain FAST			Variation of	Variation of
	Ultimate load	Mean load	Fatigue load	Ultimate load	Mean load	Fatigue load	Ultimate load (%)	Fatigue load (%)
RootMxyt (kN.m)	29,714	7,096	14,164	32,150	7,076	15,745	7.5	10
TwBsMxyt (kN.m)	245,150	50,649	112,740	275,160	54,717	123,302	10.9	8.5
Fair1Ten (kN)	1,426.5	322.7	462.2	1,590	354.2	518.4	10.3	10.8
Anch1Ten (kN)	1,186.2	221.6	349.9	1,218	236.7	395.8	2.6	11.5
Fair2Ten (kN)	3,750	747.1	1,041.7	3,307.5	772	1,105.2	13.3	5.7
Anch2Ten (kN)	3,210	650.2	976.3	2,791.8	657.1	1,004.1	15	2.7
Fair3Ten (kN)	2,835	615.3	895.7	3,242	769	1,105.5	12.5	18.9
Anch3Ten (kN)	2,595	511.3	799.9	2,870	662.4	947.7	9.5	15.6

3.4.4 MIT/NREL TLP case study

This section focuses on the comparison of the time domain and frequency domain results for the MIT/NREL TLP using an aggregate of all the environmental conditions. Note that the design parameters for this platform presented in Table 3.2. Figure 3.9 displays the amplitude of platform motions in surge, roll, and pitch as well as the amplitude of rotor thrust load, the total blade root bending moment, and the tower base bending moment in the frequency domain at the wind turbine operating condition. As already mentioned, the main reason for the differences in the amplitude of output variables in Fig. 3.9 is the average of short-time Fourier transforms of the time domain signals which are divided into 512 segments (windows). Table 3.7 is also provided to compare the maximum and the standard deviation of the results in time domain. For the platform motions, the results of the frequency domain model completely match with the time domain model. There is only small variation of 1.5% in the standard deviation of platform surge motions. As can be seen from Table 3.7, the maximum thrust load and the standard deviation of this load show variations of 6% and 13.4%.

The total blade root and the tower base bending moment variations over a frequency range are also shown in Fig. 3.9 at the rated wind speed and summarized in Table 3.7 for an aggregate of all the environmental conditions. The comparison of the maximum blade root bending moment and the standard deviation of this moment show variations of 7.2% and 9.2%, respectively. Statistical results also show variation of 6.2% for the maximum tower base bending moment, as well as 7.4% difference in their standard deviations.

Figure 3.10 shows the amplitude of fairlead and anchor tensions for the MIT/NREL TLP in the frequency domain at the wind turbine operating condition. Table 3.8 displays the fairlead and anchor tension variations as well as the statistical results for both the frequency domain and time domain models in the time domain using an aggregate of all the environmental conditions. Note that only 4 mooring lines of the

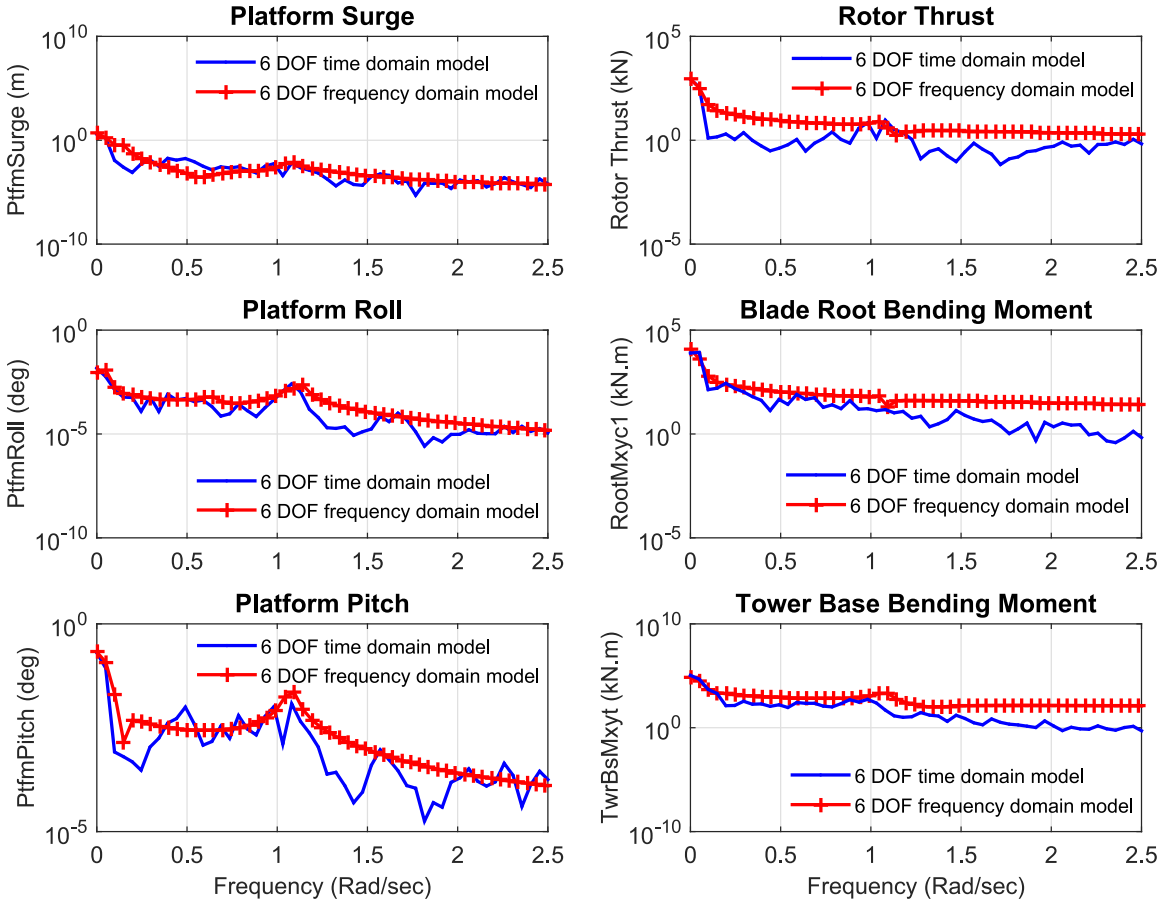

Figure 3.9: Results including the amplitude of platform surge, roll, and pitch motions of the MIT/NREL TLP at the wind turbine operating condition (wind speed of 12 m/s) are presented at the left side of the figure. The amplitude of rotor thrust, total blade root bending moment, and total tower base bending moment are shown at the right side of the above figure for the given environmental condition

MIT/NREL TLP have been chosen for this case study. Table 3.8 shows relatively large variations of fairlead and anchor tension loads (from 14.6% to 20.5%) in all the mooring lines. The reason for the relatively large variation of the fairlead and anchor tensions is the underprediction of these loads in the frequency domain model in comparison to the time domain model. For the mooring line 1 and 2, the maximum fairlead and anchor tensions vary from 17% to 18.6% with changes in their standard deviations from 16.8% to 18.1%. For the mooring line 3 and 4, the variation of maximum tensions and the standard deviations observed from 16.2% to 17.7% and from

Table 3.7: Comparison of the frequency domain model and the time domain FAST results for the MIT/NREL TLP. Maximum and standard deviation of the amplitude of the platform motions, total blade root and tower base bending moments for both models compared in time domain using an aggregate of all the environmental conditions

Objective Parameters	Maximum			Standard Deviation		
	6 DOF Frequency domain model	6 DOF Time domain FAST	Variation (%)	6 DOF Frequency domain model	6 DOF Time domain FAST	Variation (%)
PtfmSurge (m)	49.6	49.6	0	6.7	6.6	1.5
PtfmRoll (deg)	0.6	0.6	0	0.79	0.79	0
PtfmPitch (deg)	8.5	8.5	0	1.1	1.1	0
Rotor Thrust (kN)	1,910	2,033.7	6	403.9	466.7	13.4
RootMxyt (kN.m)	21,620	24,098	10.2	5,339.6	6,017	11.2
TwBsMxyt (kN.m)	150,700	163,910	8	36,429	40,057.9	9

14.6% to 20.5%, respectively.

Table 3.8: Comparison of the frequency domain model and the time domain FAST results for the MIT/NREL TLP. Maximum and standard deviation of the amplitude of the fairlead and anchor tensions for both models compared in time domain using an aggregate of all the environmental conditions

Objective Parameters	Maximum			Standard Deviation		
	6 DOF Frequency domain model	6 DOF Time domain FAST	Variation (%)	6 DOF Frequency domain model	6 DOF Time domain FAST	Variation (%)
Fair1Ten (kN)	4,880	5,883.1	17	1,137.3	1,368.1	16.8
Anch1Ten (kN)	4,720	5,644.3	16.3	1,081.8	1,317.5	17.8
Fair2Ten (kN)	5,140	6,320.1	18.6	1,392.8	1,702.3	18.1
Anch2Ten (kN)	4,990	6,065.2	17.7	1,346.6	1,638.1	17.7
Fair3Ten (kN)	7,020	8,537.9	17.7	1,665.6	2,097	20.5
Anch3Ten (kN)	6,930	8,276.9	16.2	1,732.3	2,029.2	14.6
Fair4Ten (kN)	4,970	6,006.9	17.2	1,446.8	1,709.9	15.3
Anch4Ten (kN)	4,820	5,769.2	16.4	1,395.5	1,641.3	14.9

The fatigue analysis of the frequency domain and time domain models for the MIT/NREL TLP is presented in Table 3.9. Based on the results presented in Table 3.9 for the MIT/NREL TLP, the difference of fatigue loads for the blade root and tower base are 9.9% and 4.8%, respectively. The comparison of the fatigue load for the fairlead and anchor loads also shows variations of 3.8% to 15.1%. The ultimate loads also vary from 5.8% to 18% for the wind turbine and mooring system output variables.

3.4.5 OC4-DeepCwind semisubmersible case study

The amplitude of the time domain and frequency domain results for the OC4-DeepCwind semisubmersible platform at the wind turbine operating condition are given in Fig.

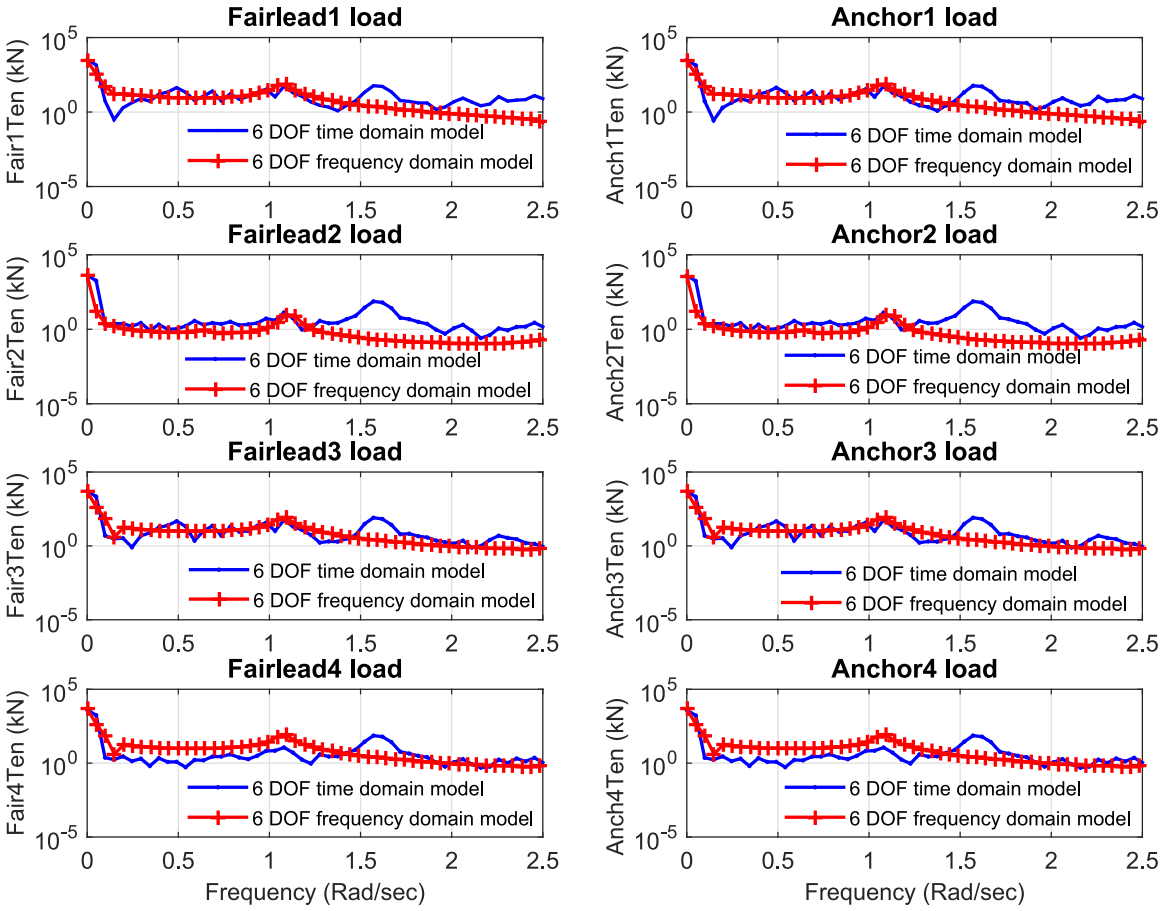

Figure 3.10: Results including the amplitude of fairlead and anchor tensions for the mooring line 1, 2, 3, and 4 of the MIT/NREL TLP at the wind speed of 12 m/s

Table 3.9: The ultimate load, mean load, and accumulative damage equivalent load (fatigue load) of the wind turbine blade and tower as well as the platform fairleads and anchors for the MIT/NREL TLP

Objective Parameter	6 DOF Frequency domain model			6 DOF Time domain FAST			Variation of	Variation of
	Ultimate load	Mean load	Fatigue load	Ultimate load	Mean load	Fatigue load	Ultimate load (%)	Fatigue load (%)
RootMxyt (kN.m)	32,189	7,813.3	14,522	36,148	7,940	16,125	10.9	9.9
TwBsMxyt (kN.m)	229,600	48,667	106,110	243,810	49,571	111,560	5.8	4.8
Fair1Ten (kN)	7,420	1,726.9	2,466.9	8,824.6	1,999.9	2,909.7	15.9	15.1
Anch1Ten (kN)	7,080	1,623.3	2,686.2	8,466.4	1,902.9	2,933.8	16.3	8.4
Fair2Ten (kN)	7,710	2,385.1	3,629	9,480	2,668.4	3,939.1	18	7.87
Anch2Ten (kN)	7,485	2,290.1	3,534.5	9,097.5	2,565	3,772.6	17.7	6.3
Fair3Ten (kN)	10,530	2,920	4,408	12,806	3,200	4,776.7	17.7	7.7
Anch3Ten (kN)	10,395	2,837	4,306.7	12,414	3,085.8	4,591.3	16.2	6.2
Fair4Ten (kN)	7,455	2,254.3	3,607.1	9,010.3	2,504.2	3,793.9	17.2	4.9
Anch4Ten (kN)	7,230	2,161.3	3,508.5	8,653.5	2,395	3,648.2	16.4	3.8

3.11 and Fig. 3.12. Figure 3.11 shows the amplitude of the platform responses in surge, roll, and pitch motions as well as the rotor thrust, total blade root bending moment, and tower base bending moment over the frequency range of $0.001 \leq \omega \leq 2.5$ rad/s. Note that the average of short-time Fourier transforms of the time domain signals impacts the shape of frequency domain plot significantly. The maximum value, the standard deviation, and the variation of the time domain results are summarized in Table 3.10 for both the frequency domain and time domain models considering an aggregate of all the environmental conditions.

As can be seen from Table 3.10, the surge motion shows relatively small variation of 5.3% in the maximum values. However, the comparison of the standard deviation for the surge motion shows larger variations of 9.8%. In addition, the statistical results for the maximum roll and pitch motions show variations of 13.3% and 13.2% with the standard deviations of 16.6% and 9%. The variations of 9.7% and 12.6% are also observed for the maximum and the standard deviation of the aerodynamic thrust load which can consequently lead to changes in the platform motions.

The total blade root and the tower base bending moment variations are also presented in Table 3.10. Based on this table, the difference between the maximum blade root bending moment for both the frequency domain and time domain models is 11.9% with 6.3% variation in its standard deviation for an aggregate of all the environmental conditions. As already mentioned, the non-linear blade root bending moments are averaged for comparison with the frequency domain model [55]. The maximum value of the tower base load and the variation of the standard deviation for the frequency domain model are 4.2% and 3.4% less than the time domain model.

Figure 3.12 shows the fairlead and anchor tensions for the mooring line 1, 2, and 3 over the frequency range of $0.001 \leq \omega \leq 2.5$ rad/s at the wind speed of 12 m/s. The statistical time domain results are also summarized in Table 3.11 for both the frequency domain and time domain models using an aggregate of all the environmental conditions. Based on Table 3.11, the mooring system shows consistent variation of

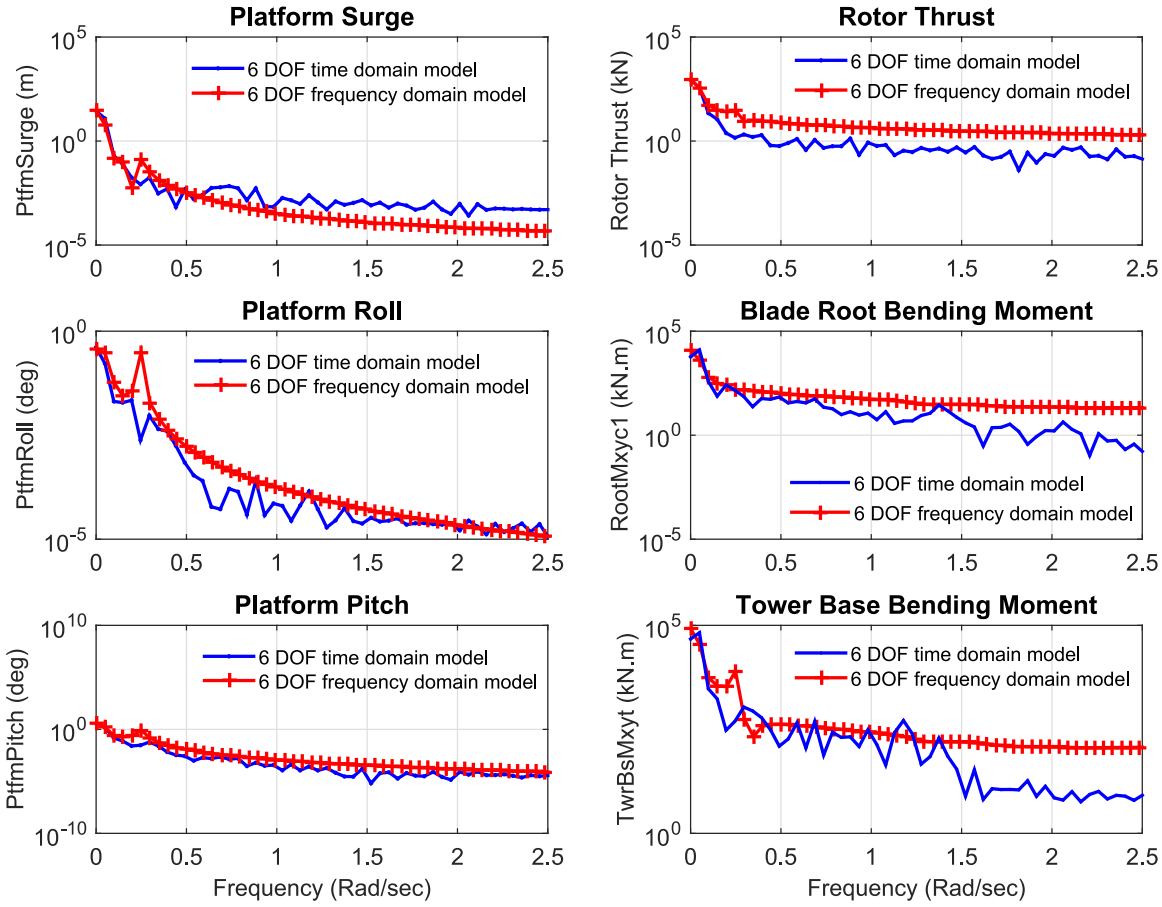

Figure 3.11: Results including the amplitude of platform surge, roll, and pitch motions of the OC4-DeepCwind semisubmersible platform at the wind turbine operating condition (wind speed of 12 m/s) are presented at the left side of the figure. The amplitude of rotor thrust, total blade root and tower base bending moments are shown at the right side of the above figure for the given environmental condition

results from zero to 12.5% for the maximum fairlead and anchor tensions. However, the relatively large variation of zero to 18.9% is observed for the standard deviation of the fairlead and anchor tensions. Among the three mooring lines, the minimum variation of the maximum fairlead and anchor tensions is observed at line 3. The maximum variation of this metric is also recorded at line 1 with variation of 8.2% to 12.5%. The reason for the relatively large variation of the maximum fairlead and anchor tensions at line 1 is the overprediction of these loads in the frequency domain model in comparison to the time domain model. Table 3.11 also shows variations of

Table 3.10: Comparison of the frequency domain model and the time domain FAST results for the OC4-DeepCwind semisubmersible platform. Maximum and standard deviation of the amplitude of the platform motions, total blade and tower bending moments for both models compared in time domain using an aggregate of all the environmental conditions

Objective Parameters	Maximum			Standard Deviation		
	6 DOF Frequency domain model	6 DOF Time domain FAST	Variation (%)	6 DOF Frequency domain model	6 DOF Time domain FAST	Variation (%)
PtfmSurge (m)	49.6	52.4	5.3	11.9	13.2	9.8
PtfmRoll (deg)	1.3	1.5	13.3	0.1	0.12	16.6
PtfmPitch (deg)	11.1	9.8	13.2	2.4	2.2	9
Rotor Thrust (kN)	1,830	2,028	9.7	432.7	495.1	12.6
RootMxyt (kN.m)	21,400	23,813	10.1	6,191.5	6,293.2	1.6
TwBsMxyt (kN.m)	199,600	205,870	3	46,836.4	47,305	0.9

2.6% to 7.2% in the maximum fairlead and anchor tensions of line 2. The comparison between the standard deviation of fairlead and anchor tensions of the mooring lines 1 and 2 shows variations of 3.6% to 18.9% and 0.1% to 4.5% due to the significant effect of the platform motions as well as the aerodynamic thrust load on these mooring lines. The standard deviation of fairlead and anchor 3 also varies from zero to 4.7%.

Table 3.11: Comparison of the frequency domain model and the time domain FAST results for the OC4-DeepCwind semisubmersible platform. Maximum and standard deviation of the amplitude of the fairlead and anchor loads for both models compared in time domain using an aggregate of all the environmental conditions

Objective Parameters	Maximum			Standard Deviation		
	6 DOF Frequency domain model	6 DOF Time domain FAST	Variation (%)	6 DOF Frequency domain model	6 DOF Time domain FAST	Variation (%)
Fair1Ten (kN)	1,440	1,280.7	12.5	298.9	288.5	3.6
Anch1Ten (kN)	1,060	978.9	8.2	260.2	218.8	18.9
Fair2Ten (kN)	2,490	2,426	2.6	512.6	537.1	4.5
Anch2Ten (kN)	2,280	2,126	7.2	476.3	475.7	0.1
Fair3Ten (kN)	1,460	1,460	0	212.9	223.6	4.7
Anch3Ten (kN)	1,310	1,310	0	202	202	0

The fatigue analysis of the frequency domain and time domain models for the OC4-DeepCwind semisubmersible platform is shown in Table 3.12. Based on the results presented in Table 3.12, the variation of fatigue loads for the blade root and tower are 8.6% and 4.4%. However, the fairlead and anchor fatigue loads vary from 2.7% to 21.2%. The reason for the relatively large variation of the fairlead and anchor fatigue loads is the overprediction of these loads in the frequency domain model in

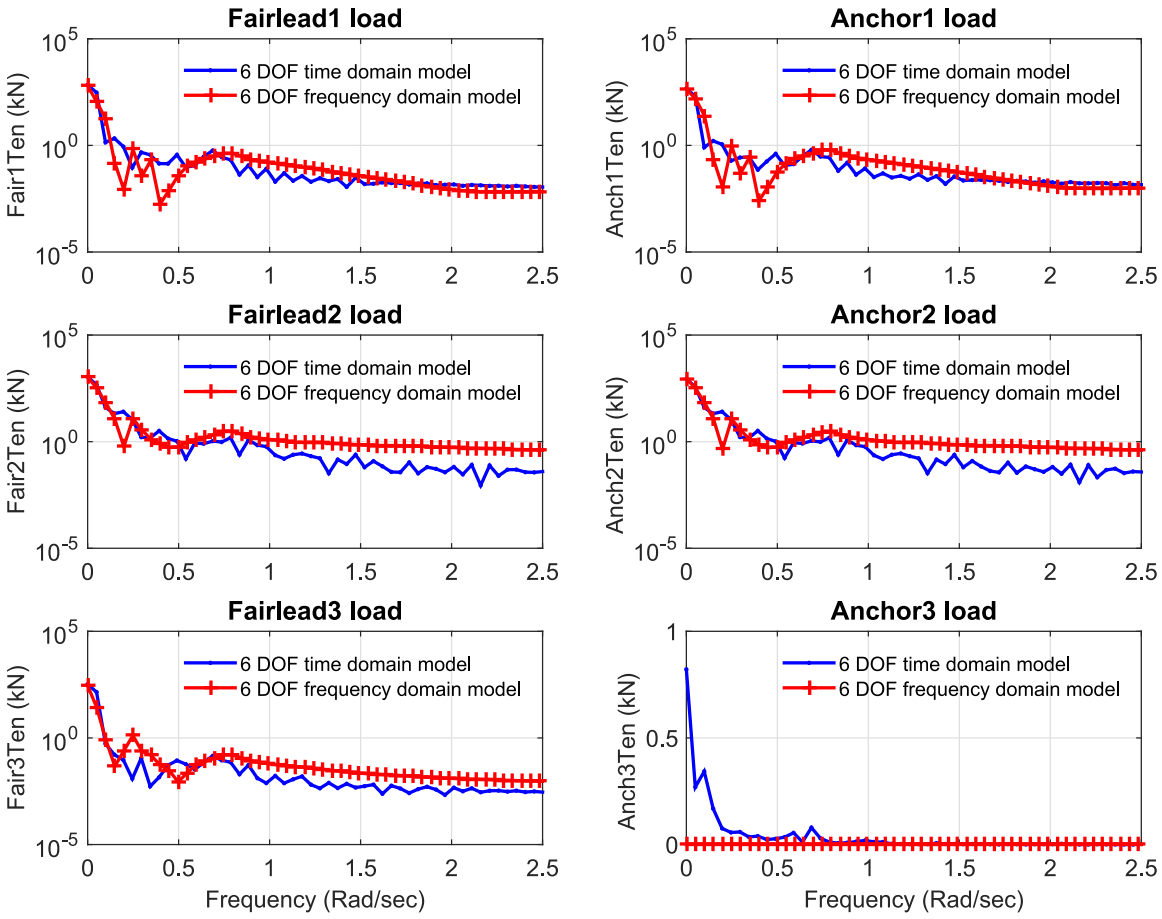

Figure 3.12: Results including the amplitude of fairlead and anchor tensions for mooring line 1, 2, and 3 of the OC4-DeepCwind semisubmersible platform at the wind speed of 12 m/s

comparison to the time domain model. The ultimate loads also vary from zero to 26.6% for the wind turbine and mooring system output variables.

3.4.6 Comparison of 22 DOF FAST and 6 DOF frequency domain model

The lifetime fatigue analysis of the 22 DOF time domain and the 6 DOF frequency domain results for the three baseline FOWTs are summarized in Table 3.13 considering an aggregate of all the environmental conditions. Based on the results presented in Table 3.13, the maximum variation of the fatigue load at the blade root is 5.3% for

Table 3.12: The ultimate load, mean load, and accumulative damage equivalent load (fatigue load) of the wind turbine blade and tower as well as the platform fairleads and anchors for the OC4-DeepCwind semisubmersible platform

Objective Parameter	6 DOF Frequency domain model			6 DOF Time domain FAST			Variation of	Variation of
	Ultimate load	Mean load	Fatigue load	Ultimate load	Mean load	Fatigue load	Ultimate load (%)	Fatigue load (%)
RootMxyt (kN.m)	32,123	7,878	14,756	34,279	7,970	16,158	6.2	8.6
TwBsMxyt (kN.m)	305,130	58,579	136,800	306,140	58,086	131,010	0.3	4.4
Fair1Ten (kN)	2,160	427.1	812.9	1,921	459.2	705.6	12.4	15.2
Anch1Ten (kN)	1,590	284.5	535.8	1,468.3	306.1	468.4	8.3	14.3
Fair2Ten (kN)	3,735	712.6	1,050.6	3,639	790.8	1,169	2.6	10.1
Anch2Ten (kN)	2,340	589.6	1,059.2	3,189	648	1,089.9	26.6	2.7
Fair3Ten (kN)	2,190	257.2	527.2	2,190	271.9	472.1	0	21.2
Anch3Ten (kN)	1,965	83.1	446.7	1,965	71.8	394.9	0	13.1

the OC4-DeepCwind semisubmersible. The maximum difference of the fatigue load at the tower base is 9.8% for the OC3-Hywind spar buoy.

The comparison of the fatigue loads for the fairleads and anchors shows large variations in one of the mooring systems of each baseline platform. The main reason for this difference is the unidirectional irregular waves in the time domain simulation which affects the downwave mooring lines (mooring line 3 in the OC3-Hywind, mooring line 1 in the MIT/NREL TLP, mooring line 3 in the OC4-DeepCwind). By removing this downwave mooring lines from the comparison, then the maximum variation of the fatigue load for the fairleads and anchors of all the platforms is 13.3%.

Table 3.13: The ultimate load and accumulative damage equivalent load (fatigue load) of the wind turbine blade and tower as well as the platform fairleads and anchors for all the baseline platforms in the 6 DOF frequency domain model and 22 DOF time domain FAST

Objective Parameter		6 DOF frequency domain model		22 DOF time domain FAST		Variation of	Variation of
		Ultimate load	Fatigue load	Ultimate load	Fatigue load	Ultimate load (%)	Fatigue load (%)
OC3-Hywind	RootMxyt (kN.m)	29,714	14,164	32,725	14,592	9.2	2.9
	TwBsMxyt (kN.m)	245,150	112,740	283,512	123,830	13.5	9.8
	Fair1Ten (kN)	1,426.5	462.2	1,661.5	517.1	14.1	10.6
	Anch1Ten (kN)	1,186.2	349.9	1,290	403.6	8	13.3
	Fair2Ten (kN)	3,750	1,041.7	3,301.5	1,093	13.5	4.7
	Anch2Ten (kN)	3,210	976.3	2,762.5	931.7	16.1	4.8
	Fair3Ten (kN)	2,835	895.7	3190	1,106.5	11	23.6
	Anch3Ten (kN)	2,595	799.9	2,820	994.7	7.9	19.5
MIT/NREL TLP	RootMxyt (kN.m)	32,189	14,522	35,813	14,861	10.1	2.2
	TwBsMxyt (kN.m)	229,600	106,110	245,800	106,750	6.5	0.5
	Fair1Ten (kN)	7,420	2,466.9	8,588	3,103	13.6	25.8
	Anch1Ten (kN)	7,080	2,686.2	8493	3,193	16.6	15.8
	Fair2Ten (kN)	7,710	3,629	9,009	3,990	14.4	9
	Anch2Ten (kN.)	7,485	3,534.5	8,850	3,805	15.4	7.1
	Fair3Ten (kN)	10,530	4,408	9,297	4562	13.2	3.3
	Anch3Ten (kN)	10,395	4,306.7	12670	4,419	16.8	2.5
	Fair4Ten (kN)	7,455	3,607.1	9,080	3,945	17.8	8.5
	Anch4Ten (kN)	7,230	3,508.5	8,654	3,789	16.4	7.4
OC4-DeepCwind	RootMxyt (kN.m)	32,123	14,756	35,279	15,584	0.4	5.3
	TwBsMxyt (kN.m)	305,130	136,800	307,220	132,110	0.6	3.5
	Fair1Ten (kN)	2,160	812.9	1,898	754.4	13.8	7.7
	Anch1Ten (kN)	1,590	535.8	1,495	491	6.3	8.9
	Fair2Ten (kN)	3,735	1,050.6	3,553	1,198	5.1	12.3
	Anch2Ten (kN)	2,340	1,059.2	2,805	1,056	16.5	0.2
	Fair3Ten (kN)	2,190	527.2	1,454	433	50.6	21.7
	Anch3Ten (kN)	1,965	446.7	1190	296	65.12	50.6

3.5 Conclusions and Future Work

In the past years, many studies have been done to develop time domain aero-hydro-servo tools for the FOWTs. For faster approximate results than time domain models, frequency domain models widely used as the predominant alternative. However, only a few of these frequency domain models have calculated the overall response of the FOWTs to wind and wave loading, and those only examined the harmonic or steady wind and wave conditions. These frequency domain models therefore potentially missed the significant impact of the turbulent winds and irregular waves on the platform displacements, and wind turbine blade and tower loads, as well as mooring system loads. This limitation in previous frequency domain models is probably due to the level of complexity in linearization of a FOWT using turbulent winds and irregular waves, since the numerical linearization is performed by perturbing the system variables about the operating point to achieve a converged solution. The work pre-

sented herein was a step forward in developing a simpler FOWT modeling technique that considers the coupled platform-turbine system in the frequency domain under turbulent winds and irregular wave conditions.

In this research, to carry out a new frequency domain approach for FOWTs, a validated tool, FAST, was selected to provide a frequency domain representation of FOWT dynamics. Then a model framework was created to define the frequency domain responses of the system under turbulent winds and irregular waves using wind and wave PSDs. To verify this approach, an NREL 5 MW offshore wind turbine with three classes of the baseline platforms including the OC3-Hywind, the MIT/NREL TLP, and the OC4-DeepCwind semisubmersible were examined using the output variables of 22 DOF and 6 DOF time domain models, as well as 6 DOF frequency domain model. The goal of this verification study was: first, to investigate the impacts of system flexibility reduction in the results of the time domain models, and second, to compare the statistical results of the platform displacements, turbine and tower loads, and mooring system loads, as well as lifetime fatigue loads for the 6 DOF and 22 DOF time domain and the 6 DOF frequency domain models.

The result comparison for the OC3-Hywind, MIT/NREL TLP, and the OC4-DeepCwind semisubmersible lead to the following insights. The comparison of the 6 DOF and 22 DOF time domain models shows consistent results for the key parameters of the wind turbine and baseline platforms. For the 6 DOF frequency domain and time domain models comparison, in terms of platform displacements, the difference between the results of the frequency domain and time domain models for the TLP is zero, the spar buoy platform shows small variations of 6.2% to 11.7%, and the semisubmersible shows relatively large variations of 5.3% to 13.2%. The comparison of the rotor thrust, total blade root bending moment, and total tower base bending moment shows a good agreement between the models for the TLP and the semisubmersible, and relatively large variations of 10.9% to 12.8% for the spar buoy platform. The best agreement between the fairlead and anchor tensions for both

the frequency domain and time domain models achieved for the semisubmersible and spar buoy platform and large variations of 16.2% to 18.6% obtained for the TLP. In terms of fatigue loads for the turbine blade root and tower base, the comparison of the results for the semisubmersible indicates small variations of 8.6% and 4.4%, while the spar buoy platform and the TLP show a relatively larger variations from 4.8% to 10%. The comparison of the fairlead and anchor fatigue loads displays the over-prediction of these loads in the frequency domain model of the semisubmersible and the underprediction of the fatigue loads for the spar buoy and TLP. It is noticeable that the deviation of the results between the 22 DOF time domain model and 6 DOF frequency domain model are lower than the cumulative variation of the modeling results between the 6 DOF time domain and 6 DOF frequency domain models due to apparently fortuitous pair of error trends.

There are a number of avenues for improving the framework examined in this study, including structural flexibility extensions, defining an active rotor collective pitch controller, as well as a variable speed controller. The future efforts are directed at using the current framework with a wide range of floating platforms, yielding structural performance, lifetime fatigue loads and cost estimates to ultimately compute cost of energy (COE) for the FOWTs. For this purpose, the presented frequency domain approach increases the computational efficiency of the design optimization of FOWTs. In the future, multi-fidelity optimization techniques might also be employed to correct the frequency domain model outputs with high-fidelity simulations.

Chapter 4

Multidisciplinary Design Optimization of Floating Offshore Wind Turbine Support Structures For Levelized Cost of Energy

This paper will be submitted to the journal *Renewable Energy*.

Karimi, Meysam, Abdulbaset Saad, Zuoming Dong, Brad Buckham, and Curran Crawford, "Multidisciplinary design optimization of floating offshore wind turbine support structures for levelized cost of energy".

This chapter presents a multidisciplinary design optimization approach for floating offshore wind turbines using a fully coupled frequency domain dynamic model developed in Chapter 3, a design parametrization scheme (see Chapter 2), a cost model, and a single objective optimization algorithm. The focus in this chapter is on evaluation and comparison of different classes of floating offshore wind turbines subject to levelized cost of energy across standard environmental conditions. To show the potential of the proposed method, the optimal design candidates of each platform class (from the subdivided design space) are compared with three baseline platforms.

Abstract This chapter presents a multidisciplinary design optimization approach for floating offshore wind turbine support structures with a design space that spans three stability classes of floating platforms. A design parameterization scheme and a frequency domain modeling approach were incorporated to calculate the overall system responses including motions, and design loads of a wide range of tension leg platforms, spar buoy platforms, and semisubmersibles to turbulent wind and irregular wave loads. To calculate the cost of each design candidate, a set of cost scaling tools for an offshore wind turbine was used. The levelized cost of energy was defined as a combination of initial capital cost, fixed charge ratio, annual operating expenses, and annual energy production. A Kriging-Bat optimization method was used to determine the minimum levelized cost of energy when pairing the 5 MW NREL offshore wind turbine with a moored platform. The potential of the method is demonstrated through three case studies - each determining potential design improvements on a conventional floating wind turbine platform design: the OC3-Hywind spar buoy, the MIT/NREL TLP, and the OC4-DeepCwind semisubmersible. Results for the tension leg and spar buoy case studies showed 5.21% and 3.1% decrease in the levelized cost of energy of the optimal design candidates in comparison to the MIT/NREL TLP and the OC3-Hywind respectively. Optimization results for the semisubmersible case study indicated that the levelized cost of energy decreased by 1.52% for the optimal design in comparison to the OC4-DeepCwind.

keywords Multidisciplinary design optimization, Wind turbine, Offshore, Floating platform, Cost of energy

4.1 Introduction

During the past decade, the offshore wind energy sector has developed rapidly from a global cumulative installed offshore wind capacity of 1,800 MW in 2007 to 18,814 MW in 2017 [100]. Although a significant part of this energy production is generated using

turbines with bottom fixed support structures in shallow waters, the trend is toward building FOWTs in deep waters [54, 56]. However, a move to FOWT technology introduces a myriad of potential techniques to support the turbine tower, nacelle and rotor assembly. For any given choice, there are complex interactions of the mooring mechanics, platform hydrodynamics, rotor aerodynamics and the system controllers that determine system performance and cost. Consequently, the engineering design of moored FOWT support structures requires the development of a multidisciplinary design optimization (MDO) framework to automate early stage assessment of platform-turbine system dynamics, economics, and survivability. This work is focused on an MDO framework for selecting optimal FOWT platform configurations using linearized coupled aerodynamics, hydrodynamics, structural dynamics, and platform/mooring design parametrizations.

The three established FOWT classes are the TLP, a spar buoy platform, and a semisubmersible platform as shown in Fig. 4.1. For all the platform classes, mooring lines, ballast mass, displacement or a combination of these parameters stabilizes the floating system, and all three are usually deployed in water depth of greater than 60 m [2]. The TLP achieves stability through taut vertical mooring lines and displacement. The spar buoy platform, also known as ballast-stabilized class, uses a relatively high sub-structure ballast and steel mass and a deep draft with three catenary mooring lines. The semisubmersible platform, also called buoyancy-stabilized class, utilize a set of multi-cylinder configurations that surround the central tower with a catenary mooring system.

Several studies in the past have developed techniques for fully coupled dynamic simulation, design optimization, and cost analysis of offshore wind energy, with most of the studies being focused on time domain simulation codes to predict the behavior of FOWTs. A brief review of these studies is summarized as below.

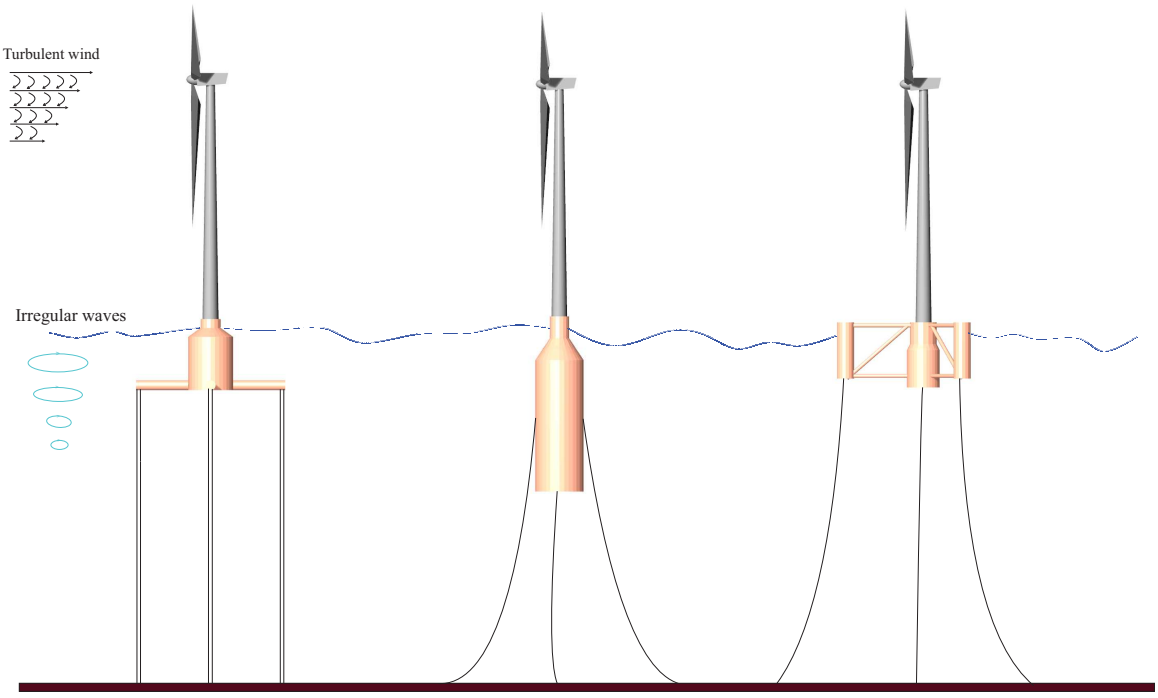

Figure 4.1: Three classes of FOWTs in a turbulent wind and irregular waves. From left to right: a mooring stabilized (tension leg) platform, ballast stabilized (spar buoy), buoyancy stabilized (semisubmersible).

4.1.1 FOWT time domain dynamics modeling

In the context of dynamic response analysis of FOWTs, it is common to use non-linear time domain tools to model the hydrodynamic and aerodynamic loading, mooring lines, and motions of the floating support structures. One of the first fully coupled aero-hydro-servo-elastic simulation tools, referred to as FAST, was developed by Jonkman and Buhl Jr [7]. Jonkman's FAST with HydroDyn module is widely used for simulation of FOWTs in the several studies [4, 16, 43, 51, 57, 60, 61, 83]. Skaare et al [59] developed a computer tool using HAWC2 [8] and the SIMO/RIFLEX for simulating the dynamic response of FOWTs exposed to wind, wave and current forces. Shirzadeh et al [101], Karimirad and Moan [102], Paulsen et al [103], Damgaard et al [104] used HAWC2 to address coupled wave and wind induced motions of FOWTs. Bossanyi [9] developed BLADED which is a time domain tool to calculate the aerodynamic and hydrodynamic loads of FOWTs.

4.1.2 FOWT frequency domain dynamics modeling

Alternative to non-linear time domain simulations, there is a simpler modeling technique in the literature which uses a linearization of the system dynamics in order to facilitate frequency domain analysis of FOWTs. This approach is widely used for floating offshore structures in the literature [10, 11, 60, 80, 81]. The linearization of FOWTs is usually accomplished using a time domain simulation code. FAST is widely used for the linearization of FOWTs in the literature [12–16, 83]. FAST perturbs the state variables to obtain steady state conditions for the system displacements and reaction forces/moments- these changes are then used to determine the coefficients of the linearized model. The weakness of the FAST code is that the linearization of the floating system imposes steady wind and still water approximations.

One of the first frequency domain offshore wind turbine codes TURBU developed by van Engelen and Braam [84] to model fixed bottom offshore wind turbines. Lupton [55] developed a frequency domain approach to model the overall responses of FOWTs to harmonic wind and wave loading. A new frequency domain approach for a coupled wind turbine, floating platform, and mooring system was explained in Chapter 3. In this study, irregular wave and turbulent wind loads were incorporated to the frequency domain model developed in this dissertation using wave and wind power spectral densities (PSDs).

4.1.3 Design optimization studies

Several studies in the past have proposed comparison analysis of the different classes of FOWT support structures [4, 23–27]. However, in the context of the FOWT support structure design optimization, there is a lack of studies that explore and analyze a wide range of support structure design classes. One of the first support structure design optimization studies for four design classes including a TLP, a spar buoy, and two buoyancy stabilized platforms was performed by Wayman [12]. Tracy [14] presented a comprehensive design optimization study for the single-body floating

support structures to evaluate design candidates across the design space. Parker [29] developed an optimization framework to perform the parametric analysis of the design of mooring-stabilized platforms. Fylling and Berthelsen [30] presented an optimization study subject to the stability of a wide range of spar buoy platforms and mooring line costs. Myhr et al [32] used optimization routines to find the optimal geometry and mooring line layout for tension leg buoy (TLB) platforms subject to the platform cost. A design optimization of floating wind turbine support structures for three stabilized classes of floating platforms including single-body and multi-body platforms presented by Hall [15], Karimi et al [16], Hall et al [33]. An extensive review of the recent studies and approaches in the design optimization of FOWT support structures was provided by Muskulus and Schafhirt [34].

4.1.4 Cost models

The wind turbine rotor, gearbox, and tower have the highest cost contribution of the total offshore wind turbine cost [105]. Fingersh et al [17] developed a set of cost scaling functions and a tool to estimate the levelized cost of energy (LCOE) of onshore and offshore wind turbines based on turbine power rating, rotor diameter, hub height, and other key turbine and support structure features. Fingeresh et al.'s cost model is used in the studies by Ashuri et al [105], Dinwoodie and McMillan [106], Fischer et al [107]. Rademakers et al [108] developed an operating and maintenance cost estimator (OMCE) tool to calculate the costs of offshore wind farms. Myhr et al [18] used OMCE to estimate the cost of offshore wind farms. Ozkan [19] developed an offshore wind integrated cost model (OFWIC) which includes the power market to estimate the electricity prices for offshore wind energy. Roeth et al [109], Dykes et al [110] used OFWIC model for financial analysis of offshore wind energy. Hofmann [20] provided an overview of existing onshore and offshore wind turbine/wind farm cost models with their main characteristics.

4.1.5 Proposed model

In the current study, an integrated MDO framework is developed for FOWTs to simultaneously design the platform and mooring system using a parametrization scheme for three platform stabilization classes. A fully coupled frequency domain dynamic model is also integrated to the MDO framework to evaluate the internal forces, system motions, and other dynamic variables from the frequency domain outputs. Using the frequency domain dynamic model and the parametric scheme to numerically span the design space, an MDO of FOWT support structure is executed.

The approach taken for this MDO problem is to find the optimum floating support structure design for each stabilized classes that can then be used as a starting point in the detailed design processes. To identify the optimal concept, the Kriging-Bat optimization algorithm [22] in this work is focused on the task of finding a global minima. Each global minima in this study is the minimum of the LCOE using Fingeresh et al.'s cost model for a 5 MW NREL offshore wind turbine [40] across the range of possible floating support structures.

4.1.6 Chapter outline

The remainder of this chapter is structured in three main sections as follows. The architecture of the MDO framework including the linearized aero-hydro-elastic model, support structure parametrization, and the optimization problem formulation is discussed in section 4.2. In section 4.3, the results of the optimized NREL offshore 5 MW wind turbine for the three stabilized classes of floating platforms are compared with the NREL FOWT baseline models- OC3-Hywind spar buoy [5], MIT/NREL TLP [4], and OC4-DeepCwind semisubmersible [6]. Finally, section 4.4 presents the conclusions drawn from this study and directions for future work.

4.2 Methodology

In the following subsections, we describe how the MDO architecture is assembled from four main constituent blocks; these are: support structure parametrization, frequency domain dynamic model, cost esmtimation model, and optimization problem formulation. The functional relationships between these blocks are shown in Figs. 4.2 and 4.4.

4.2.1 MDO framework

A series of multidisciplinary computational tools is used in this MDO framework to manipulate the design variables and consequently the objective function. Most of these tools have been developed for wind energy and floating platform studies, and are listed in Table 4.1. To make a framework for integrating and automating the design process, the computational tools have been coupled such that the objective function could be linked to the optimizer as shown in Fig. 4.2. This automation is achieved using a MATLAB-based script to manage the dataflow between all the tools in the MDO framework.

In the current study, the platform and mooring design variables, design load cases, and the wind turbine properties are passed to a linearized aero-hydro-servo model, which computes the complete suite of system external and internal loads for the coupled system. Then, the computed objective function from the cost model and design constraints are passed to the optimizer in an iterative approach until the optimal solution is achieved.

4.2.2 Support structure parametrization

The support structure parametrization scheme uses a finite set of design variables to describe the widest range of feasible FOWT platforms and mooring system configurations. The platform geometry, connective elements, platform mass and inertia,

Table 4.1: Computational tools and models used in the MDO architecture.

Tools and Models	Usage
WAMIT	Computes hydrodynamic coefficients and wave excitation for each platform[111]
AeroDyn	Models the aerodynamic loads [112]
HydroDyn	Models the hydrodynamic loads [91]
FAST	Models the linearized aero-hydro-servo-elastic behaviour of the floating wind turbine
TurbSim	Simulate the steady wind flow [95]
MBC	Generates azimuth-averaged of the wind turbine properties [96]
Mlife	Computes rain-flow cyles using time series in fatigue analysis [98]
Cost model	Computes cost components [17]
MATLAB	Integrates the computational tools to the optimization algorithm[48]

and mooring line arrangements and properties were first described in past work (c.f. Section 2.3 in Chapter 2) and we summarized the salient features in the following subsections. Note that the design space is subdivided into 3 sub-domains (TLP, spar buoy, and semisubmersible) to complete three different optimizations within each sub-domain.

Platform geometry

The geometric design variables for the three classes of floating platforms are illustrated in Fig. 4.3. The platform geometries are formed by vertical cylinders with variable radius and draft, an array of outer cylinders, circular heave plates, top taper ratio of the central cylinder draft, cross-bracing elements, and tendon arms as provided in Table 4.2. A free board of 10 m is considered for all the platform designs as a constant design parameter [5].

The mass and inertia properties of each platform are specified by the platform geometry and the ballast mass which is set according to the surplus buoyancy of the platform to achieve the specific freeboard. The wall thickness of vertical cylinders and

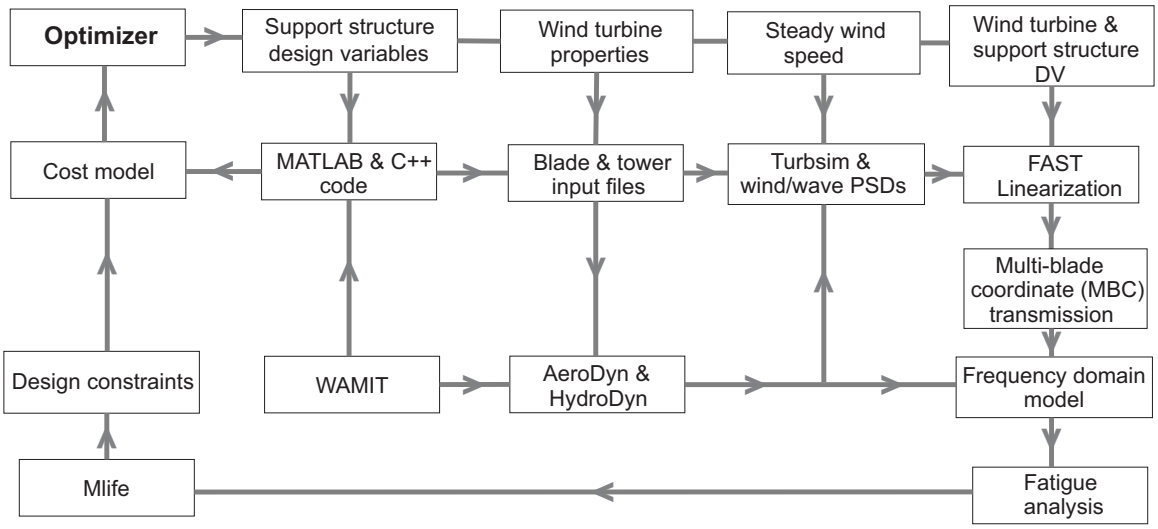

Figure 4.2: The integrated MDO architecture with required computational tools. This architecture shows how optimizer is coupled to the wind turbine and support structure design variables and computational tools. The gray lines show the data flow between all the tools which is automated using a MATLAB-based script.

heave plates are considered 50 mm and 30 mm respectively [16, 51]. The total platform mass and inertia is estimated by superposing the masses of the vertical cylinders, heave plates, cross-bracing members, and tendon arms using the steel density of 8,050 kg/m^3 as well as the density of 2,400 kg/m^3 for the concrete ballast mass.

Mooring system

The mooring line configuration is defined based on different platform classes, from taut lines to slack catenary mooring lines in the parametrization scheme. Hence, an additional design variable for the mooring system, X_M, is added to the platform design variables described in the previous subsection. This design variable transitions between taut vertical lines ($-1 \leq X_M \leq 0$), angled taut lines ($0 < X_M \leq 1$), and slack catenary lines ($1 < X_M \leq 3$) as discussed in [16].

For the TLP design, four pairs of taut vertical lines are used and they are connected at the end of each tendon arm as shown in Fig. 4.1. The anchor of this platform class is located directly under the fairlead. For the spar buoy and semisubmersible

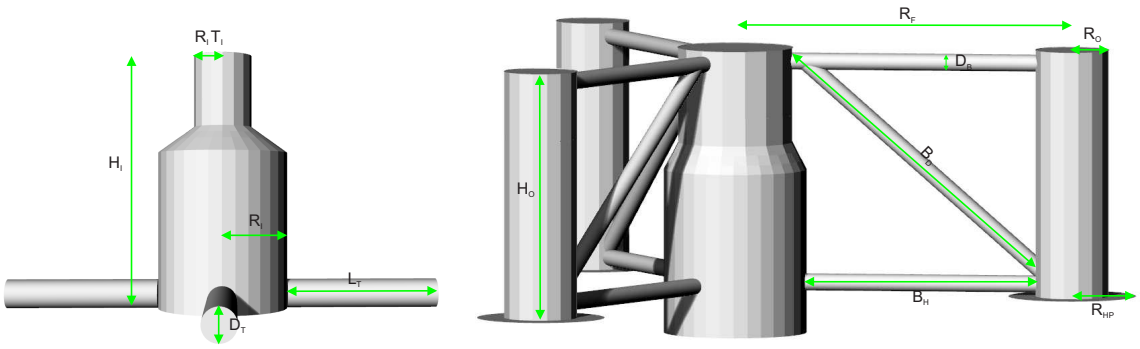

Figure 4.3: Design variables for three platform classes including the inner and outer cylinders radius and draft, diameter and length of the connective elements, and radius of the outer cylinders array for a semisubmersible platform.

Table 4.2: Geometric design variables of platforms with the lower and upper bounds of each variable. The length and diameter of tendon arm and cross-bracing members are the function of fairlead tension, mooring design variable X_M, and buoyancy loads.

Design variables	**Description**	**Variations**
H_I	Inner cylinder draft (m)	$2 \leq H_I \leq 150$
R_I	Inner cylinder radius (m)	$3 \leq R_I \leq 25$
T_I	Top taper ratio	$0.2 \leq T_I \leq 2$
R_F	Radius of outer cylinder array (m)	$5 \leq T_I \leq 40$
H_O	Outer cylinder draft (m)	$3 \leq H_O \leq 50$
R_O	Outer cylinder radii (m)	$1.5 \leq R_O \leq 10$
R_{HP}	Outer cylinders heave plate radii (m)	$0 \leq R_{HP} \leq 20$
D_T	Tendon arm diameter (m)	$f(fairlead\ tension)$
L_T	Tendon arm length (m)	$f(mooring\ design\ variable\ X_M)$
B_H	Cross-bracing horizontal length (m)	$f(R_F, R_O, R_I)$
B_D	Cross-bracing diagonal length (m)	$f(R_F, H_O, H_I)$
D_B	Diameter of the cross-bracing (m)	$f(max(buoyancy, fairlead\ tension))$

platforms, three lines are used and they are connected to the fairlead at the half of the cylindrical draft and at the bottom of each outer cylinder respectively (see Fig. 4.1). The anchor location for these two platform classes are determined from the horizontal spread of the water depth as illustrated in Table 4.3. All the mooring system properties for three classes of the floating platforms are summarized in Table 4.3.

Table 4.3: Design parameters of mooring systems for three specific platform types.

Design parameters	**TLP**	**Spar buoy platform**	**Semisubmersible platform**
Mooring technology	Four pairs of taut vertical line	Three angled taut lines or slack catenary lines	Three angled taut lines or slack catenary lines
X_M Variations	$-1 \leq X_M \leq 0$	$0 < X_M \leq 3$	$0 < X_M \leq 3$
Line mass density (kg/m)	116.027	77.7	113.35
Modulus of elasticity (Pa)	1.18E+09	6E+08	1.66E+09
Line diameter (m)	0.127	0.09	0.076
Line extensional stiffness (N)	1.5E+09	384.243E+06	7.536E+08
Horizontal distance (l_x) of anchor from fairlead (m)	0	$X_M \times Water\ depth$	$X_M \times Water\ depth$
Vertical distance (l_z) of anchor from fairlead (m)	$Water\ depth - H_I$	$Water\ depth - H_I/2$	$Water\ depth - H_O$
Unstretched mooring line length (m)	(Water depth - H_I)-1	$\sqrt{l_x^2 + l_z^2} + \frac{l_z}{12}$	$\sqrt{l_x^2 + l_z^2} + \frac{l_z}{12}$

4.2.3 Frequency domain aero-hydro-servo model

To predict the coupled platform-turbine system motions and survivability, a frequency domain dynamics modeling approach, which is developed in Chapter 3, is used here in the MDO framework. This model provides a quick and accurate insight on system aerodynamics, hydrodynamics, and structural dynamics and has been shown to capture the static and dynamic behavior of FOWT systems across all three platform classes mentioned earlier in the real world turbulent wind and irregular wave loads.

In the frequency domain modeling framework, the wind turbine blade, nacelle, and tower properties are assumed rigid with no structural DOF, and the rotor rotational speed is assumed constant. The motions of floating support structures are described in 6 DOF including surge, sway, heave, roll, pitch, and yaw.

The frequency domain model is assembled using the validated numerical tools FAST, WAMIT, and TurbSim are used for a FOWT design as shown in Fig. 4.2. For each candidate design, a frequency domain model is assembled by first using FAST to complete a linearization process considering still water, steady wind, a predefined collective blade pitch controller, and frequency independent hydrodynamic coefficients calculated using WAMIT for the specific candidate platform geometry. In this solution for the steady state condition, frequency independent added mass and damping coefficients are used to extract energy from the platform and attenuate oscillations in order to expedite the convergence on the operating point. Once the steady state

(or operating point) has been calculated, the linearized system's mass, damping and stiffness matrices are computed through the conventional process of perturbing the system state (all 6 platform DOFs), the rotor pitch angle, the wind speed disturbances, and the state dependent reaction forces. For more details about the FAST linearization and the governing equations, the reader is referred to the FAST users guide [7] and the study presented in Chapter 3.

Model assembly

The linearization output files require a multi-blade coordinate (MBC) transformation to generate the azimuth-averaged mass M_{avg}, damping C_{avg}, and stiffness K_{avg}. Note that in the frequency domain equation of motion, the constant added mass and damping values, which were used in the linearization process, subtracted from the azimuth-averaged mass and damping matrices. Moreover, the MBC transformation generates output variables Y_{opt}, displacement output matrix $DspC_{avg}$, velocity output matrix $VelC_{avg}$, pitch control F and wind input disturbance F_d input matrices for the frequency representation of a system dynamics at the operating point. Then the irregular wave and turbulent wind loads are incorporated to the frequency domain model using JONSWAP $S_j(\omega)$ [90] and Kaimal $S_k(\omega)$ [94] power spectral densities (PSDs). The resulting linearized frequency domain equation of motion is shown in Eq. 4.1:

$$\begin{aligned} &-\omega^2\Big(M_{avg}+M_a(\omega)\Big)\Delta q(\omega)e^{i\omega t} \\ &+i\omega\Big(C_{avg}+C_p(\omega)\Big)\Delta q(\omega)e^{i\omega t}+\Big(K_{avg}\Big)\Delta q(\omega)e^{i\omega t} \\ =&\left(F_w\left(\sqrt{2\ S_J(\omega)\Delta\omega}\right)+F_d\left(\sqrt{2\ S_k(\omega)\Delta\omega}\right)+F\Delta u(\omega)\right)e^{i\omega t} \end{aligned} \tag{4.1}$$

where $\Delta q(\omega)e^{i\omega t}=\Delta q(t)$, $M_a(\omega)$ is the platform added mass, $C_p(\omega)$ is the platform damping matrix, and F_w is the wave excitation vector calculated using WAMIT. $\Delta u(\omega)$ is the collective blade pitch controller (rotor pitch) vector, and ω is the fre-

quency of the steady system response. Note that external forces are independent for each frequency component, ω. In addition, the relative phases of the external forces are assumed to be zero, since detail of phases cannot be extracted from PSDs.

Output variables

By using the state variable q from Eq. 4.1, azimuth-averaged matrices from the MBC, and the FAST capability to develop a series of output variables. The linearized representation of the output variables are given as:

$$\begin{aligned} Y_j(\omega) = &\left| i\omega VelC_{j\times k}\ \Delta q_{k\times j}(\omega) \right| + \left| DspC_{j\times k}\ \Delta q_{k\times j}(\omega) \right| \\ &+ \left| D_{dj}\Delta u_d(\omega) \right| + \left| D_j \Delta u(\omega) \right| + Y_{op_j}(\omega) \end{aligned} \tag{4.2}$$

where $Y(\omega)$ is the amplitude of the output variables, $\Delta u_d(\omega)$ is the vector of wind input disturbance, D_d is the wind input disturbance transmission matrix, and D is the control input transmission matrix. In the above equation, j subscript shows the number of output variables and k subscript presents the system's DOF. The frequency domain output variables include any linear combination of dynamic model state variables, internal forces and moments such as blade root and tower base bending moment, and fairlead/anchor loads (see Table 4.8 for a list of output variables in this chapter).

Fatigue and extreme load analysis

In order to perform the fatigue-life analysis for a design candidate, the amplitude of the output variables (Eq. 4.2) is converted to the time domain data file using the following equation:

$$\zeta(t) = \sum_{i=1}^{N} (Y_i \cos(\omega_i t + \phi_i)) \tag{4.3}$$

where $\zeta(t)$ is the time series generated from the amplitude of the output variables Y, N is the number of frequency bins, time t in seconds, and associated frequency ω_i and random phase ϕ_i. Then the lifetime fatigue analysis is completed using the cycle counting of the variable-amplitude load ranges, ultimate loads, mean loads, and wind speed distribution as discussed in Hayman and Buhl Jr [97] and presented in Section 3.3 of Chapter 3 .

4.2.4 Cost estimation

There are various factors to consider when the final goal is to determine an optimal energy generation system. However, when considering a large-scale deployment of a system like the FOWT, the cost of energy is the dominant factor [18]. The approach taken to obtain the cost of FOWTs, which leads to the calculation of LCOE, is similar to Fingersh et al [17], and only the main aspects of the design cost and scaling model for an offshore wind turbine are presented in the following items:

Turbine capital cost (TCC) . The TCC displays the cost of all the main wind turbine components including rotor, drivetrain and nacelle, control, safety system, condition monitoring, tower, and marinization (extra cost to protect an offshore system against marine environment). All the aforementioned TCC components are the function of machine rating, rotor diameter, hub height, and rotor rotational speed in the cost model.

Balance of station cost (BOS) . The BOS encompasses all the cost components of a FOWT system other than the wind turbine cost. This includes platform, mooring and anchor cost as well as offshore transportation, port and staging equipment, offshore turbine installation, offshore electrical interface/connections, offshore permits, engineering and site assessment, personal access equipment, and offshore warranty premium.

In this design cost and scaling model, the floating platform cost is a function of design variables defined in section 4.2.2. A constant cost per mass of $\$1/kg$ is considered for the platform cylinder and connection materials, and cost of $\$0.083/kg$ for the concrete ballast materials. The cost of the mooring system is calculated using the total length of the lines and the maximum mooring line tension which is observed to occur at the fairlead. Hence, a constant cost of $\$5/m - kN$ is defined for the mooring lines which is multiplied by the safety factor of 5. This provides the line cost results within the range of costs spanned by Musial et al [113], Kim et al [114]. The anchor cost is a combination of anchor installation and technology costs which is summarized in Table 4.4. Similar to the mooring line cost model, the maximum anchor tension and the safety factor of 5 is used for each anchor technology cost [16].

Table 4.4: Cost model for three anchor systems including installation and technology cost.

Anchor technology	**Line angle**	**$/anchor/kN (Line tension)**	**$/anchor (Installation)**
Drag embedment	$0^o - 10^o$	100	50000
VLA	$10^o - 45^o$	120	80000
Suction pile	$45^o - 90^o$	150	110000

Initial capital cost (ICC) . The ICC is the sum of the TCC and the BOS (c.f. Section 3.2.3 in [17]) . Note that ICC does not include construction financing or financing fees, since these are taken into account through the fixed charge rate (FCR).

Levelized replacement cost (LRC) . The LRC is a cost factor to cover the life-time replacements and overhauls of major wind turbine components such as generators, gearboxes, and blades. The LRC is an explicit function of machine rating.

Operations and maintenance cost (OMC) . The OMC covers the scheduled and unscheduled mechanical and electrical maintenance expenditures of the offshore

wind turbine. The cost model assumes a fixed cost per kWh of energy converted as an estimate for the OMC.

Land lease cost (LLC) . The LLC includes the ocean bottom lease cost for an offshore wind turbine which is defined as a fixed cost per kWh in the cost model.

Annual operating expenses (AOE) . The AOE is the sum of the LRC, the OMC, and the LLC (c.f. Section 3.2.4 in [17]).

Note that the cost model was developed based on 2005 costs and it needs to be calibrated based on the costs components in the present time. To compensate for the cost fluctuations, a cost escalation model is used based on the producer price index (PPI) of the U.S Department of Labor, Bureau of Labor Statistics. Moreover, a labor cost escalator, which is specified as the general inflation index, is the gross domestic product (GDP) for the cost components such as AOE, marinization, offshore warranty, etc. In this study, the general inflation index is 1.27 and PPI varies for different components of the offshore wind turbine such as shaft, bearing, hub, etc.

4.2.5 Optimization problem formulation

The general formulation for a single objective design optimization problem is:

$$Find \quad x = [x_1, x_2, ., x_k] \quad that\ minimizes \quad J(x) \tag{4.4}$$

where $J(x)$ is the objective function, and x is a k-dimensional vector of design variables with lower and upper bounds subject to inequality constraints:

$$x_{lower} \leq x \leq x_{upper} \tag{4.5}$$

$$g_j(x) \leq 0; \quad j = 1 \text{ to } p \tag{4.6}$$

where p is the number of inequality constraint functions g_j. To achieve optimal design configurations for floating support structures, an optimization algorithm with the LCOE as an objective function and eleven cost and design constraints are used in this MDO problem for a specific case of offshore wind turbine.

Objective function

In this study, the LCOE is used as a multidisciplinary objective function because it reflects the cost of energy production for FOWTs in a coupled analysis system.

Annual energy production (AEP) . The net AEP is the maximum amount of generated electricity in a year based on the machine rating, wind speed distribution (Weibull distribution), and the power curve of the wind turbine:

$$AEP_{net} \approx 8760 \times \sum_{i=cut-in}^{cut-out} P(V_i).f(V_i) \tag{4.7}$$

where V_i represents the discretized wind speed with a bin interval of 4, 6, 8, ..., 24 m/s, 8760 is the number of hours per year, P_V is the power curve of the wind turbine, and $f(V_i)$ is the wind speed distribution which is defined as:

$$f(V_i) = (\frac{k}{c}).(\frac{V_i}{c})^{k-1} e^{\left[-(\frac{V_i}{c})^k\right]} \tag{4.8}$$

where k is the shape factor of 2 and c is the scale factor of 9.47 [105]. Note that due to using the same wind turbine on each candidate platform, the AEP_{net} value is uniform across all design candidates considered in this work.

Levelized cost of energy (LCOE) . By using all the aforementioned cost (see Section 4.2.4) and wind energy factors, the LCOE is calculated by the following equation:

$$LCOE = \frac{FCR \times ICC + AOE}{AEP_{net}} \tag{4.9}$$

where FCR is an annual value per $ of the ICC required to cover the return on debt and equity, depreciation, income tax, property tax, and insurance. A constant value is considered for the FCR in the design cost and scaling model.

Design constraints

In addition to the design variable bounds discussed in section 4.2.2, complex constraints are enforced that ensure the mooring and internal structural loads with the candidate design are within allowable limits. Table 4.5 lists the design constraints and the partial safety factors which are prescribed in this study.

Table 4.5: Wind turbine, support structure, and mooring line cost and design constraints.

Index	Design constraint	Value	Partial safety factor
1	Support structure cost (M$)	≤ 12	N/A
2	Nacelle acceleration (m/s^2)	≤ 1	N/A
3	Platform pitch angle (deg)	≤ 10	N/A
4	Platform mass (tons)	≥ 2500	N/A
5	Blade root fatigue damage rate (-)	≤ 1	1.38 [115]
6	Tower base fatigue damage rate (-)	≤ 1	1.38 [115]
7	Breaking strength of offshore mooring steel wire rope (kN)	$\leq 18,000$	1.15 [116]
8	Breaking strength of offshore mooring chain- spar (kN)	$\leq 8,100$	1.15 [116]
9	Breaking strength of offshore mooring chain- semisub (kN)	$\leq 5,800$	1.15 [116]
10	Total blade root stress (MPa)	≤ 325	1.62 [105]
11	Total tower base stress (MPa)	≤ 270	1.62 [105]

To avoid expensive support structures, an inequality cost constraint limit the sum of platform cost, mooring cost, and anchor cost to less than \$12 M [6]. To keep the platform and wind turbine stable, the maximum standard deviation of nacelle acceleration is limited to 1 m/s^2 [14]. In order to avoid over-turning of the floating

system, the platform pitch angle should be less than 10 degrees at all instants in an aggregate of all environmental conditions [15]. A platform mass of less than 2500 *tons* is avoided to prevent insufficient buoyancy of the FOWT.

To avoid the failure of the blade elements, the maximum allowable fatigue damage of 1 and the stress constraint (yield stress) of 325 MPa are applied to the blade root by considering that the blade is made of composite materials with the Wholer exponent of 10 [105]. In addition, a maximum allowable fatigue damage of 1 and the stress constraint (yield stress) of 270 MPa are assumed for the tower base considering that the tower is made of structural steel with the Wholer exponent of 3 [105]. Note that the blade root and tower base fatigue damages and stresses are calculated based on the ultimate loads (1.5 of the extreme load) and fatigue analysis explained in section 4.2.3.

To avoid mooring line failure, the breaking strengths of 18,000 kN, 8,100 kN, and 5,800 kN are defined for TLPs, spar buoys, and semisubmersible platforms respectively (as prescribed by DNV GL standards [117, 118]).

Optimization algorithm

As a population-based random search algorithm, the Bat algorithm (BA) was introduced by Yang [119]. BA has been successfully applied in many real-world optimization problems because of its easy implementation in global optimum searches. The Kriging-Surrogate model (K-SM) method has the performance of high robust and global convergence [120]. Therefore, in this work the Kriging-Bat algorithm (K-BA) is used, which combines the K-SM and BA to increase the efficiency of the BA to find the global optimal solutions [22].

Note that the BA requires thousands of function evaluations to locate a global optimum, which impedes its application in computationally expensive problems. The basic idea of the K-BA is to approximate the original objective function using K-SM. The K-BA algorithm starts with a Design of Experiments (DOE) using Latin

Hypercube Sampling (LHS) techniques [121], which allows for sampling the objective function within the considered domain, and then constructs a K-SM to approximate the expensive function. Based on the latter, new points are chosen and added at each iteration to the initial DOE samples, in order to improve the quality of the approximation, as evaluated by K-SM metrics. In this work, the size of population of the K-BA was chosen to be 20 candidates as the initial sample across the design space with a maximum number of function evaluation of 600 before the algorithm converges to the optimal design. In addition, a tolerance value of 1E-06 is applied as a stoping criteria. More details about the K-BA algorithm and its comparison with other search methods can be found in Saad et al [22].

Figure 4.4 shows the data and process flow of different computational tools in the MDO framework that captures the dynamic responses of a FOWT in standard design load cases and evaluates the design constraints and objective function. This integration is achieved using a MATLAB-based script to manage the design optimization. Note that the computational cost of the steps (e.g. FAST, WAMIT, and Mlife run times) per design candidate is very fast for frequency domain modeling and overall runtimes to get the final optimal solutions.

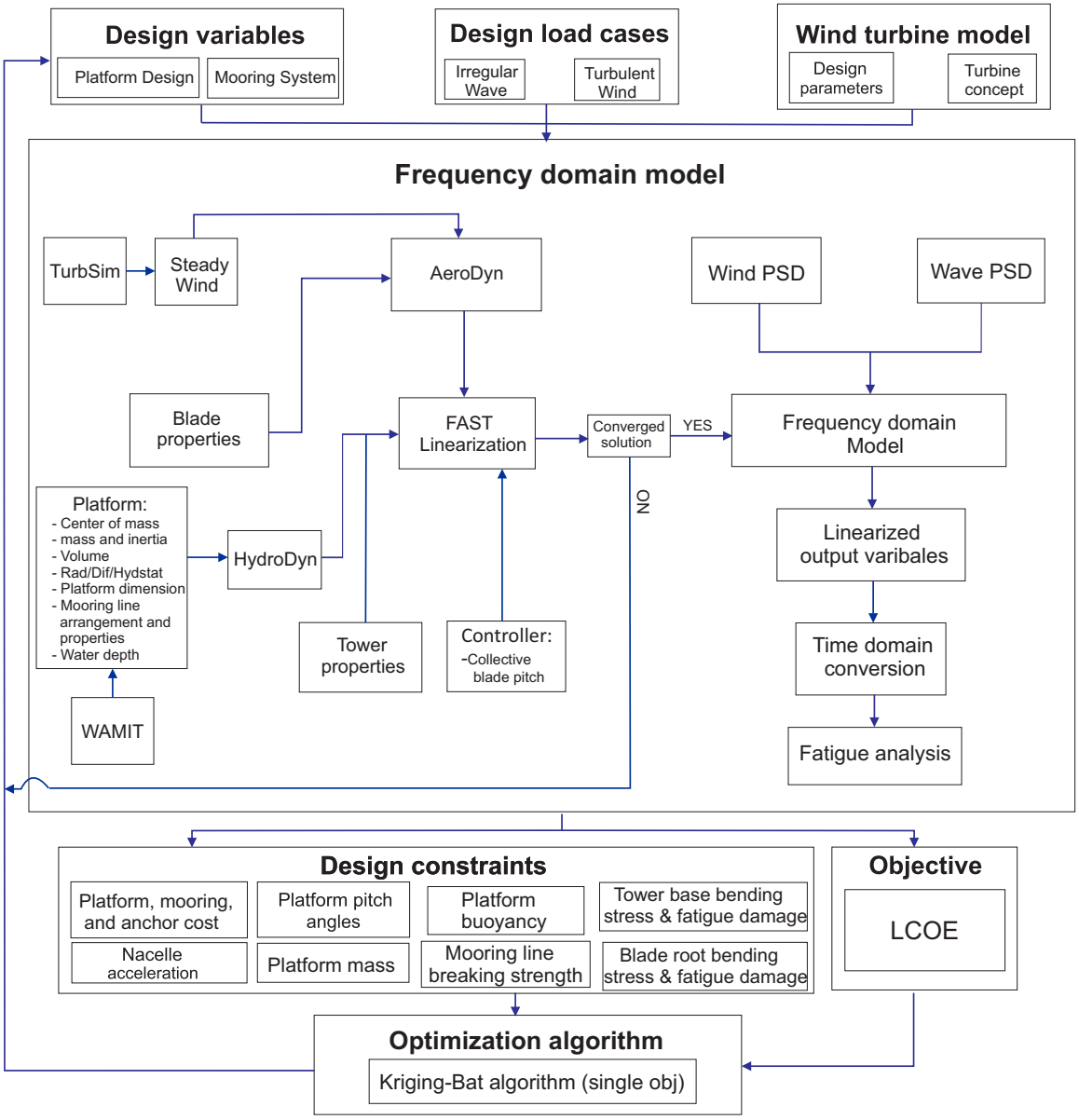

Figure 4.4: Fully coupled MDO block diagram to show the data and process flow of different computational components.

4.3 Results

This section presents the optimization results using the NREL offshore 5 MW horizontal axis wind turbine and three stabilized classes of support structures. For all the design cases, the TCC is \$7.13 M, the LRC is \$0.1 M, the OMC is \$0.59 M, the LLC is \$0.03 M, and the FCR is 11.58%. The optimization algorithm spans across the design space which is subdivided into 3 sub-domains in order to force the optimization to reveal the best possible platform candidate in each class. This will allow the techno-economic tradeoffs that exist between classes to be fully elucidated. Consequently, the optimization results are presented in the TLP, spar buoy, and semisubmersible design cases. In addition, the optimal design cases are compared with three baseline FOWTs including the MIT/NREL TLP, the OC3-Hywind, and the OC4-DeepCwind semisubmersible. Note that the optimization is repeated 10 times for each platform case to find the optimum design using the baseline models as the initial population. The range of environmental conditions as well as the results from each stage are discussed separately in the following subsections.

4.3.1 Environmental conditions

In this study, a water depth of 200 m is used for the TLP and semisubmersible platform designs, and a water depth of 300 m is considered for the spar buoy platforms to maintain the consistency being considered between this MDO study and prior studies of the three baseline platform designs. A range of steady wind speeds from 4 m/s to 24 m/s with 2 m/s increments at the hub height with corresponding peak periods T_p and significant wave heights H_s are presented in Table 4.6. The peak shape parameter of 3.3 is defined for the wave spectrum, JONSWAP. For the wind spectra, Kaimal shape is used with an integral length scale of 28.35 and a standard deviation of wind speed of 1.2 m/s [93]. The spectral discretization of the waves and winds is at a resolution of 0.0497 rad/s over the range of $0.001 \leq \omega \leq 12.65$ rad/s. For

the sake of evaluating the internal forces and system motions, an aggregate of all the environmental conditions is used. Note that multi-seeds (6 random phases for each condition) are used for the environmental conditions to get a set of statistically meaningful results. The fatigue load analysis is also performed considering the operating design load case (DLC) 1.2, which is recommended by IEC 61400-3 design standard. To calculate the fatigue ratio, the ultimate load is assumed as 1.5 of the extreme load generated from the time domain results. The net AEP is 23871E3 kWh (as discussed in Section 4.2.5) for all the design cases in the MDO framework.

Table 4.6: Environmental conditions over the operational wind speed range for partially developed waves for DLC 1.2 [60]

Objective Parameters	**Environmental Conditions**										
Mean Wind Speed (m/s)	4	6	8	10	12	14	16	18	20	22	24
Wave Height (m)	1.1	1.9	2.5	2.9	3.4	4	4.9	5.1	5.5	6.2	6.9
Peak Period (s)	2.9	3.2	3.9	4.3	5.1	5.9	6.4	7.2	8.7	9.1	9.7

4.3.2 TLP design class

To define the TLP support structure, a cylindrical element with six design variables including cylinder draft H_I, cylinder radius R_I, top taper ratio T_I, tendon arm length L_T, tendon arm diameter D_T, and taut vertical mooring lines, $-1 \leq X_M \leq 0$, are used in the MDO of this platform.

Figure 4.5 illustrates the design space for the TLP in terms of LCOE and number of design evaluations. The visualization of a group of platform candidates as well as the optimal platform design is also shown in Fig. 4.5. The geometry, cost components, and the LCOE of each labelled platform are summarized in Table 4.7.

As can be seen from Fig. 4.5 and Table 4.7, platform D is found to be the most optimal design with the lowest support structure cost of \$3.09 M and the minimum LCOE of 11.26E-2 \$/kWh. The design space also presents the highest support structure cost of \$3.44 M for platform A with the maximum LCOE of 11.43E-2 \$/kWh.

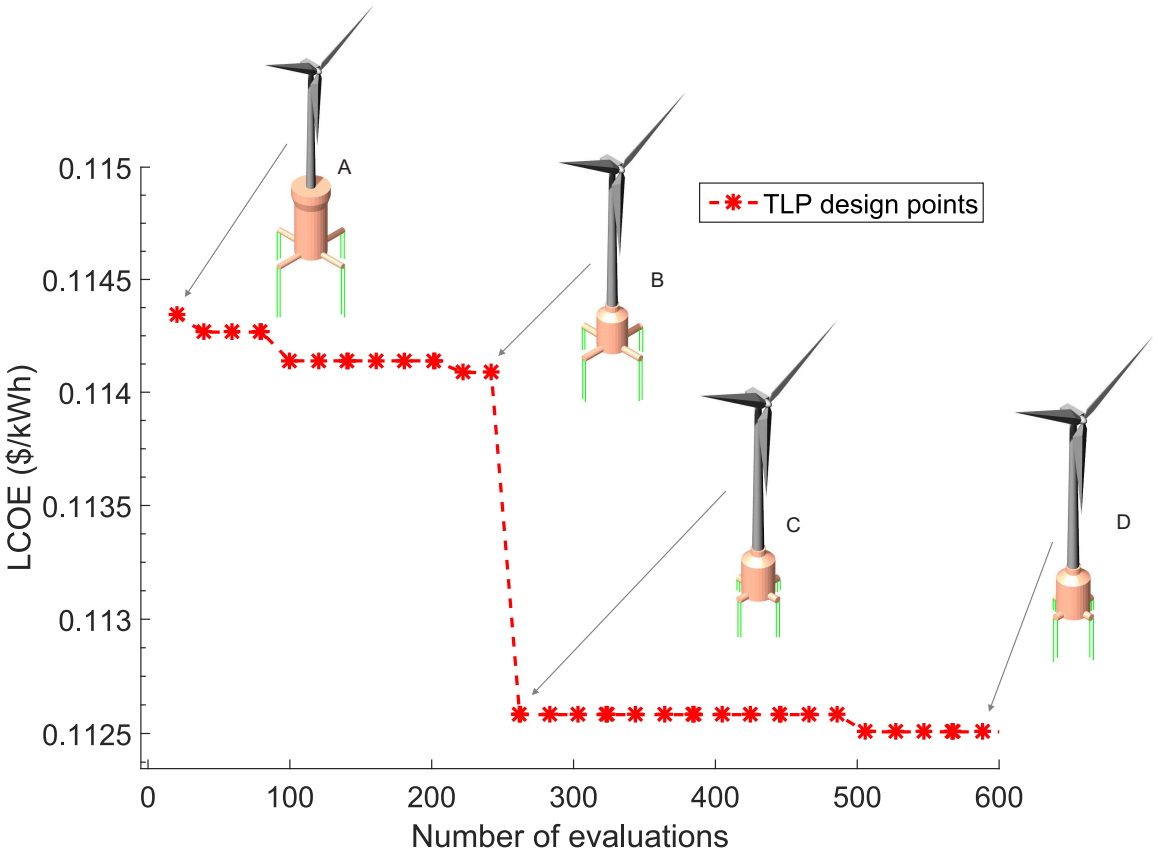

Figure 4.5: Design exploration of TLPs subject to the LCOE and number of design evaluations. Four design candidates including the optimal platform (D) are presented in the design space. The reason for the sharp declination in the design space between 200 to 300 evaluations is the cost sensitivity of the TLP designs as already discussed in Section 2.6.5 of Chapter 2.

In addition to the design candidates shown in Figure 4.5, the design and cost components of the MIT/NREL TLP are presented in Table 4.7. The cost model indicates the support structure cost of \$4.34 M for the MIT/NREL TLP with the LCOE of 11.88E-2 \$/kWh, which is 5.21% higher than the calculated LCOE for platform D.

From the details of each TLP design (Table 4.7), it is apparent that there is a consistent trend along the design components as the support structure and LCOE decrease. This trend shows that although the draft and radius have been roughly the same for all the platform candidates, the platform taper ratio, and tendon arm length and diameter decrease among platforms A to D. The more slender floats are reducing

Table 4.7: Platform characteristics, cost components, and calculated objective function (LCOE) for TLP designs and the MIT/NREL TLP baseline model.

Design and cost components	**Units**	**Tension-leg platforms**				
		A	**B**	**C**	**D**	**MIT/NREL TLP**
Draft (H_I)	m	42.13	42.23	42.32	42.36	47.89
Radius (R_I)	m	8.85	9.34	9.43	9.52	9
Taper ratio (T_I)	N/A	1.19	0.55	0.46	0.44	1
Mooring line type (X_M)	N/A	-0.08	-0.19	-0.09	-0.06	-0.36
Tendon arm length (L_T)	m	4.1	9.5	4.5	3.35	18
Tendon arm diameter (D_T)	m	3.92	3.2	3.02	2.95	2.65
Support structure cost	1000 $	3449.3	3320.6	3109.4	3099.6	4344.5
Balance of station cost (BOS)	1000 $	10132.3	9999.7	9782.2	9772.1	11054.4
Levelized cost of energy (LCOE)	$/kWh	11.43E-2	11.37E-2	11.26E-2	11.26E-2	11.88E-2

the platform's cost and sensitivity to wave excitation which affect the fairlead and anchor tensions.

The wind turbine blade root and tower base bending stresses and fatigue damage rates as well as the platform ultimate fairlead loads (FairTen) and ultimate anchor loads (AnchTen) for the optimal TLP (platform D) and the MIT/NREL TLP are listed in Table 4.8. The accumulative fatigue damage rate experienced at the of tower base for platform D is higher than for the baseline platform. Table 4.8 displays also higher bending stresses and ultimate fairlead/anchor loads for platform D.

Table 4.8: The accumulative fatigue damage rates and bending stresses of the wind turbine blade root and tower base as well as the platform ultimate fairlead and anchor loads for the optimal TLP (platform D) and the MIT/NREL TLP.

Design parameters	**Platform D**	**MIT/NREL TLP**
Blade root bending stress (MPa)	10.4	9.2
Tower base bending stress (MPa)	36.1	14.9
Blade root fatigue damage rate (-)	0.37	0.48
Tower base fatigue damage rate (-)	0.69	0.33
Fair1Ten (kN)	17,458	7,420
Anch1Ten (kN)	16,529	7,080
Fair2Ten (kN)	9,812	7,710
Anch2Ten (kN)	9,512	7,485
Fair3Ten (kN)	17,040	10,530
Anch3Ten (kN)	17,212	10,395
Fair4Ten (kN)	9,399	7,455
Anch4Ten (kN)	9,231	7,230

4.3.3 Spar buoy design class

To define the spar buoy platform, a cylindrical element with four design variables including cylinder draft H_I, cylinder radius R_I, top taper ratio T_I, and angled taut/slack catenary mooring lines, $0 < X_M \leq 3$, are used in the MDO of this platform.

Figure 4.6 presents the design space for the spar buoy platform in terms of LCOE and number of design evaluations. The visualization of a group of platform candidates as well as the optimal platform design is shown in Fig. 4.7. The geometry, cost components, and the LCOE of each labelled platform are summarized in Table 4.9.

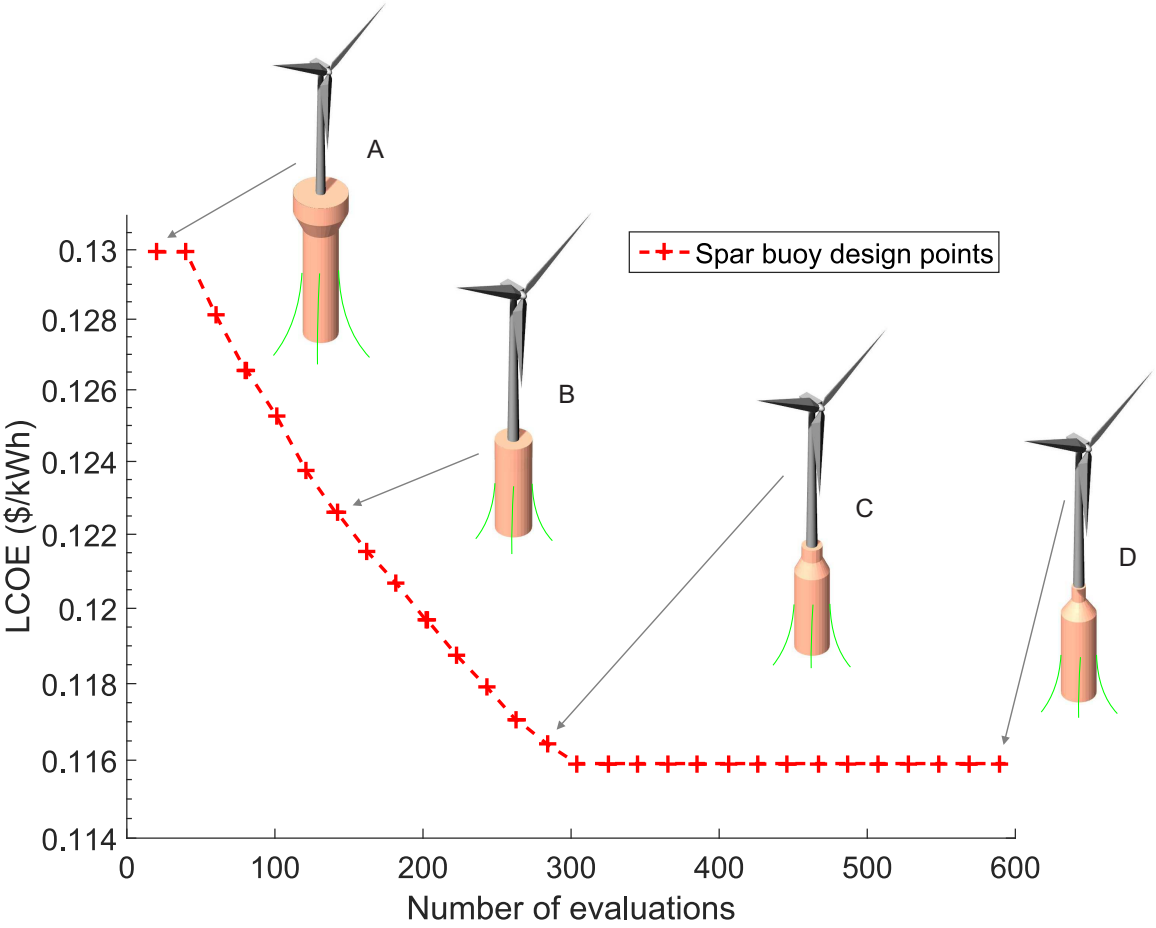

Figure 4.6: Design exploration of spar buoy platforms subject to the LCOE and number of design evaluations. Four design candidates including the optimal platform (D) are presented in the design space

For the spar buoy design configuration, the support structure costs are distributed between \$3.76 M to \$6.55 M for platforms A to D. From Fig. 4.6 and Table 4.9, it can be seen that platforms D and A represent the lowest and highest LCOE of 11.59E-2 \$/kWh and 12.98E-2 \$/kWh respectively. Moreover, the details of design and cost components of the OC3-Hywind spar buoy platform are summarized in Table 4.9 as a baseline model. The cost model shows the support structure cost of \$4.49 M for the OC3-Hywind platform with the LCOE of 11.95E-2 \$/kWh, which is 3.1% higher than the calculated LCOE for platform D.

Table 4.9: Platform characteristics, cost components, and calculated objective function (LCOE) for spar buoy platform designs and the OC3-Hywind baseline model.

Design and cost components	**Units**	**Spar buoy platforms**				
		A	**B**	**C**	**D**	**OC3-Hywind**
Draft (H_I)	m	86.92	86.88	86.88	86.85	120
Radius (R_I)	m	9.12	8.88	8.46	8.38	6.5
Taper ratio (T_I)	N/A	1.55	0.96	0.25	0.2	0.69
Mooring line type (X_M)	N/A	2.08	2	1.99	1.97	2.88
Support structure cost	1000 \$	6551.8	5091.7	3859	3760.1	4496.8
Balance of station cost (BOS)	1000 \$	13327.9	11823.9	10554.2	10452.4	11211.2
Levelized cost of energy (LCOE)	\$/kWh	12.98E-2	12.25E-2	11.63E-2	11.59E-2	11.95E-2

By using the details of platforms from Table 4.9, the apparent trend for the spar buoy design candidates is the predominant influence of two design parameters, platform radius and taper ratio, as the support structure cost and the LCOE decrease. As already explained, the more slender floats are reducing the platform's cost and sensitivity to wave excitation. consequently, the fairlead/anchor tension decreases.

The blade root and tower base bending stresses and fatigue damage rates as well as the platform ultimate fairlead and anchor loads for the optimal spar buoy (platform D) and the OC3-Hywind are listed in Table 4.10. As the table displays, only for platform D is the tower base accumulated fatigue damage ratio higher than that for baseline platform. Table 4.10 indicates also higher ultimate fairlead and anchor loads for the baseline platform.

Table 4.10: The accumulative fatigue damages and bending stresses of the wind turbine blade root and tower base as well as the platform ultimate fairlead and anchor loads for the optimal spar buoy (platform D) and the OC3-Hywind.

Design parameters	**Platform D**	**MIT/NREL TLP**
Blade root bending stress (MPa)	9.1	9.3
Tower base bending stress (MPa)	12	10.2
Blade root fatigue damage rate (-)	0.49	0.78
Tower base fatigue damage rate (-)	0.87	0.42
Fair1Ten (kN)	980	1,426
Anch1Ten (kN)	825	1,186.2
Fair2Ten (kN)	822	3,750
Anch2Ten (kN)	604	3,210
Fair3Ten (kN)	933	2,835
Anch3Ten (kN)	714	2,595

4.3.4 Semisubmersible design class

This section focuses on the MDO results for semisubmersible platforms. This multi-body structure is defined with eleven design variables including inner cylinder draft H_I, inner cylinder radius R_I, top taper ratio T_I, radius of outer cylinders array R_F, outer cylinders draft H_O, outer cylinders radius R_O, outer cylinders heave plate radius R_{HP}, cross-bracing horizontal length B_H, cross-bracing diagonal length B_D, diameter of the cross-bracing D_B, and angled taut/slack catenary mooring lines, $0 < X_M \leq 3$.

The design space of semisubmersible platforms, which includes one inner cylinder and three outer cylinders, is indicated in Fig. 4.7 along with the visualization of a group platform candidates as well as the optimal platform design. The geometry, cost components, and the LCOE of each labelled platform are summarized in Table 4.11.

The semisubmersible designs with four total floats in Fig. 7 are indicated by representative platforms A to D. As can be seen from Table 4.11, platform D is the optimal design with the lowest support structure cost of \$4.13 M and the minimum LCOE of 11.77E-2 \$/kWh. The highest support structure cost of \$4.84 M is calculated for platform A with the maximum LCOE of 12.13E-2 \$/kWh. To compare the results of the optimal design case with a baseline model, the design and cost components of

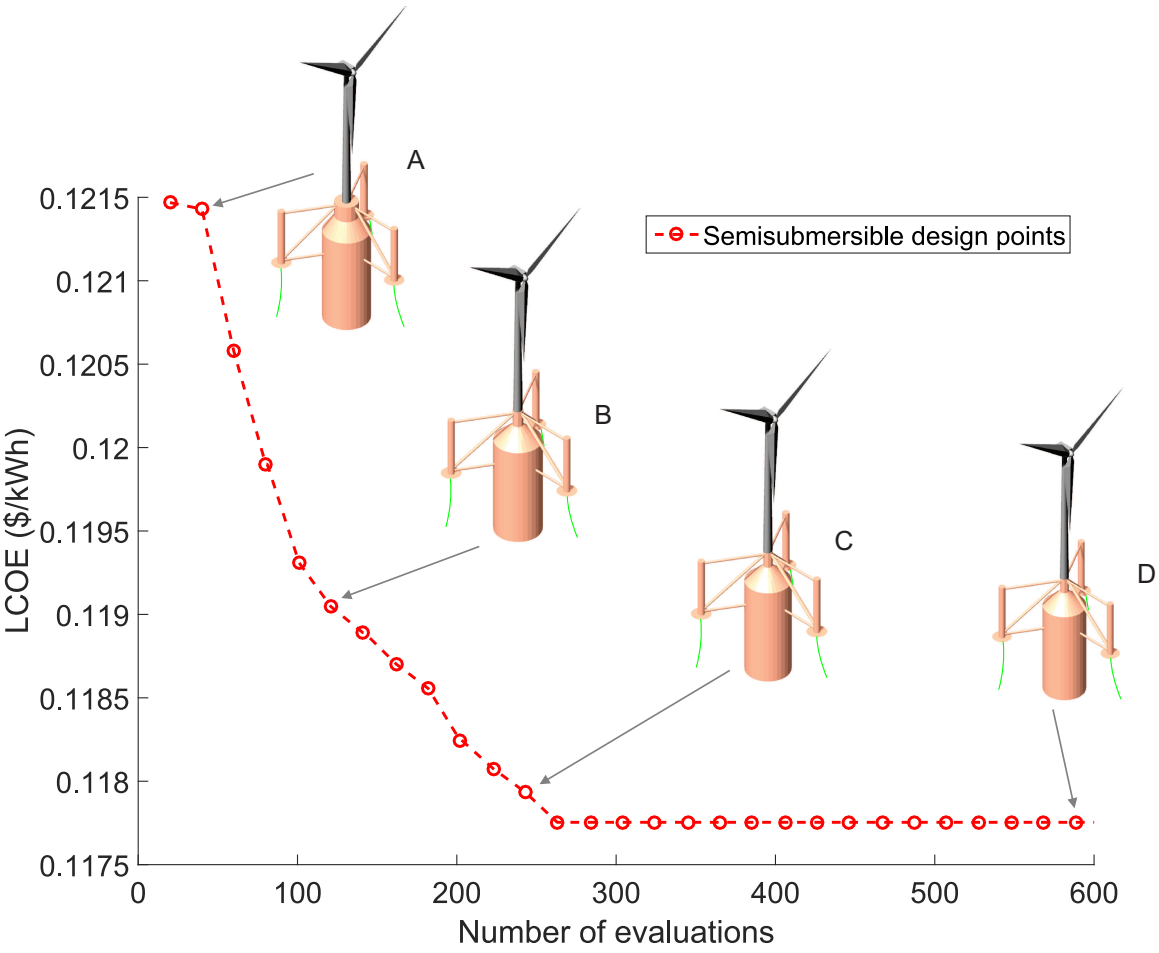

Figure 4.7: Design exploration of semisubmersible platforms subject to the LCOE and number of design evaluations. Four design candidates including the optimal platform (D) are presented in the design space.

the OC4-DeepCwind semisubmersible platform are provided in Table 4.11. The cost model calculates the support structure cost of $4.49 M for the OC4-DeepCwind with the LCOE of 11.95E-2 $/kWh, which is 1.52% higher than the calculated LCOE for the optimal design (platform D).

From the details of presented semisubmersible designs in Table 4.11, it is apparent that there is a consistent trend along the design components of platforms A to D as the LCOE decreases. This trend shows the inner cylinders radius and draft, taper ratio, and the radius of outer cylinders becoming smaller, while the heave plates, and draft of outer cylinders are not changed significantly. Moreover, the outer cylinders

Table 4.11: Platform characteristics, cost components, and calculated objective function (LCOE) for semisubmersible platform designs and the OC4-DeepCwind baseline model.

Design and cost components	**Units**	**Semisubmersible platforms**				
		A	**B**	**C**	**D**	**OC4-DeepCwind**
Inner cylinder draft (H_I)	m	60.81	60.80	60.68	60.64	20
Inner cylinder radius (R_I)	m	10.56	10.43	9.96	9.82	3
Taper ratio (T_I)	N/A	0.51	0.22	0.2	0.2	1
Radius of array (R_F)	m	28.95	28.89	28.94	28.92	30
Outer cylinders draft (H_O)	m	27.28	27.29	27.29	27.3	20
Outer cylinder radius (R_O)	m	1.61	1.51	1.51	1.51	6
Cross-bracing diameter (D_B)	m	1.22	1.28	1.28	1.28	2.34
Heave plate radius (R_{HP})	m	4.37	4.36	4.36	4.36	12
Mooring line type (X_M)	N/A	1.18	1.18	1.12	1.12	2.5
Support structure cost	1000 $	4849.3	4438.01	4192.8	4130.4	4496.8
Balance of station cost (BOS)	1000 $	11574.2	11151.5	10898.3	10834.7	11211.2
Levelized cost of energy (LCOE)	$/kWh	12.13E-2	11.92E-2	11.88E-2	11.77E-2	11.95E-2

radius and mooring line design parameter decreases slightly from platform A to D. Hence, the platform water plane area decreases (i.e. reducing sensitivity to incident waves). Note that reducing the platform sensitivity to the incident waves decreases the fairlead/anchor tensions and their costs.

Table 4.12: The accumulative fatigue damage rates and bending stresses of the wind turbine blade root and tower base as well as the platform ultimate fairlead and anchor loads for the optimal semisubmersible (platform D) and the OC4-DeepCwind.

Design parameters	**Platform D**	**MIT/NREL TLP**
Blade root bending stress (MPa)	9.7	9.6
Tower base bending stress (MPa)	26	26.1
Blade root fatigue damage rate (-)	0.63	0.63
Tower base fatigue damage rate (-)	0.66	0.28
Fair1Ten (kN)	2,433	2,160
Anch1Ten (kN)	2,115	1,590
Fair2Ten (kN)	1,884	3,735
Anch2Ten (kN)	1,614	2,340
Fair3Ten (kN)	612	2,190
Anch3Ten (kN)	108	1,965

The blade root and tower base bending stresses and fatigue damage rates as well as the platform ultimate fairlead and anchor loads for the optimal semisubmersible (platform D) and the OC4-DeepCwind are listed in Table 4.12. As this table shows,

the accumulative damage rate of the tower base for the platform D is higher than the baseline platform.

4.4 Conclusions and Future Work

In the past years, the design optimization of FOWTs was based on a sequential approach. In this approach, the structural, hydrodynamic, and aerodynamic designs of the FOWT were performed separately. This was mainly because of the level of complexity in modeling and simulating the coupled aero-hydro-servo interaction among different components of FOWTs. The work presented herein was a step forward in the design optimization of FOWT support structures that simultaneously designs the three classes of floating platforms and mooring systems subject to constraints on the wind turbine blade and tower stresses, platform cost and displacements, and mooring line breaking strengths with the LCOE as the objective function.

In this research, to carry out an integrated MDO for FOWTs, a fully coupled frequency domain dynamic model and a design parameterization scheme were incorporated to evaluate the internal forces, and system motions from the frequency domain outputs under turbulent winds and irregular waves. To calculate the objective function, a set of cost scaling tools for a 5 MW NREL offshore wind turbine and the dynamic model were used in the MDO framework. A K-BA optimization algorithm was selected to represent the design exploration and the optimal designs. To show the potential of this MDO framework, three baseline platforms including the MIT/NREL TLP, the OC3-Hywind, and the OC4-DeepCwind were compared with the results obtained from the design optimization.

The results for the TLPs showed the minimum LCOE of 11.26E-2 with the support structure cost of $3.44 M. The cost model indicated the LCOE of 11.88E-2 $/kWh for the MIT/NREL TLP that was 5.21% higher than the calculated LCOE for the optimal TLP. The lowest LCOE for the spar buoy case study was 11.59E-2 $/kWh

with the support structure cost of $3.76 M. The cost model shows the LCOE of 11.95E-2 $/kWh and the support structure cost of $4.49 M for the OC3-Hywind platform which was 3.1% higher than the LCOE of the optimal spar buoy. The LCOE of the optimal semisubmersible design was 11.77E-2 $/kWh with the support structure cost of $4.13 M, while the calculated LCOE for the OC4-DeepCwind was 11.95E-2 $/kWh which was 1.52% higher than the optimal design.

There are a number of avenues for improving the MDO framework used in this work, including improvements to the linearized dynamic model, cost model improvements, structural flexibility extensions, and extending the parameterization scheme to include turbine design variables. The future efforts are therefore directed at extending this MDO framework to include a higher fidelity dynamic model using a wide range of floating platforms and wind turbines by defining more flexible design variables.

Chapter 5

Conclusions and Future Work

Design optimization of FOWTs is a challenge to the widespread deployment of offshore wind technologies. The traditional approach to dealing with this challenge is the comparison analyses of a limited number of designs using the available time domain models, which often is computationally too expensive and can lead to a specific design at the targeted environmental condition. A multidisciplinary design optimization approach using a frequency domain dynamic model is the optimal solution to study a wide range of FOWTs. Hence, this dissertation suggests (1) a platform and mooring system parameterization scheme that spans three stability classes of FOWT support structures, (2) a fully coupled frequency domain dynamic model to predict the floating system motions and internal forces in the aggregate of turbulent wind and irregular wave conditions, and (3) a systematic MDO framework for three classes of FOWT support structures by interaction of different components of design problem to find the minimum LCOE. A summary of the key conclusions and future work directions are listed in the following sections.

5.1 Conclusions

The key conclusions of this dissertation are as follows:

1. **The unique Pareto front exploration of FOWTs for three classes of support structures using the frequency domain and cost models**

   In this study, to carry out a global optimization, a multi-objective GA was selected to represent the entire design exploration and optimal points through Pareto fronts. A combination of a cost model and dynamic model were used to define the economic and engineering performance of the platforms. A linearized hydrodynamic model computed loads on the platform, together with a quasi-static mooring system model, and a linear representation of the NREL 5 MW wind turbine under specific environmental conditions. The goal of this optimization was explore the cost implications of platform stability, expressed through the nacelle acceleration objective function, across the three FOWT platform stability classes.

   The results for optimized TLPs, spar buoys, and semisubmersible platforms lead to Pareto fronts with widely distributed optimal design points. The results showed that TLPs and semisubmersibles with three outer cylinders are the best options below a cost of $4.5 M. Above this cost, TLPs are the optimal platforms but achieve only modest performance improvements with exponentially increasing costs. Sensitivity analysis of the optimization revealed high sensitivity of the TLP designs to changes in the cost model. It is very important to note though that this work was a preliminary exploration across the full design space, focusing only on acceleration minimization versus cost, rather than a direct minimization of cost of energy. Therefore, a full multidisciplinary design optimization of FOWTs subject to LCOE was performed in Chapter 4.

2. **The unique fully coupled frequency domain dynamic model for FOWTs**

   In this study, a model framework was created to define the frequency domain responses of the system under turbulent winds and irregular waves using wind and wave PSDs. To verify this approach, an NREL 5 MW offshore wind turbine

with three classes of the baseline platforms including the OC3-Hywind, the MIT/NREL TLP, and the OC4-DeepCwind semisubmersible were examined using the output variables of 22 DOF and 6 DOF time domain models, as well as 6 DOF frequency domain model. The goal of this verification study was to compare the statistical results of the platform displacements, turbine and tower loads, and mooring system loads, as well as lifetime fatigue loads for the 6 DOF and 22 DOF time domain and the 6 DOF frequency domain models.

The comparison of the 6 DOF and 22 DOF time domain models showed consistent results for the key parameters of the wind turbine and baseline platforms. For the 6 DOF frequency domain and time domain models comparison, in terms of platform displacements, the difference between the results of the frequency domain and time domain models for the TLP is zero, the spar buoy platform showed small variations of 6.2% to 11.7%, and the semisubmersible showed relatively large variations of 5.3% to 13.2%. The comparison of the rotor thrust, total blade root bending moment, and total tower base bending moment showed a good agreement between the models for the TLP and the semisubmersible, and relatively large variations of 10.9% to 13.5% for the spar buoy platform. The best agreement between the fairlead and anchor tensions for both the frequency domain and time domain models achieved for the semisubmersible and spar buoy platform and large variations of 16.2% to 18.6% obtained for the TLP. In terms of fatigue loads for the turbine blade root and tower base, the comparison of the results for the semisubmersible indicated small variations of 8.6% and 4.4%, while the spar buoy platform and the TLP showed a relatively larger variations from 4.8% to 10%. The comparison of the fairlead and anchor fatigue loads displayed the overprediction of these loads in the frequency domain model of the semisubmersible and the underprediction of the fatigue loads for the spar buoy and TLP. The deviation of the results between the 22 DOF time domain model and 6 DOF frequency domain model were lower than

the cumulative variation of the modeling results between the 6 DOF time domain and 6 DOF frequency domain models due to apparently fortuitous pair of error trends from the frequency resolution assumption at the low frequencies. The verified coupled frequency domain model was used in the multidisciplinary design optimization study which presented in Chapter 4.

3. **The unique multidisciplinary design optimization of FOWTs support structures for the minimum LCOE**

   In this study, a fully coupled frequency domain dynamic model (see Chapter 3) and a design parameterization scheme (see Chapter 2) were incorporated to evaluate the internal forces, and system motions from the frequency domain outputs under turbulent winds and irregular waves. To calculate the objective function (LCOE), a set of cost scaling tools for a 5 MW NREL offshore wind turbine and the dynamic model were integrated to shape the multidisciplinary design optimization framework. A Kriging-Bat optimization algorithm was selected to represent the design exploration and the optimal designs. To show the potential of this framework, three baseline platforms including the MIT/NREL TLP, the OC3-Hywind, and the OC4-DeepCwind were compared with the results obtained from the design optimization.

   The results for the TLPs showed the minimum LCOE of 11.26E-2 $/kWh with the support structure cost of $3.44 M. The cost model indicated the LCOE of 11.88E-2 $/kWh for the MIT/NREL TLP that was 5.21% higher than the calculated LCOE for the optimal TLP. The lowest LCOE for the spar buoy case study was 11.59E-2 $/kWh with the support structure cost of $3.76 M. The cost model shows the LCOE of 11.95E-2 $/kWh and the support structure cost of $4.49 M for the OC3-Hywind platform which was 3.1% higher than the LCOE of the optimal spar buoy. The LCOE of the optimal semisubmersible design was 11.77E-2 $/kWh with the support structure cost of $4.13 M, while

the calculated LCOE for the OC4-DeepCwind was 11.95E-2 $/kWh which was 1.52% higher than the optimal design.

5.2 Future work

Although the current frequency domain dynamic model and MDO framework look promising, the following studies and modifications could be done to improve the current work.

- To improve the fully coupled frequency domain dynamic model of the floating structure, structural flexibilty extensions, second order wave loads, and mooring dynamics could be added to the linearization process and hydrodynamic analysis, respectively.
- An active rotor pitch angle and variable rotational speed controllers can be used outside the optimizer (to be able to opt as well in frequency domain) to improve the performance of the offshore wind turbine and consequently to reduce the structural loads and to increase the floating platform restoring moment.
- It would also be possible to expand the design space, by defining more design variables to create other support structures and wind turbines. For the wind turbine, it would be possible to add rotor, tower, and controller design variables as a complete set of parametric scheme in the design optimization.
- More accurate and updated cost models can be applied to calculate the LCOE not only for a single FOWT but also for an offshore wind farm.
- The accuracy of developed dynamic model in this dissertation is verified for several test cases, consequently it can be an appropriate model for floating moored structures such as wave energy convertors.

Bibliography

[1] Leung DY, Yang Y (2012) Wind energy development and its environmental impact: A review. Renewable and Sustainable Energy Reviews 16(1):1031–1039 1, 13, 56

[2] Schwartz M, Heimiller D, Haymes S, Musial W (2010) Assessment of offshore wind energy resources for the united states. Tech. rep., National Renewable Energy Laboratory (NREL), Golden, CO. 2, 13, 100

[3] Breton SP, Moe G (2009) Status, plans and technologies for offshore wind turbines in europe and north america. Renewable Energy 34(3):646–654 2, 13, 53

[4] Robertson A, Jonkman J (2011) Loads analysis of several offshore floating wind turbine concepts. Tech. rep., National Renewable Energy Laboratory (NREL), Golden, CO. ix, 2, 14, 30, 57, 76, 101, 102, 104

[5] Jonkman J (2010) Definition of the floating system for phase iv of oc3. Tech. rep., National Renewable Energy Laboratory (NREL), Golden, CO. 2, 60, 61, 104, 106

[6] Robertson A, Jonkman J, Masciola M, Song H, Goupee A, Coulling A, Luan C (2014) Definition of the semisubmersible floating system for phase ii of oc4. Tech. rep., National Renewable Energy Laboratory (NREL), Golden, CO. 2, 61, 104, 116

[7] Jonkman JM, Buhl Jr ML (2005) Fast user's guide-updated august 2005. Tech. rep., National Renewable Energy Laboratory (NREL), Golden, CO. 2, 56, 57, 66, 101, 110

[8] Larsen TJ, Hansen AM (2007) How 2 hawc2, the user's manual. Tech. rep., Risø National Laboratory 2, 57, 58, 101

[9] Bossanyi E (2003) Gh bladed theory manual. GH & Partners Ltd 2, 56, 58, 101

[10] Faltinsen O (1993) Sea loads on ships and offshore structures, vol 1. Cambridge university press 3, 59, 102

[11] Halfpenny A (1998) Dynamic analysis of both on and offshore wind turbines in the frequency domain. PhD thesis, University of London 59, 102

[12] Wayman EN (2006) Coupled dynamics and economic analysis of floating wind turbine systems. Master's thesis, Massachusetts Institute of Technology 15, 33, 34, 59, 102

[13] Wayman E, Sclavounos P, Butterfield S, Jonkman J, Musial W (2006) Coupled dynamic modeling of floating wind turbine systems: Preprint. Tech. rep., National Renewable Energy Laboratory (NREL), Golden, CO. 15, 59

[14] Tracy CCH (2007) Parametric design of floating wind turbines. Master's thesis, Massachusetts Institute of Technology 15, 21, 30, 32, 37, 59, 102, 116

[15] Hall MTJ (2013) Mooring line modelling and design optimization of floating offshore wind turbines. Master's thesis, University Of Victoria 21, 24, 59, 103, 117

[16] Karimi M, Hall M, Buckham B, Crawford C (2017) A multi-objective design optimization approach for floating offshore wind turbine support structures. Journal of Ocean Engineering and Marine Energy 3(1):69–87 3, 57, 59, 101, 102, 103, 107, 113

[17] Fingersh L, Hand M, Laxson A (2006) Wind turbine design cost and scaling model. Tech. rep., National Renewable Energy Lab.(NREL), Golden, CO (United States) 3, 103, 106, 112, 113, 114

[18] Myhr A, Bjerkseter C, Ågotnes A, Nygaard TA (2014) Levelised cost of energy for offshore floating wind turbines in a life cycle perspective. Renewable Energy 66:714–728 3, 103, 112

[19] Ozkan D (2011) Financial analysis and cost optimization of offshore wind energy under uncertainty and in deregulated power markets. PhD thesis, The George Washington University 3, 103

[20] Hofmann M (2011) A review of decision support models for offshore wind farms with an emphasis on operation and maintenance strategies. Wind Engineering 35(1):1–15 3, 103

[21] Hall M, Buckham B, Crawford C (2013) Evolving offshore wind: A genetic algorithm-based support structure optimization framework for floating wind turbines. In: OCEANS-Bergen, 2013 MTS/IEEE, IEEE, Bergen, Norway, pp 1–10 8, 16, 32, 36

[22] Saad A, Dong Z, Buckham B, Crawford C, Younis A, Karimi M (2018) A new kriging–bat algorithm for solving computationally expensive black-box global optimization problems. Engineering Optimization pp 1–21 10, 104, 117, 118

[23] Lefebvre S, Collu M (2012) Preliminary design of a floating support structure for a 5mw offshore wind turbine. Ocean Engineering 40:15–26 14, 102

[24] Bachynski EE, Moan T (2012) Design considerations for tension leg platform wind turbines. Marine Structures 29(1):89–114 14

[25] Bachynski EE, Etemaddar M, Kvittem MI, Luan C, Moan T (2013) Dynamic analysis of floating wind turbines during pitch actuator fault, grid loss, and shutdown. Energy Procedia 35:210–222 15

[26] Benassai G, Campanile A, Piscopo V, Scamardella A (2014) Mooring control of semi-submersible structures for wind turbines. Procedia Engineering 70:132–141 15

[27] Karimirad M, Michailides C (2015) V-shaped semisubmersible offshore wind turbine: An alternative concept for offshore wind technology. Renewable Energy 83:126–143 15, 102

[28] Clauss G, Birk L (1996) Hydrodynamic shape optimization of large offshore structures. Applied Ocean Research 18(4):157–171 15

[29] Parker NW (2007) Extended tension leg platform design for offshore wind turbine systems. Master's thesis, Massachusetts Institute of Technology 15, 103

[30] Fylling I, Berthelsen PA (2011) Windopt: an optimization tool for floating support structures for deep water wind turbines. In: ASME 2011 30th International Conference on Ocean, Offshore and Arctic Engineering, American Society of Mechanical Engineers, Rotterdam, The Netherlands, pp 767–776 15, 103

[31] Brommundt M, Krause L, Merz K, Muskulus M (2012) Mooring system optimization for floating wind turbines using frequency domain analysis. Energy Procedia 24:289–296 16, 59

[32] Myhr A, Nygaard TA, et al (2012) Load reductions and optimizations on tension-leg-buoy offshore wind turbine platforms. In: The Twenty-second International Offshore and Polar Engineering Conference 16, 103

[33] Hall M, Buckham B, Crawford C (2014) Hydrodynamics-based floating wind turbine support platform optimization: A basis function approach. Renewable Energy 66:559–569 16, 33, 103

[34] Muskulus M, Schafhirt S (2014) Design optimization of wind turbine support structures-a review. Journal of Ocean and Wind Energy 1(1):12–22 16, 103

[35] Karimirad M (2014) Aerodynamic and hydrodynamic loads. In: Offshore Energy Structures, Springer, Switzerland, pp 187–221 18

[36] Borgman LE (1967) Spectral analysis of ocean wave forces on piling (coastal engineering conference in santa barbara, california, october 1965). Journal of the waterways and harbors division 93(2):129–156 18

[37] Clauss G, Lehmann E, Östergaard C (2014) Offshore Structures: Volume I: Conceptual Design and Hydromechanics. Springer, London 19, 20

[38] Tao L, Dray D (2008) Hydrodynamic performance of solid and porous heave plates. Ocean engineering 35(10):1006–1014 20

[39] Savenije F, Peeringa J (2009) Aero-elastic simulation of offshore wind turbines in the frequency domain. Tech. rep., Energy Research Center of the Netherlands, Tech. Rep 20

[40] Jonkman J, Butterfield S, Musial W, Scott G (2009) Definition of a 5-mw reference wind turbine for offshore system development. Tech. rep., National Renewable Energy Laboratory (NREL), Golden, CO. ix, 21, 25, 75, 76, 104

[41] Jonkman JM (2007) Dynamics modeling and loads analysis of an offshore floating wind turbine. PhD thesis, University Of Colorado At Boulder 21, 57

[42] Robertson A, Jonkman J, Masciola M, Song H, Goupee A, Coulling A, Luan C (2012) Definition of the semisubmersible floating system for phase ii of oc4.

Tech. rep., National Renewable Energy Laboratory (NREL), Golden, CO. 26, 28

[43] Matha D (2010) Model development and loads analysis of an offshore wind turbine on a tension leg platform with a comparison to other floating turbine concepts. Tech. rep., National Renewable Energy Laboratory (NREL), Golden, CO. 28, 57, 61, 101

[44] Butterfield CP, Musial W, Jonkman J, Sclavounos P, Wayman L (2007) Engineering challenges for floating offshore wind turbines. National Renewable Energy Laboratory Golden, CO. 28

[45] Jonkman J, Musial W (2010) Offshore code comparison collaboration (oc3) for iea task 23 offshore wind technology and deployment. Tech. rep., National Renewable Energy Laboratory (NREL), Golden, CO. 29

[46] Pareto V (1906) Manuale di economica politica, societa editrice libraria. milan. translated to English by Schwier AS as Manual of Political Economy, Kelley, New York 32

[47] Arora J (2004) Introduction to optimum design. Academic Press, Iowa 32

[48] MATLAB (2014) version 8.3.0.532 (R2014b). The MathWorks Inc., Natick, Massachusetts 33, 106

[49] Sclavounos P, Tracy C, Lee S (2008) Floating offshore wind turbines: Responses in a seastate pareto optimal designs and economic assessment. In: ASME 2008 27th International Conference on Offshore Mechanics and Arctic Engineering, American Society of Mechanical Engineers, Estoril, Greece, pp 31–41 33, 34

[50] Bulder B, Van Hees MT, Henderson A, Huijsmans R, Pierik J, Snijders E, Wijnants G, Wolf M (2002) Study to feasibility of and boundary conditions

for floating offshore wind turbines. Tech. rep., ECN, MARIN, Lagerway the Windmaster, TNO, TUD 34

[51] Hall M, Buckham B, Crawford C (2014) Evaluating the importance of mooring line model fidelity in floating offshore wind turbine simulations. Wind energy 17(12):1835–1853 37, 57, 101, 107

[52] Jonkman J, Matha D (2011) Dynamics of offshore floating wind turbinesanalysis of three concepts. Wind Energy 14(4):557–569 40, 60, 78

[53] Jonkman JM (2010) Definition of the Floating System for Phase IV of OC3. National Renewable Energy Laboratory Golden, CO. 53

[54] Henderson AR, Witcher D (2010) Floating offshore wind energy-a review of the current status and an assessment of the prospects. Wind Engineering 34(1):1–16 56, 100

[55] Lupton R (2015) Frequency-domain modelling of floating wind turbines. PhD thesis, University of Cambridge 60, 90, 102

[56] Collu M, Borg M, Manuel L (2016) On the relative importance of loads acting on a floating vertical-axis wind turbine system when evaluating the global system response. In: ASME 2016 35th International Conference on Ocean, Offshore and Arctic Engineering, American Society of Mechanical Engineers, pp V006T09A045–V006T09A045 56, 100

[57] Lackner MA, Rotea MA (2011) Passive structural control of offshore wind turbines. Wind energy 14(3):373–388 56, 57, 101

[58] Stewart GM, Lackner MA (2014) The impact of passive tuned mass dampers and wind–wave misalignment on offshore wind turbine loads. Engineering Structures 73:54–61 56

[59] Skaare B, Hanson TD, Nielsen FG, Yttervik R, Hansen AM, Thomsen K, Larsen TJ (2007) Integrated dynamic analysis of floating offshore wind turbines. In: 2007 European Wind Energy Conference and Exhibition 57, 101

[60] Matha D, Fischer T, Kuhn M, Jonkman J (2010) Model development and loads analysis of a wind turbine on a floating offshore tension leg platform. Tech. rep., National Renewable Energy Laboratory (NREL), Golden, CO. ix, xii, 57, 59, 79, 101, 102, 121

[61] Sultania A, Manuel L (2010) Extreme loads on a spar buoy supported floating offshore wind turbine. In: Proceedings of the structures, structural dynamics materials conference, Orlando, FL, Paper No. AIAA, vol 2738 57, 101

[62] Roddier D, Cermelli C, Aubault A, Weinstein A (2010) Windfloat: A floating foundation for offshore wind turbines. Journal of renewable and sustainable energy 2(3):033,104 57

[63] Ormberg H, Passano E, Luxcey N (2011) Global analysis of a floating wind turbine using an aero-hydro-elastic model. part 1: Code development and case study. In: 30th International Conference on Ocean, Offshore, and Arctic Engineering, Rotterdam, The Netherlands, Paper No. OMAE2011-50114 57

[64] Henderson AR, Argyriadis K, Nichos J, Langston D (2010) Offshore wind turbines on tlps-assessment of floating support structures for offshore wind farms in german waters. In: 10th German wind energy conference, Bremen, Germany 58

[65] Myhr A, Maus KJ, Nygaard TA, et al (2011) Experimental and computational comparisons of the oc3-hywind and tension-leg-buoy (tlb) floating wind turbine conceptual designs. In: The Twenty-first International Offshore and Polar Engineering Conference, International Society of Offshore and Polar Engineers 58

[66] Manual AU (1994) Swanson analysis systems. Inc, Volumes I, II, III, IV, Revision 5(0) 58

[67] Larsen TJ, Kallesøe BS, Hansen HF, et al (2011) Dynamics of a floating wave energy platform with threewind turbines operating. In: The Twenty-first International Offshore and Polar Engineering Conference, International Society of Offshore and Polar Engineers 58

[68] Risø D, Kallesøe BS, Larsen TJ, Uwe S (2011) Aero-hydro-elastic simulation platform for wave energy. Wind energy 2:3 58

[69] Karimirad M, Moan T (2011) Wave-and wind-induced dynamic response of a spar-type offshore wind turbine. Journal of waterway, port, coastal, and ocean engineering 138(1):9–20 58

[70] Cordle A, Jonkman J, et al (2011) State of the art in floating wind turbine design tools. In: The Twenty-first International Offshore and Polar Engineering Conference, International Society of Offshore and Polar Engineers 58

[71] Øye S (1999) Flex5 user manual. Danske Techniske Hogskole, Technical Report Ver 5 58

[72] Ramachandran GKVK (2013) A numerical model for a floating tlp wind turbine. PhD thesis, Technical University of Denmark 58

[73] Bae Y, Kim M (2014) Aero-elastic-control-floater-mooring coupled dynamic analysis of floating offshore wind turbine in maximum operation and survival conditions. Journal of Offshore Mechanics and Arctic Engineering 136(2):020,902 58

[74] Fulton G, Malcolm D, Elwany H, Stewart W, Moroz E, Dempster H (2007) Semi-submersible platform and anchor foundation systems for wind turbine support. NREL/SR (500–40282) 58

[75] Casale C, Lembo E, Serri L, Viani S (2010) Preliminary design of a floating wind turbine support structure and relevant system cost assessment. Wind Engineering 34(1):29–50 59

[76] Bergholm F (1989) Moses handbook. 35, Coronet Books 59

[77] Sandner F, Schlipf D, Matha D, Seifried R, Cheng PW (2012) Reduced nonlinear model of a spar-mounted floating wind turbine. Proc DEWEK 59

[78] Zhang R, Tang Y, Hu J, Ruan S, Chen C (2013) Dynamic response in frequency and time domains of a floating foundation for offshore wind turbines. Ocean Engineering 60:115–123 59

[79] Veritas DN (1998) Sesam user manual. Hovik, Norway 59

[80] Low Y, Langley R (2006) Time and frequency domain coupled analysis of deepwater floating production systems. Applied Ocean Research 28(6):371–385 59, 102

[81] Brebbia CA, Walker S (2013) Dynamic analysis of offshore structures. Newnes 59, 102

[82] Philippe M, Babarit A, Ferrant P (2011) Comparison of time and frequency domain simulations of an offshore floating wind turbine. In: ASME 2011 30th International Conference on Ocean, Offshore and Arctic Engineering, American Society of Mechanical Engineers, pp 589–598 59

[83] Saad AEH, Dong Z, Karimi M (2017) A comparative study on recently-introduced nature-based global optimization methods in complex mechanical system design. Algorithms 10(4):120 59, 101, 102

[84] van Engelen T, Braam H (2004) Turbu offshore, computer program for frequency domain analysis of horizontal axis offshore wind turbines. Tech. rep., Implementation 59, 102

[85] Kvittem MI, Moan T (2015) Frequency versus time domain fatigue analysis of a semisubmersible wind turbine tower. Journal of Offshore Mechanics and Arctic Engineering 137(1):011,901 59

[86] Namik H, Stol K (2010) Individual blade pitch control of floating offshore wind turbines. Wind Energy: An International Journal for Progress and Applications in Wind Power Conversion Technology 13(1):74–85 62

[87] Lackner MA (2009) Controlling platform motions and reducing blade loads for floating wind turbines. Wind Engineering 33(6):541–553 62, 70

[88] Browning J, Jonkman J, Robertson A, Goupee A (2014) Calibration and validation of a spar-type floating offshore wind turbine model using the fast dynamic simulation tool. In: Journal of Physics: Conference Series, IOP Publishing, vol 555, p 012015 62

[89] Noureldin A, Karamat TB, Georgy J (2013) Basic navigational mathematics, reference frames and the earths geometry. In: Fundamentals of Inertial Navigation, Satellite-based Positioning and their Integration, Springer, pp 21–63 62

[90] Hasselmann K (1973) Measurements of wind wave growth and swell decay during the joint north sea wave project (jonswap). Dtsch Hydrogr Z 8:95 64, 110

[91] Jonkman J, Robertson A, Hayman G (2014) Hydrodyn users guide and theory manual. Tech. rep. 64, 106

[92] TC88-MT I (2005) Iec 61400-3: Wind turbines–part 1: Design requirements. International Electrotechnical Commission, Geneva 64

[93] Arany L, Bhattacharya S, Macdonald J, Hogan SJ (2015) Simplified critical mudline bending moment spectra of offshore wind turbine support structures. Wind Energy 18(12):2171–2197 64, 65, 78, 120

[94] Kaimal JC, Wyngaard J, Izumi Y, Coté O (1972) Spectral characteristics of surface-layer turbulence. Quarterly Journal of the Royal Meteorological Society 98(417):563–589 64, 110

[95] Jonkman BJ (2009) Turbsim user's guide: Version 1.50. Tech. rep. 64, 78, 106

[96] Bir GS (2010) User's guide to mbc3: Multi-blade coordinate transformation code for 3-bladed wind turbine. Tech. rep. 68, 72, 106

[97] Hayman G, Buhl Jr M (2012) Mlife users guide for version 1.00. National Renewable Energy Laboratory, Golden, CO 74, 75, 112

[98] Hayman G (2012) Mlife theory manual for version 1.00. National Renewable Energy Laboratory, Golden, CO 74, 75, 106

[99] Ellingwood BR, Tekie PB (1999) Wind load statistics for probability-based structural design. Journal of Structural Engineering 125(4):453–463 85

[100] Europe W (2017) The european offshore wind industrykey trends and statistics 2016. Wind Europe: Brussels, Belgium p 37 99

[101] Shirzadeh R, Devriendt C, Bidakhvidi MA, Guillaume P (2013) Experimental and computational damping estimation of an offshore wind turbine on a monopile foundation. Journal of Wind Engineering and Industrial Aerodynamics 120:96–106 101

[102] Karimirad M, Moan T (2012) A simplified method for coupled analysis of floating offshore wind turbines. Marine Structures 27(1):45–63 101

[103] Paulsen US, Madsen HA, Hattel JH, Baran I, Nielsen PH (2013) Design optimization of a 5 mw floating offshore vertical-axis wind turbine. Energy Procedia 35:22–32 101

[104] Damgaard M, Zania V, Andersen LV, Ibsen LB (2014) Effects of soil–structure interaction on real time dynamic response of offshore wind turbines on monopiles. Engineering Structures 75:388–401 101

[105] Ashuri T, Zaaijer MB, Martins JR, Van Bussel GJ, Van Kuik GA (2014) Multidisciplinary design optimization of offshore wind turbines for minimum levelized cost of energy. Renewable Energy 68:893–905 103, 115, 116, 117

[106] Dinwoodie I, McMillan D (2012) Sensitivity of offshore wind turbine operation & maintenance costs to operational parameters. In: Proceedings of the 42nd ESReDA Seminar on Risk and Reliability for Wind Energy and other Renewable Sources 103

[107] Fischer GR, Kipouros T, Savill AM (2014) Multi-objective optimisation of horizontal axis wind turbine structure and energy production using aerofoil and blade properties as design variables. Renewable Energy 62:506–515 103

[108] Rademakers L, Braam H, Obdam T, vd Pieterman R (2009) Operation and maintenance cost estimator (omce) to estimate the future o&m costs of offshore wind farms. In: European Offshore Wind 2009 Conference, vol 1, pp 14–16 103

[109] Roeth J, McClellan S, Ozkan D, Kempton W, Levitt A, Thomson H (2015) New york offshore wind cost reduction study. New York State Energy Research and Development Authority: Albany, NY, USA 103

[110] Dykes K, Meadows R, Felker F, Graf P, Hand M, Lunacek M, Michalakes J, Moriarty P, Musial W, Veers P (2011) Applications of systems engineering to the research, design, and development of wind energy systems. Tech. rep., National Renewable Energy Lab.(NREL), Golden, CO (United States) 103

[111] Lee CH (1995) WAMIT theory manual. Massachusetts Institute of Technology, Department of Ocean Engineering 106

[112] Moriarty PJ, Hansen AC (2005) Aerodyn theory manual. Tech. rep., National Renewable Energy Lab., Golden, CO (US) 106

[113] Musial W, Butterfield S, Boone A (2004) Feasibility of floating platform systems for wind turbines. In: 42nd AIAA aerospace sciences meeting and exhibit, p 1007 113

[114] Kim H, Choung J, Jeon GY (2014) Design of mooring lines of floating offshore wind turbine in jeju offshore area. In: ASME 2014 33rd International Conference on Ocean, Offshore and Arctic Engineering, American Society of Mechanical Engineers, pp V09AT09A042–V09AT09A042 113

[115] Caboni M (2016) Probabilistic design optimization of horizontal axis wind turbine rotors. PhD thesis, University of Glasgow 116

[116] Veritas DN (2013) Design of floating wind turbine structures. Offshore Standard DNV-OS-J103 5 116

[117] Veritas DN (2009) Offshore standard dnv-os-e302 offshore mooring chain. DNV-OSE302 117

[118] Veritas DN, DNV OE (2009) Offshore mooring steel wire ropes. DNV-OSE304 117

[119] Yang XS (2010) A new metaheuristic bat-inspired algorithm. In: Nature inspired cooperative strategies for optimization (NICSO 2010), Springer, pp 65–74 117

[120] Audet C, Denni J, Moore D, Booker A, Frank P (2000) A surrogate-model-based method for constrained optimization. In: 8th Symposium on Multidisciplinary Analysis and Optimization, p 4891 117

[121] Cavazzuti M (2012) Optimization methods: from theory to design scientific and technological aspects in mechanics. Springer Science & Business Media 118